Study of high temperature phase stability and thermo-physical properties of Fe-Cr based alloys

By

Raj Narayan Hajra

Enrolment No.: **CHEM02201404003**

Indira Gandhi Centre for Atomic Research
Kalpakkam 603102, India

A thesis submitted to the
Board of Studies in Chemical Sciences
In partial fulfillment of requirements
for the Degree of

DOCTOR OF PHILOSOPHY

of

HOMI BHABHA NATIONAL INSTITUTE

November 2018

Homi Bhabha National Institute

Recommendations of the Viva Voce Committee

As members of the Viva Voce Committee, we certify that we have read the dissertation prepared by Mr. Raj Narayan Hajra entitled "**Study of high temperature phase stability and thermo-physical properties of Fe-Cr based alloys**" and recommend that it may be accepted as fulfilling the thesis requirement for the award of Degree of Doctor of Philosophy.

Chairman – Prof. K. Ananthasivan
Date: 2nd Aug 2019

Guide / Convener – Prof. Saroja Saibaba
Date: Aug. 02, 2019

Examiner - Prof. N. N. Viswanathan
N.N. Viswanathan
Date: 2nd Aug 2019

V. Jayaraman
Member 1- Prof. V. Jayaraman
Date: 02/08/2019.

R. Govindaraj
Member 2- Prof. R. Govindaraj
Date: 2nd Aug 2019

Technology Advisor- Dr. S. Raju
Date: 02/08/2019

Final approval and acceptance of this thesis is contingent upon the candidate's submission of the final copies of the thesis to HBNI.

I/We hereby certify that I/we have read this thesis prepared under my/our direction and recommend that it may be accepted as fulfilling the thesis requirement.

Date: **02.08.2019**

Place: IGCAR, Kalpakkam

Signature of Guide

STATEMENT BY AUTHOR

This dissertation has been submitted in partial fulfillment of requirements for an advanced degree at Homi Bhabha National Institute (HBNI) and is deposited in the Library to be made available to borrowers under rules of the HBNI.

Brief quotations from this dissertation are allowable without special permission, provided that accurate acknowledgement of source is made. Requests for permission for extended quotation from or reproduction of this manuscript in whole or in part may be granted by the Competent Authority of HBNI when in his or her judgment the proposed use of the material is in the interests of scholarship. In all other instances, however, permission must be obtained from the author.

Raj Narayan Hajra.

(Raj Narayan Hajra)

DECLARATION

I, hereby declare that the investigation presented in the thesis has been carried out by me. The work is original and has not been submitted earlier as a whole or in part for a degree / diploma at this or any other Institution / University.

Raj Narayan Hajra.

(Raj Narayan Hajra)

Dedicated to

My little princes

Shree

LIST OF PUBLICATIONS ARISING FROM THESIS

Journal

1. Effect of sigma phase on thermo-physical properties of $Fe_{55}Cr_{45}$ alloy

   Raj Narayan Hajra, H. Tripathy, C. Sudha, N. Vijayashanthi, S. Raju, S. Saroja, ***Intermetallics*** (Accepted).

2. Study of high temperature phase stability and phase transformation kinetics of sigma and parent alpha phase in $Fe_{56}Cr_{44}$(wt.%) alloy

   Raj Narayan Hajra, A.K. Rai, H. Tripathy, N. Vijayashanthi, S. Raju, S. Saroja, ***J. Alloy Compd.***, 727 (2017) 826.

3. Influence of tungsten on transformation characteristics in P92 ferritic-martensitic steel

   Raj Narayan Hajra, A.K. Rai, H. Tripathy, S. Raju, S. Saroja, ***J. Alloy Compd.,*** 689 (2016) 829.

4. Phase stability of Fe-15wt.% Cr alloy: A calorimetry and modeling based approach to elucidating the role of magnetic interactions

   Raj Narayan Hajra, S. Raju, H. Tripathy, A.K. Rai, S. Saroja, ***Thermochim. Acta***, 620 (2015) 40

5. Thermodynamics of α'(Fe-rich bcc)+α''(Cr-rich bcc)$\rightarrow\alpha$(bcc) and $\alpha^{para} \rightarrow \alpha^{ferro}$ transformations in Fe-20wt.%Cr Alloy: Drop calorimetry study and elucidation of magnetic contribution to phase stability

   Raj Narayan Hajra, S. Raju, A.K. Rai, H. Tripathy, R. Mythili, S. Saroja, ***Metall. Mater.Trans. A***, 45 (2014) 3386.

Conference Proceedings

1. A calorimetric study of phase stability in Fe-15 wt. % Cr alloy

   Raj Narayan Hajra, S. Raju, A.K. Rai, H. Tripathy, S. Saroja, Proc. Thermans, IIT BHU, Varanasi, 18-22 January, 2016.

2. High temperature thermal stability and thermal expansion characteristics of sigma (σ) and alpha (α) phases of $Fe_{56}Cr_{44}$ alloy

   Raj Narayan Hajra, C. Sudha, H. Tripathy, S. Raju, S. Saroja, Proc. Thermans, Goa University, 16-20 January, 2018.

Raj Narayan

(Raj Narayan Hajra)

Acknowledgements

It is a genuine pleasure to convey my deep sense of thanks and gratitude to all of those, whose support and encouragement assisted me in preparing this Ph.D. thesis. My humble acknowledgement is as follows;

I would like to express my deep sense of gratitude to my guide, Dr. Saroja Saibaba, Associate Director, Material Characterization Group, IGCAR for her invaluable guidance, inspiration and support throughout this project.

I am extremely grateful to Dr. S. Raju, Head, Physical Metallurgy Division, whose persistent guidance and indispensible technical support assisted me in the completion of my Ph.D. work.

I am thankful to my doctoral committee, Chairman- Prof. K. Ananthasivan and Members- Prof. V. Jayaraman, Prof. R. Govindaraj, for their insightful suggestions for the progress of the research work at various DC meetings.

I am grateful to Dr. C. Sudha, Head, CMMS, IGCAR for her continuous support, encouragement and worth technical value addition to my thesis. I am thankful to her for her critical correction which make the thesis a worth reading.

My heartfelt acknowledgements go to my colleagues Dr. Arun Kumar Rai (currently at RRCAT, Indore), Dr. Hara Prasanna Tripathi and Mrs. N. Vijayashanthi for their timely help in the laboratory works and useful discussions.

I would like to thank Dr. Arup Dasgupta, Dr. R. Mythili, Dr. Chanchal Ghosh, Mr. Manmath Dash, Dr. Prasanthi, Mr. Haribabu, and all PMD members for providing the experimental facilities and their support during the course of this research work.

I owe my sincere gratitude to my parents and my mother in law for their persistent moral support and faith on me. I am extremely thankful to my beloved wife *Gargi* for taking care of most of my domestic responsibilities and encouraging me to carry out my research work.

At the end, I thank the Divine Master for giving me the strength, ability and opportunity to undertake this research study.

Contents

Chapter 1

Introduction

Chapter 2

Experimental Methodology

Chapter-3

Phase Stability of Fe-16 at.% Cr Alloy: A Calorimetry and Modelling Based Approach to Elucidate the Role of Magnetic Interactions

Chapter – 4

Influence of phase separation on thermal properties in Fe-21 at. %Cr binary system

Chapter – 5

Study of sigma (σ) → alpha (α) transformation characteristics in Fe-Cr model alloy by dynamic calorimetry

Chapter 6

High temperature thermo-physical and heat transport properties of sigma (σ) and alpha (α) phases

Chapter-7

Effect of W on the α ↔γ transformation characteristics in Fe-Cr based binary and multi component alloys

Chapter 8

Summary & Further Avenues of Research

SYNOPSIS

The availability of high performance structural materials is an important step towards the successful development of advanced reactor technologies which could be either nuclear or conventional power plants. The demanding service environment of fast breeder reactor (FBR), or fusion reactors requires a wide range of structural materials that has to be tailored for high performance in a hostile environment involving intense heat fluxes, high temperatures, potentially corrosive coolants, significant cyclic thermo mechanical stresses, high-energy neutrons and electromagnetic radiation. The technological challenges therefore associated with the accomplishment of advance reactor technologies, depends to a very large extent on the advancement of high strength structural materials for critical components. In this context, 9-12 Cr based ferritic/martensitic (F-M) steel and oxide dispersed high Cr ferritic steels have been identified worldwide as potential materials for vital core components. These steels have excellent thermo-mechanical properties in radiation and corrosive environments at moderate temperature (~500^{o}C (773 K)). The major advantage of these steels over austenitic steels and Ni base super alloy is void swelling resistance. Presence of minimum Ni in ferritic steel also leads to substantial cost reduction which makes them economically viable. However, notwithstanding the above advantages, mechanical properties namely high temperature creep strength, impact toughness and tensile ductility are the major challenges for these steels for long term performance under radiation environment. The 9-12% Cr steels are used in the normalized and tempered condition where in fine scale precipitates provide strength apart from the lath substructure. The recovery of tempered martensite microstructure leading to substructure modifications and coarsening of precipitates is the main reason for deterioration of mechanical strength at elevated temperatures. It is difficult to control the recovery of metastable martensite, since it is an intrinsic process. The rapid recovery of the martensite structure leads to drastic reduction in strength at temperatures exceeding 550 ^{o}C (823 K). There has been considerable research activity in recent times to develop high strength ferritic steels with addition of either refractory metals like Ta and W, strong carbide or nitride formers like V and Nb or nano sized oxide dispersoids. Increase in Cr content > 13 weight% provides enhanced corrosion resistance, while the steel remains in the single phase ferrite field thus suppressing the martensitic transformation. However, the high Cr ferritic steels are found to be vulnerable at elevated temperature because of two reasons; (b) 475 ^{o}C embrittlement and (b) formation of brittle intermetallic Frank–Kasper phases like laves and sigma phase. The 475 ^{o}C embrittlement is mainly observed in high Cr steels, nucleated by the complex interaction of magnetism and chemistry between ferromagnetic Fe and anti-ferromagnetic Cr atoms. The magnetism induced phase separation of Fe-Cr solid solution (*α-ferrite*) into Fe rich bcc (α') and Cr rich bcc (α'') results in deterioration in high temperature properties which is commonly known as 475 ^{o}C embrittlement. Moreover, the formation of brittle intermetallic sigma phase upon prolonged exposures to high temperature and stress is also detrimental to the high temperature mechanical properties. The formation of sigma phase is governed by the phase stability of Fe-Cr binary phase field at elevated temperature. In the presence of other alloying elements in steels, the kinetics of phase separation (α'' formation) and sigma formation may be either enhanced or retarded. Therefore, the knowledge base on thermodynamics, phase stability and phase transformation kinetics of Fe-Cr binary systems is essential in successful implementation and technological exploitation of advanced ferritic steels. A detailed survey of recent literature on Fe-Cr system also reveals that quite a few issues of fundamental importance, in particular the intricate interplay between magnetic and chemical degrees of freedom and their combined influence in dictating the low and intermediate temperature phase equilibrium are yet to be resolved. Specifically, the prevailing understanding with regard to the equilibrium state of Cr solubility in α matrix of Fe-rich side is still unsolved. A gradual crossover of formation enthalpy ($\Delta^{o}H_f$) of α phase of Fe-Cr binary system at ~ 4 at.% Cr, from being mildly negative to strongly positive in character by first principle calculations supported the extended Cr solubility in contradiction with the earlier assessment. Since the pioneering studies of Dench and Normanton et al., there have not been many in-depth calorimetry investigations on Fe-Cr alloys. This again is a serious limitation from the point of view of not having adequate data that would help in modelling the energetics of magnetic contribution to Gibbs energy, G. In addition, it is also well known that magnetism is responsible for the anomalous, nonsystematic behavior of thermo-physical, mechanical and magnetic properties witnessed in dilute Fe-Cr alloys. Curie temperature (T_C) of Fe-Cr alloy exhibits a local maxima at ~ 4 at % of Cr. Further irregular trend has been observed for lattice parameter also. Theoretically calculated lattice parameter shows a maxima in low Cr region in Fe rich side. The elastic modulus and Poisson ratios have also been observed to exhibit a minima at ~ 5-6 at% Cr. It is also observed that the upper limit of sigma phase field is not established beyond speculation as the sigma dissolution temperature is reported from 1093 to 1203 K in Fe-Cr alloys. The $\sigma \leftrightarrow \alpha$ transformation characteristics and the effect of sigma phase on the heat transport and thermo-physical properties of alpha phase has also not been studied in detail. It is also observed that there exist huge scatter in experimental data for γ phase field of Fe-Cr binary alloys which plays important role to form martensitic microstructure for low Cr (9 wt.% Cr) ferritic - martensitic steel. In view of the above, present thesis is an attempt to resolve some of the issues detailed above namely the investigations on the high temperature thermal stability and thermo-physical properties of Fe-Cr alloys. It also includes the synthesis of σ phase from its parent α phase in Fe-Cr model alloys, study of $\sigma \rightarrow \alpha$ transformation characteristics and the effect of σ phase on the thermal and heat transport properties of α phase. This thesis report contains eight (8) chapters in all. The organization of the thesis is given below.

Chapter 1: ***Introduction***

This chapter deals with the introduction based on extensive literature survey which includes the relevance of Fe-Cr phase field in governing the characteristics of advanced ferritic steels, origin of miscibility gap, the present status of literature for α, γ, and σ phase fields in Fe-Cr binary system, anomalous behavior of α phase field for Fe rich Fe-Cr alloys and the effect of α" and σ phase field on the thermo-physical and heat transport properties of α ferrite phase in Fe-Cr alloys.

Chapter 2: ***Experimental Methodology***

In this chapter the experimental methodology employed in this thesis is presented in detail. Brief descriptions on alloy preparation, compositional characterization and annealing treatments are followed by structural characterization techniques namely X-ray diffraction, metallography, scanning and transmission electron microscopy. Descriptions on specific instrumentation techniques like inverse drop calorimetry (IDC), differential scanning calorimetry (DSC), high temperature dilatometry, laser flash thermal diffusivity (LFTD) are described in adequate detail. The experimental schedules, calibration, and error limits associated with each experimental technique are also described in this chapter.

Chapter 3: **Study of phase stability and thermodynamic properties of Fe rich Fe-Cr (1-16 *at. %*) binary alloys**

This chapter demonstrates the quantification of magnetic, anharmonic and electronic effects on the phase stability of Fe rich Fe-Cr alloy which partially fills the gap on thermal property data in this particular region. In specific terms, measurements of high temperature enthalpy increment (H_T-$H_{298.15}$) and heat capacity have been made on Fe-16 *at.%* Cr alloy using drop calorimetry in the temperature range, 200 – 1200 ^oC (473 to 1473 K), which are compared with the data available in literature. Further, a consolidated physically based modelling approach has been developed which fully describes the thermodynamic properties of ferromagnetic α phase for Fe-rich Fe-Cr alloys (0-16 *at.* %Cr). Therefore, by generation of high temperature calorimetry data and possible integration of these in terms of simple and physically based modelling protocols, a wholesome conceptual basis of phase stability in Fe rich Fe-Cr system has been established.

Chapter 4: Influence of phase separation on thermal properties of Fe-Cr (21 at.%) binary alloy

This chapter demonstrates the effect of phase separation (α' + α'') on the thermal properties of Fe-21 *at.%* Cr alloy. After arc melting, homogenization and slow cooling, Fe-21 *at.%* Cr exhibits two phase structure of α' + α''. Enthalpy measurements were carried out by using inverse drop calorimeter in the temperature range, 298 to 1473 K (25 to 1200 °C). The experiments revealed two distinct phase transformations: (i) at 720±10 K (447±10 °C), the Fe-21Cr alloy transformed from α'(Fe-rich)+α''(Cr-rich) two phase microstructure to α single phase; (ii) at 925±10 K (652±10 °C), the ferromagnetic single phase α transformed to paramagnetic state. Both these transformations were clearly attested by the measured enthalpy increment variation with temperature. The enthalpy data obtained in this study have been combined with available literature information to forge an integrated theoretical assessment of the energetic aspects of $\alpha'+\alpha''\rightarrow\alpha$, and $\alpha_{ferro}\rightarrow\alpha_{para}$ transformations. In addition, a comprehensive evaluation of enthalpy and heat capacity data for Fe-21Cr alloy in the temperature range 0-1473 K (-273 to 1200 °C), with explicit incorporation of magnetic contribution has also been made.

Chapter 5: Study of sigma (σ) → alpha (α) transformation characteristics by dynamic calorimetry for Fe-Cr model alloy

This chapter presents an extensive experimental characterization of high temperature phase stability and phase transformation kinetics of intermetallic sigma (σ) and alpha (α) phases of $Fe_{54}Cr_{46}$ alloy carried out by dynamic calorimetry. Sigma phase (σ) was synthesized from its parent alpha (α) phase of $Fe_{54}Cr_{46}$ alloy by annealing at 700 °C (973K) for 360 h in vacuum. A comparative thermal study of sigma (σ) and alpha phase alloy was performed from 100 – 1400 °C (373 to 1673 K) by Differential Scanning Calorimeter (DSC). Single inflection of ferro to para magnetic transition (T_C) was observed in DSC upto melting at 558 °C (831 K) for alpha phase. The sigma (σ) to alpha (α) decomposition temperature for sigma phase was measured under pseudo equilibrium condition as 849 °C (1122 K). It was observed that sigma (σ) phase decomposition temperature is nearly 30 °C higher than the presently reported upper limit of 820 °C (1093 K) in Fe Cr phase diagram. Study of sigma (σ) to alpha (α) phase transformation kinetics has been carried out by employing various heating rates from 1 to 50 K min^{-1} in DSC. The activation energy for sigma (σ) to alpha (α) phase transformation was obtained as 369 kJ $mole^{-1}$ employing Kissinger model. The non isothermal KJMA model has been adopted to model the fraction transformed to determine the order and kinetics parameters.

Chapter 6: High temperature thermo-physical and heat transport properties of sigma (σ) and alpha (α) phases

This chapter explains the effect of sigma (σ) phase on thermo-physical and heat transport properties of parent alpha (α) phase. It shows that sigma (σ) phase degrades the thermal conductivity of alpha (α) phase. Enthalpy of both the phases was measured by Drop calorimeter. It was observed that the alpha (α) phase does not undergo any structural phase transformation; however sigma (σ) undergoes a phase transformation of to alpha (α) at 847 °C (1120 K). The enthalpy of transformation was measured as 2.6 kJ $mole^{-1}$. The thermal expansion for alpha (α) and sigma (σ) phases were measured by Thermo mechanical analyzer. The room temperature thermal expansion coefficient for alpha (α) and sigma (σ) phase is 7.39×10^{-6} K^{-1} and 1.5×10^{-5} K^{-1} respectively. The room temperature thermal diffusivity of alpha (α) and sigma (σ) phases were measured as 0.0484 cm^2/s and 0.011 cm^2/s

respectively by Laser Flash Thermal Diffusivity Analyzer. It is observed that sigma (σ) phase formation has adverse effects on heat transport properties of alpha (α) phase. The room temperature thermal conductivity of alpha phase is 16.9 W $m^{-1}s^{-1}$ whereas that of sigma (σ) phase is 3.9 W $m^{-1}s^{-1}$. Further, a comprehensive analytical modeling of experimental thermodynamic parameters has been carried out which shows a good agreement.

Chapter 7: Study of α → γ transformation characteristics in Fe-Cr binary and W added Fe-9Cr ternary and Fe-9Cr-2W multicomponent alloys

This chapter presents the α ↔ γ transformation temperatures for Fe- (1-13 wt.%) Cr alloys and the effect of W on α ↔ γ transformation characteristics in Fe-9Cr alloys and its consequences on martensitic transformation in Fe-9Cr-2W-0.1C (P92) steel. This work shows that beyond 12 wt% Cr, α↔γ transformation is suppressed in Fe-Cr binary alloys, which is lower than the reported value of 14 wt% Cr. Similar observation was made in Fe-9Cr alloy for W addition beyond 1.5 wt%. However, in P92 (Fe-9Cr-2W-0.1C) ferritic-martensitic steel containing 2 wt.% W DSC study revealed the presence of a magnetic transition preceding the martensitic transformation during cooling. The observation supports the co-existence of ferrite and martensite. The formation of diffusional ferrite at high cooling rates is precluded by a systematic variation of three parameters namely cooling rate, austenitising temperature and hold times. Complete martensite formation has not been experimentally observed in P92 steel for all cooling rates (1 - 90 K min^{-1} in DSC and water quenching) during cooling from austenitisation temperatures (1223-1423 K (950 - 1150°C)), unlike in P91 steel where complete martensite structure forms during cooling beyond the critical cooling rate of 30 K min^{-1}. The experimental results have been substantiated by ThermoCalc simulation for varying W contents in P91 and P92 steels. ThermoCalc simulation revealed that P91 steel remains in the single phase γ domain during austenitisation. It is observed that γ phase field shrinks with addition of W. P92 steel remains in the three phase domain of α + γ + MX region at 1223-1423K (950-1150 ^{o}C), which explains the presence of ferrite above Ac_3 temperatures.

<u>Chapter-8</u>: ***Summary and Further Avenues of Research***

Chapter 8 presents a summary of the experimental and modeling studies carried out in this thesis and also identifies few potential avenues for further research.

Chapter - 1

INTRODUCTION

1.1. Ferritic steels: A promising structural material for advanced reactor technologies

The availability of high-performance structural materials is a significant step towards successful design and operation of advanced power plants be it nuclear or fossil fired. The demanding operating environments in liquid metal cooled fast breeder reactor (LMFBR), fusion or advanced coal fired power plants require a wide range of high-performance structural materials for service in high temperatures and stresses, corrosive media, high energy neutrons and electromagnetic radiation. In this context, 9-12 Cr based ferritic/martensitic (F-M) steels and their variants have been identified worldwide as potential materials for core components facing hostile environments in fast reactors. These steels have excellent mechanical properties, radiation and corrosion resistance at moderate temperatures upto 500^{o}C (773 K) [1-6].

The major advantage of ferritic steels over austenitic steels and Ni-based super alloys is the void swelling resistance besides economic viability. However, low creep strength at high temperatures > 550 ^{o}C (823 K) and low fracture toughness are major challenges to be addressed in these steels [6-8]. The F-M steels used in the normalized and tempered condition consist of a tempered martensite microstructure, which imparts the best combination of properties for high temperature applications [9-15]. The martensitic transformation from high temperature austenite (γ) depends upon the stability of the γ phase which in turn is strongly decided by the alloy content. The sub-structure modification of the tempered martensitic structure and coarsening of the carbide precipitates are the main reasons for reduction in strength at elevated temperatures [16-17]. There have been significant efforts to develop F-M steels with higher strength by addition of refractory metals like Ta, W or chemically inert and stable oxide dispersoids [4-9, 18] resulting in the oxide dispersion strengthened (ODS) class of steels. The need for improved corrosion resistance in addition to strength has also led to considerable research activities for development of high Cr ferritic steels [4, 18].

The inherent problems faced by the F-M steels at elevated temperatures are accentuated in the presence of neutron irradiation mainly due to the formation of brittle intermetallic phases like laves and sigma [19-21] and also 475 ^{o}C (748 K) embrittlement [7-8, 22-24]. The 475 ^{o}C (748 K) embrittlement is mainly observed in high Cr ferritic steels and is nucleated by the complex interaction of magnetism and chemistry between ferromagnetic Fe and anti-ferromagnetic Cr atoms. The magnetism induced phase separation of Fe-Cr solid solution (α ferrite) into Fe rich bcc (α') and Cr rich bcc (α'') that results in deterioration of high temperature properties like creep strength, tensile ductility, impact toughness as well as corrosion properties is commonly known as 475 ^{o}C (748 K) embrittlement. Moreover, the brittle intermetallic sigma phase that forms upon prolonged high temperature exposures and under stress is also detrimental to the high temperature mechanical properties. Formation of sigma phase is governed by the stability of Fe-Cr binary phase field at elevated temperature. The kinetics of phase separation and sigma formation may be accelerated or retarded in the presence of other alloying elements in steels. Hence, it is not an exaggeration to say that the attributes of the Fe-Cr phase field are crucial in governing the high temperature phase stability and mechanical properties of high Cr ferritic steels. The knowledge base on thermodynamics, phase stability and phase transformation kinetics of Fe-Cr binary systems is therefore essential in successfully employing ferritic steels to their fullest potential [1-9]. This has provided the necessary motivation for a detailed study of the Fe-Cr binary system for the present thesis. The present worldwide status of understanding of this system will be described in the subsequent sections.

1.2. Unsolved issues in Fe-Cr phase diagram

The Fe-Cr system has been investigated extensively in the past and continues to evoke serious research interest [25-85]; and besides, has critically assessed thermodynamic database. The commonly used Fe-Cr phase diagram shown in **Fig. 1.1** has been established in literature with a great degree of certainty. However, it also emerges that a few issues of fundamental importance, in particular the intricate interplay between magnetic and chemical degrees of freedom and their combined influence in dictating the low and intermediate temperature phase equilibrium are yet to be resolved [39,60,74, 78,83-84]. It is well known that Fe and Cr belong to early 3d-transition metal series, with stable bcc crystal structure at room temperature and ambient pressure. Further, the difference in their atomic volumes and electro-negativities is also small, implying a great degree of chemical similarity. Although, complete solid solution is expected according to Hume Rothery rule, magnetization plays a very crucial role in determining the phase fields in this system. Magnetization measurements and subsequent electronic band structure and total energy calculations have clearly revealed

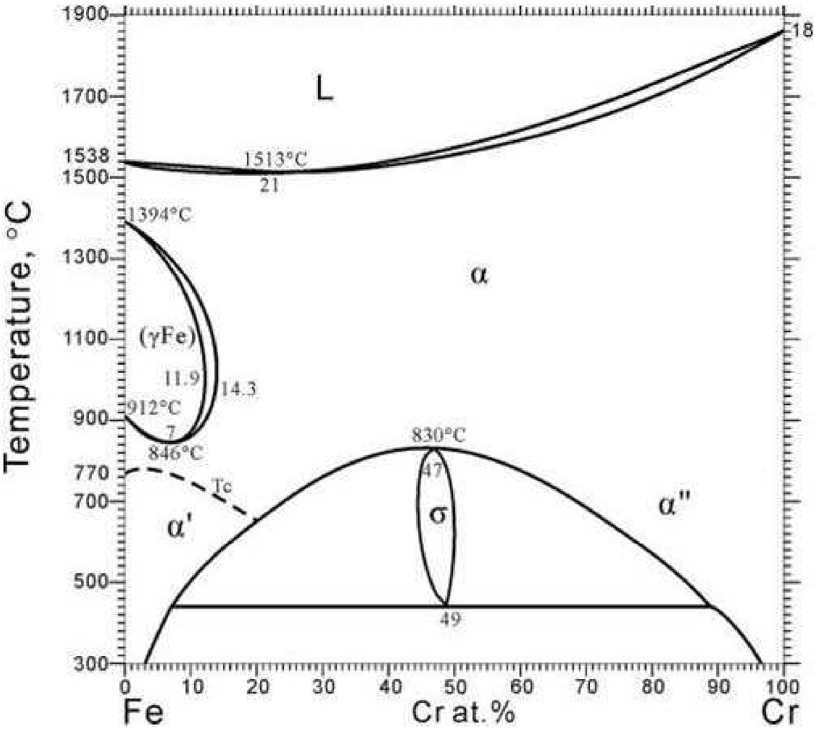

Fig. 1.1 Fe-Cr phase diagram as obtained from the assessment of Xiong et. al [85]

that Fe has ferromagnetic and Cr has anti-ferromagnetic ground state. It is amply evident that even in very dilute concentrations and especially at low temperatures, Cr addition exerts a nontrivial influence on the magnetic ground state character and therefore on the overall constitutional stability of Fe-Cr alloys [39, 60, 64-65, 67, 74, 84-86]. This feature can be illustrated by placing an anti-ferromagnetic Cr atom in ferromagnetic Fe matrix as shown in **Fig. 1.2**. Cr can dissolve and form continuous solid solution in the ferromagnetic Fe matrix until it faces an adjacent Cr atom as its nearest neighbor. The complexity in anti-ferromagnetic spin alignment for Cr atoms with respect to both Fe and Cr atoms which are present in nearest neighbor positions exerts a profound influence and is commonly known as magnetic frustration [66, 87]. Such a situation is driven by two opposing nature of spin interactions and has a tendency to induce a strong anti-magnetic ordering. This magnetic analog of classical chemically induced segregation or clustering behavior operates despite the excellent chemical similarity between Fe and Cr atoms [88]. The magnetic influence is a sensitive function of Cr concentration, for a given temperature and pressure [66]. In other words, the finite low temperature solubility of Cr in α Fe matrix is controlled primarily by promoting magnetically mediated Cr-clustering in a ferromagnetic α Fe matrix [60, 84]. As Cr-concentration is gradually increased, it becomes progressively more difficult to accommodate the increasing number of Fe-Cr near neighbors or next neighbor pairs without a considerable increase in repulsion [60, 84]. Such a situation favors clustering of Cr and eventually restricts the solubility of Cr at an optimal level, wherein the increase in magnetic stabilizing contribution can no longer be compensated by attractive Fe-Cr chemical interaction. The alloy then prefers to exist as a two phase mixture of Fe-rich α’ and Cr-rich α” phase [60, 84-85]. It has been revealed that the prevailing understanding on the equilibrium state of Fe-Cr binary system, especially the Cr solubility in α Fe, is still in an unresolved state [85].

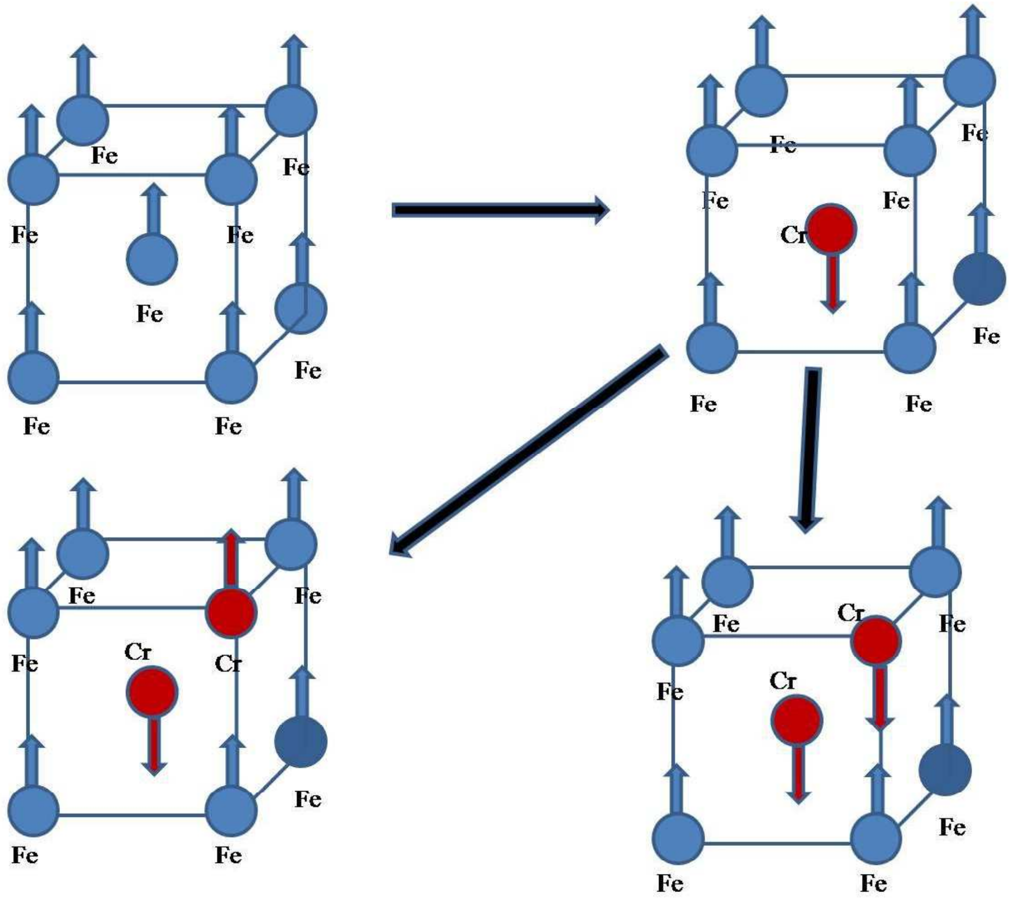

Fig. 1.2 The complexity in anti-ferromagnetic spin alignment for a Cr atomwith respect to both nearest neighbor Fe and Cr atoms, leads to separation of Fe rich and Cr rich clusters.

The huge scatter in the experimental and theoretically modeled data for Cr solubility in α Fe is shown in **Fig. 1.3** which reflects the ambiguity in the phase separation boundary. The maximum Cr solubility in the terminal α Fe solid solution phase is presently considered to be significantly higher than the limits originally set forth by earlier phase diagram assessments [32, 35-36,38- 39, 85] which were based on mostly available high temperature experimental data [25-34, 37, 85]. The earlier thermodynamic assessment of Sundman et al. [36] for Fe-Cr system predicted zero Cr solubility. However, extended Cr solubility of 2 - 7 at. % Cr was reported by several researchers [28, 39, 74-75, 85, 89-92].

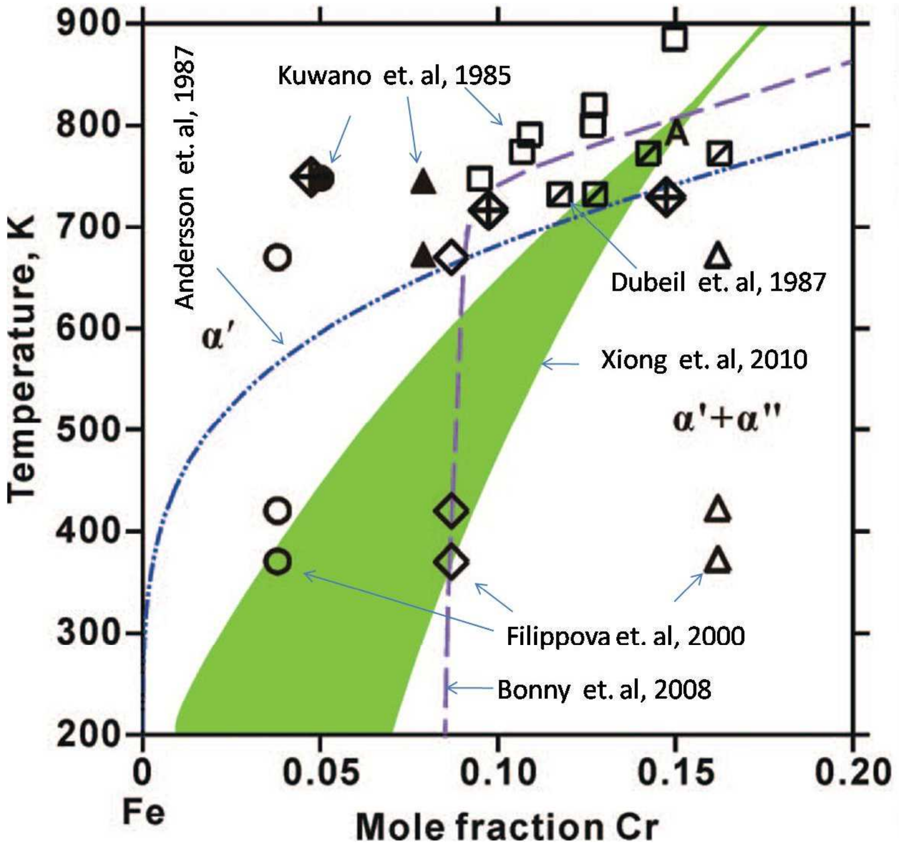

Fig. 1.3 Present status of literature on α phase field of Fe rich region of Fe-Cr phase diagram. Contradiction between experimental and theoretical data of Cr solubility in α Fe is observed. The image has been adopted from the review paper published by Xiong et. al [85]

It is essential to mention here that achieving the equilibrium phase field is very difficult within finite experimental time limits at low temperatures due to the extremely sluggish diffusion of Cr below 500 °C (773 K). The kinetics of phase separation is further accelerated by irradiation [85]. The higher solubility of Cr is supported both by experimental results obtained on long-term homogenized samples [28, 89-92] and theoretical simulations [39, 74-75]. In an early theoretical study by Hennion *et al.*, [60] it is suggested that the standard enthalpy of formation $\Delta^{o}H_{f}$ could actually be mildly negative for Fe rich Fe-Cr alloys, where magnetic effects are expected to control phase stability [66, 93-94]. This aspect also received attention in many subsequent theoretical studies in that, a gradual crossover behavior of $\Delta^{o}H_{f}$ from being mildly negative to strongly positive in character was found with increasing Cr content in the alloy [61-68, 70-76, 80] as shown in **Fig. 1.4**. It is important to note that most of the theoretical calculations are at zero Kelvin temperature, while a few include finite temperature effects as well [74-75].

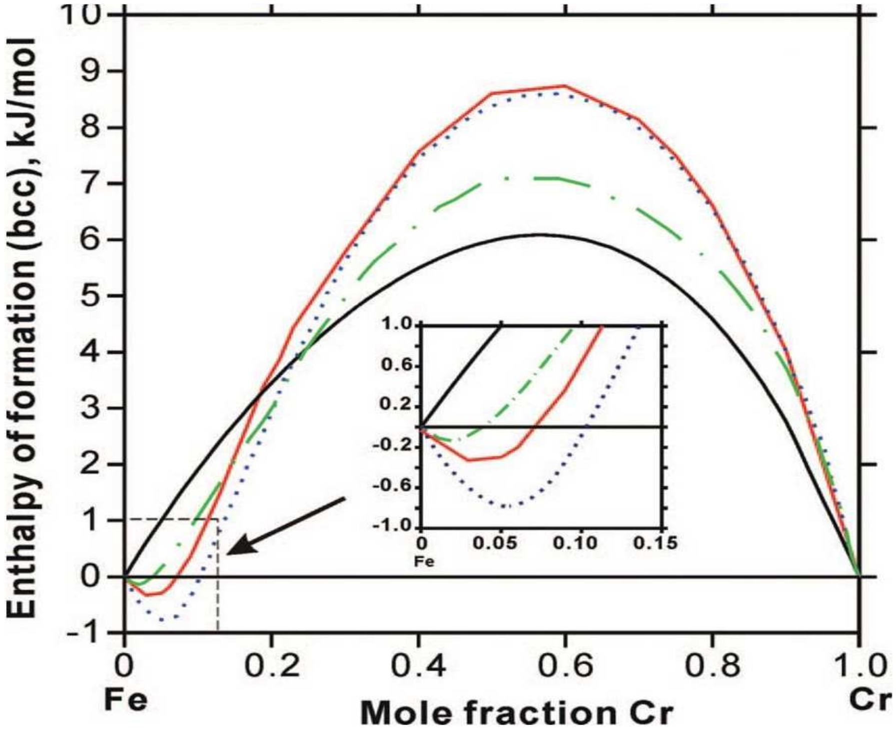

Fig. 1.4 Enthalpy of formation for α (bcc) phase of Fe-Cr alloy shows a gradual crossover at Fe rich side which supports extended solid solution. The image has been reproduced from the review paper published by Xiong et. al [85]

From **Fig. 1.4** it appears certain that in Fe rich composition domain, $\Delta^{o}H_{f}$ could actually assume negative values, where subtle physical effects due to complex magnetic short-range order dictate the solution thermodynamics. On the other hand, the only available high temperature (1327 °C (1600 K)) experimental data due to Dench [25] suggest that $\Delta^{o}H_{f}$ is positive in the entire composition range $Fe_{1-x}Cr_{x}$ ($0<x<1$). It is clear from fundamental thermodynamic considerations that a switch over from negative $\Delta^{o}H_{f}$ for low Cr alloys to strongly positive values for increasing Cr content, is indicative of the crucial interdependence of magnetic and chemical degrees of freedom [94], which can eventually influence the microstructure that evolves in Fe-Cr alloys [46-47]. When magnetic interactions, which are influenced by Cr content and increasing temperature are taken into account in theoretical phase diagram calculations, it appears that a higher equilibrium solubility of Cr in α-Fe solid solution is indeed feasible [39, 74, 80, 91-94]. In line with this hypothesis, Bonny et al. have reported a revised thermodynamic description of Fe-Cr system [39], wherein they suggest extended Cr solubility up to 8 at %. Later, Xiong et al., have also reported a revised Fe-Cr equilibrium diagram, based on a consolidated assessment of available thermodynamic data until 2010 [85] which suggested a band from 2-7 at% instead of a specific phase separation boundary line as observed in **Fig 1.3**. Disparity among different theoretical estimates of Cr solubility in α Fe and in the nature of α'+ α" miscibility gap exists [74, 93]. This disparity partly stems from the diverse theoretical estimates of magnetic contribution to total free energy, the latter arising from approximations made in the treatment of the magnetic part of the total (cohesive) energy.

From the available literature it is clear that the thermodynamics and phase stability of Fe-Cr alloys is influenced by the configurational, vibrational and magnetic contributions to total Gibbs energy. A unique quantitative enunciation of the role of magnetic interactions in Fe-based systems was lacking as there were not sufficient experimental thermodynamic and phase equilibra studies at low and intermediate temperature regions of 400- 600 ^{o}C (673-873 K) [33,40, 85], owing to the difficulty in achieving full thermodynamic equilibrium in a reasonable time frame [48,85]. This has made the quantitative evaluation of magnetic contribution to phase stability difficult using appropriate theoretical framework [94]. Since the pioneering studies of Dench [25] and Normanton *et al.*, [33], there have not been many in-depth calorimetry investigations on Fe-Cr alloys. Inadequacy of data that would help in modeling the energetics of magnetic contribution to Gibbs energy, G [95-98] is again a serious limitation. Besides, there are only few neutron inelastic scattering studies on direct determination of phonon contribution to high temperature thermodynamics in Fe-Cr alloys [54-57]. It is only in the last decade or so that both *ab-initio* and semi empirical computational tools, capable of handling the composite presence of magnetic and chemical short-range order in multicomponent alloys [84], have addressed the issues associated with phase stability calculations [67,68, 95-98]. It is indeed a difficult task to quantitatively model the energies associated with various magnetically ordered spin structures [95]. However, the recent spin polarized density functional theory (DFT) calculations with disordered localized moment have offered some insights into low temperature region of Fe-Cr equilibrium diagram [63-77]. In addition, it is also well known that magnetism is responsible for the anomalous, nonsystematic behavior of many thermo physical properties witnessed in dilute Fe-Cr alloys [85] which is discussed in the next section.

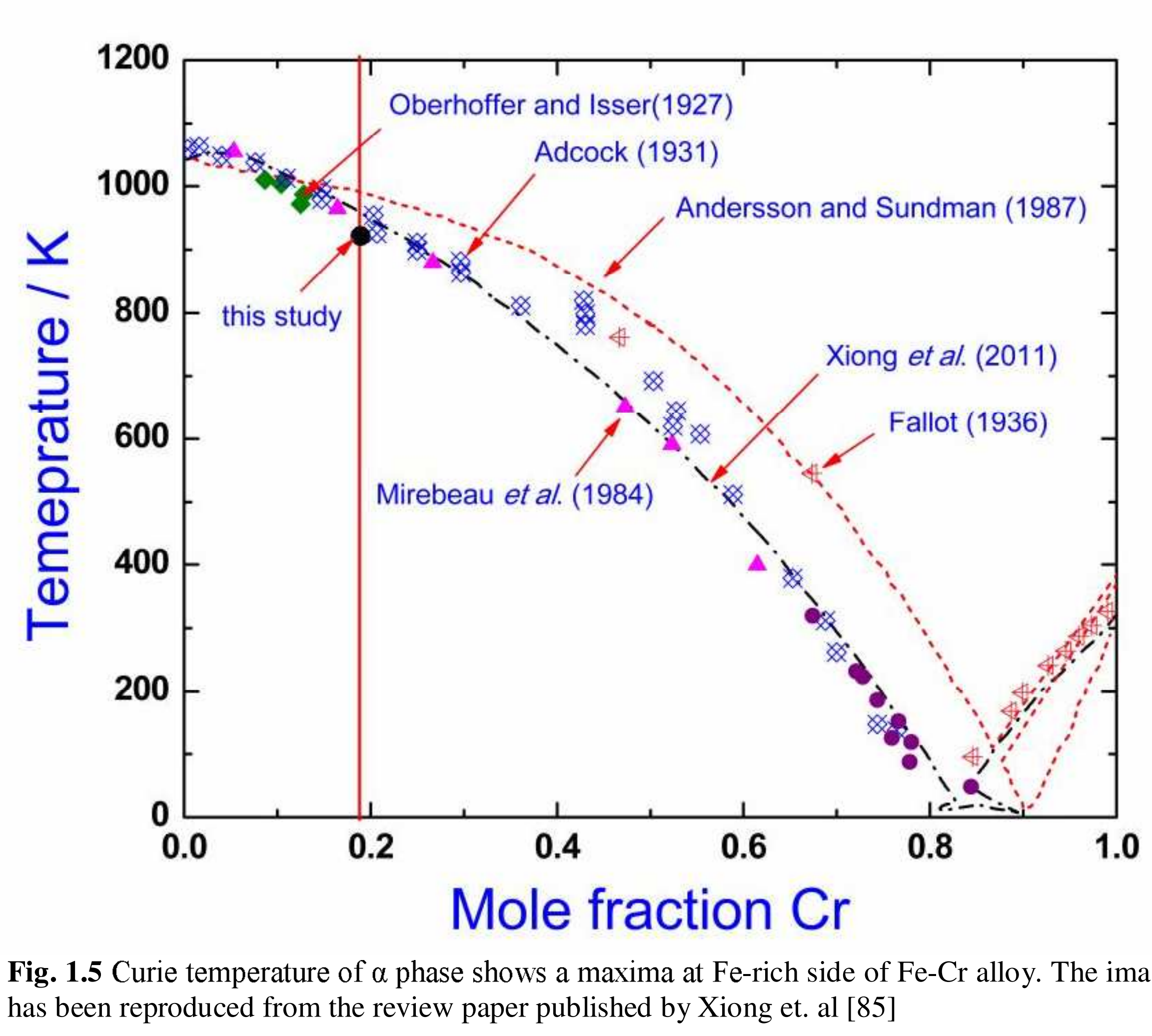

Fig. 1.5 Curie temperature of α phase shows a maxima at Fe-rich side of Fe-Cr alloy. The image has been reproduced from the review paper published by Xiong et. al [85]

1.3. Anomalous behavior of Fe rich α phase of Fe-Cr solid solution

Very dilute solution of Fe-Cr alloys in Fe rich region exhibits interesting properties [63-80, 85, 95- 98] and has drawn considerable attention in the last few decades. Contrary to an expected decreasing trend in Curie temperature (T_c) of α phase in Fe-Cr alloy from pure Fe to pure Cr, as a consequence of anti-ferromagnetic coupling, a local maxima is reported [40,85] at ~ 4 at % of Cr followed by a monotonous decrease as shown in **Fig. 1.5**.

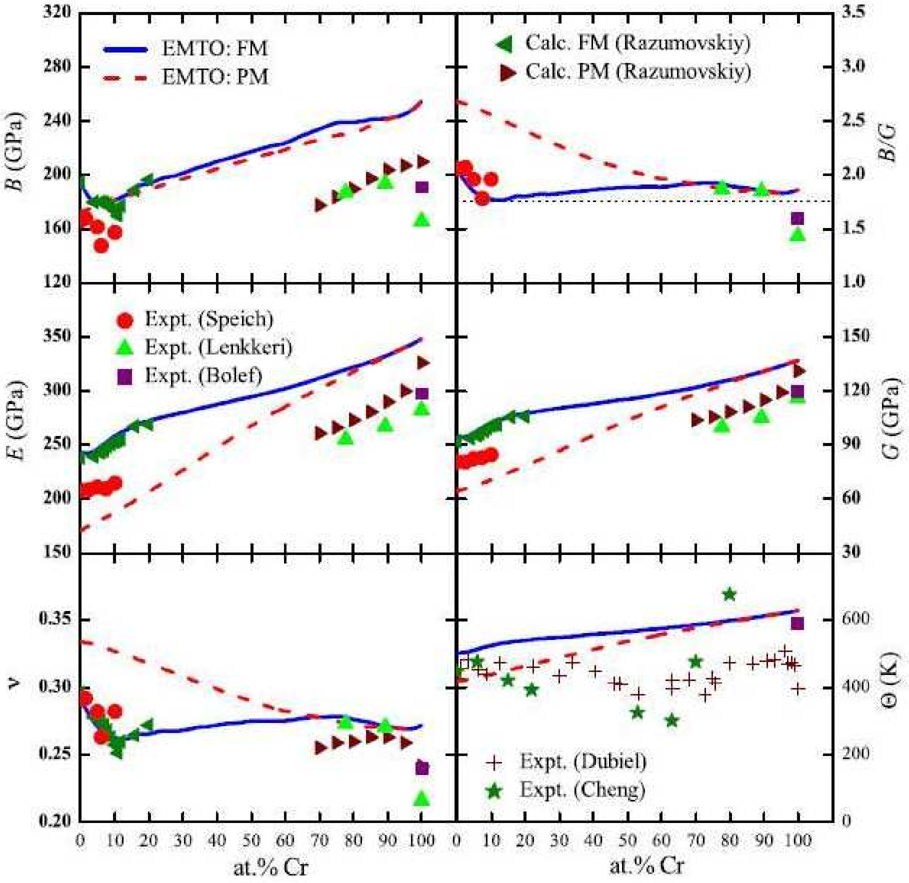

Fig. 1.6 Bulk modulus (B), Young's modulus (E), Poission ratio (ν), Debye temperature (θ) of α phase shows minima at Fe-rich side of Fe-Cr alloy. The image has been reproduced from the paper published by Zhang et. al [77].

Recently, Xiong et al [40] have reported a higher T_c (by 11 K) for Fe-3.34 at% Cr alloy than pure Fe. An irregular trend has also been reported for lattice parameter value [61, 65, 72, 74]. The theoretically calculated lattice parameter shows a maxima at low Cr region on Fe rich side whereas the experimental lattice parameter of Fe-Cr system increases monotonously from Fe to Cr. An unusual trend in elastic moduli of Fe rich Fe-Cr alloy in the low Cr region has also been reported [72, 77]. First principle calculation [72, 77] reports an initial decrease in elastic moduli and Poissons ratio (**Fig. 1.5**) with addition of Cr which reaches a minimum at ~ 5-6 at% Cr and then increases up to pure Cr. An exhaustive study of literature in this system re-affirms the fact that the magnetic interaction between Cr and Fe particularly on the Fe rich side remains unresolved and requires further studies.

1.4. Unsolved issues of Sigma phase in Fe-Cr system

Formation of brittle sigma phase is one of the major reasons for degradation of properties in high Cr ferritic steels, austenitic steels and their weldments. σ phase has been reported to form after long term exposure to elevated temperature (>400 °C (673 K)) in ferritic [99-100], austenitic [101-103] and duplex steels [20, 104-105] as well as in Fe-Cr based binary [21,85,106-107] and ternary systems [108-110]. Formation of σ phase affects the creep ductility [111], low cycle fatigue behaviour [112] and corrosion resistance [113] of structural materials. The volume fraction, size and distribution is important as very fine size σ precipitates are reported to be beneficial, imparting dispersion hardening to the matrix phase [114]. A systematic decrease in ductility with volume fraction of σ in SS310 is reported [115]. A similar correlation between volume fraction of σ and creep strength [114] and fracture toughness is also reported [116]. Many in-service failures are also reported due to σ-phase formation. Chastell and Flewitt [117] in the year 1979 reported the premature failure of SS 316 secondary super heater boiler tube due to enhanced creep cavitation associated with σ formation. ER SS 309L welds containing δ-ferrite exhibited 85% reduction in toughness after ageing at 700 °C (973 K) for 2 h, due to $\delta \rightarrow \sigma$ transformation [118]. Prolonged heating at temperatures higher than 650 °C (923 K), embrittled austenitic stainless steel weld joints due to σ formation [119]. Accelerated ageing of GTAW welds of SS 316FR also leads to the nucleation of σ at δ/γ interphase boundary which was predicted to affect the repair weldability of the steel [120].

Sigma (σ) phase has tetragonal crystal structure which was first identified by Bergman and Shoemaker [121]. It has tetragonal (space group 136, *P*42/*mnm*) unit cell with 30 atoms. The partially disordered character is the special feature of sigma (σ) phase unlike other intermetallics, which arises because of substitution of various sites in the crystal structure [122] owing to which it can exist over a wide range of composition. There are three different sublattice models which have been proposed for sigma phase in Fe - Cr alloy. Anderson and Sundman [36] first used the sublattice model with the formula of $(Cr)_4(Fe,Cr)_{18}(Fe)_8$ which has been modified later as $(Cr)_4(Fe,Cr)_{16}(Fe)_{10}$ [123]. Simple two sublattice model with formula $(Fe,Cr)_{20}(Fe, Cr)_{10}$ was used by Joubert [122]. Several experimental and theoretical studies have been carried out to construct the sigma (σ) phase field in Fe- Cr phase diagram [21, 85, 122]. However, this task was challenging because of experimental difficulties due to the highly sluggish kinetics of alpha to sigma transformation which requires very long-term annealing as well as due to the existing experimental disagreements [21, 85, 122]. The temperature range for sigma (σ) phase formation in Fe-Cr system has been reported over a wide range of temperatures from 460 to 650 ^{o}C (733 to 923K) by various authors [44, 124-131]. The pioneering study of Dubeil et al [48] wherein five Fe - Cr alloys were annealed for time periods of four to eleven years is considered as the most reliable one. Based on this study, the start temperature of sigma (σ) formation is reported as 500-510 ^{o}C (773-783 K) [110]. Similar controversy exists for the upper temperature limits of sigma (σ) phase field where a wide temperature range of 820-930 ^{o}C (1093 to 1203 K) has been reported by various authors [132-136]. Cook et. al [132] predicted 820 ^{o}C (1093 K) as the maximum temperature upto which σ phase existed based on XRD study on Fe - 47 at % Cr alloy which was supported by the thermal analysis study by Pomey et. al [134]. Baerlecken et. al [133] claimed the maximum limit for sigma (σ) phase field as 930 °C (1203 K). However, Kubaschewski [136] in 1982 reported the maximum temperature of sigma (σ) as 830 °C (1103 K), which was slightly higher than 820 °C (1093 K) reported by Cook et al [132]. Finally, 820 °C (1093 K) was accepted as the upper limit of sigma (σ) phase field as per the latest Fe - Cr phase diagram reported by Xiong et. al [85]. It is worth mentioning here that Cook et. al [132] predicted the high temperature limit of sigma phase field by XRD and metallography which is a static method of phase identification. Only thermal analysis study reported by Pomey et. al [134] in 1956 supports the data of Cook et al [132]. Thereafter, no thermal characterization studies are reported to resolve the ambiguous σ → α phase transformation although few studies have been carried out for measurement of specific heat of Fe-Cr alloys [34, 50, 137-138]. In 1958, Backhurst [137] measured the specific heat from 727 ^{0}C (1000-1400K) for the alpha phase of $Fe_{55}Cr_{45}$ alloy. Malinsky et. al [138] measured the specific heat of alpha phase of $Fe_{55}Cr_{45}$ alloy from 827 – 1427 ^{0}C (1100-1700K). In 1984, Downie et. al [34] measured the specific heat for both alpha (α) and sigma (σ) phases by DSC upto 727 ^{0}C (1000 K). Hence, the σ → α phase transformation event in the σ phase field of Fe-Cr phase diagram has not been extensively characterized by thermal analysis. It was therefore found necessary to revisit the sigma to alpha phase transformation event using high precision calorimetry techniques to identify the σ → α transformation unlike the reverse transformation of α → σ. Another interesting aspect of σ phase field is the range of Cr compositions over which it existed as large variation have been reported [128,130,132,134,139]. Initially, 44 - 50 at.% range of Cr was reported by Cook et. al [132] which was supported by Ettwig et. al [128] and Zeedijk et. al [139]. Later, Pomey et. al [134] reported 42-51 at.% Cr over which σ phase existed in Fe -Cr alloy, which was further modified to 41-51 at.% by Cerezo et. al [130]. In the recent optimization by Xiong et. al [85], the range of sigma (σ) phase field is reported as 42-50 at.% Cr.

The kinetics of sigma (σ) formation in the presence of various alloying elements has been studied by various authors [109-110, 140-144]. Advanced high Cr ferritic steels contain several alloying elements namely Mo, Ti, V, Nb, Si etc. to improve the overall physical and mechanical properties. It is therefore essential to explore the effect of these alloying elements on the kinetics of α → σ phase transformation. It is worth mentioning here that the sluggish kinetics of α → σ phase transformation cannot be arrested by dynamic thermal analysis technique. Therefore, α →σ phase transformation kinetics has been studied using static phase identification techniques mostly in-situ Mossbauer spectroscopy. Elements like Ti [109-110], Si [140-141], Mn [141], Mo [142] and Zr [143] have a tendency to accelerate the α → σ kinetics. Sn [144] has been reported as the only exception to retard the α → σ kinetics. Interesting features have been reported for Ti by Mossbauer study [109-110]. Ti accelerates the kinetics of α → σ upto 1.5 at. % and beyond that there is a reversal in the trend. Although α → σ phase transformation has been studied extensively, the reverse kinetics of σ → α phase transformation has not been investigated except for few studies using Mossbauer technique [41,145]. There is no calorimetric study reported on the kinetics of σ → α phase transformation.

1.5. Characteristics of α↔γ transformation in Fe-Cr system

The martensite structure in 9 Cr based ferritic/martensitic steel is the result of fast cooling after solution treatment from austenite (γ) phase field. The bcc ferrite phase is transformed completely to the fcc austenite phase after dissolution of carbides, thus enriching the austenite with carbon which stabilizes the γ phase. During fast cooling, the dissolved carbon is trapped in ferrite leading to diffusionless transformation to martensite. It is required to mention here that there exists a huge scatter in the experimental data for austenite phase field of Fe-Cr binary system as shown in **Fig. 1.7**. This phase field was optimized by Sundman et.al in 1982 [36]. Since then there has been no calorimetric study which dealt with α→γ phase field. It is established that the addition of refractory solutes like Mo, W and Ta to steels usually shifts the *γ* phase field to higher temperatures. It is important to mention here that W added 9Cr steel has attracted considerable attention in the development of economic creep resistant materials [12-18, 146-156].

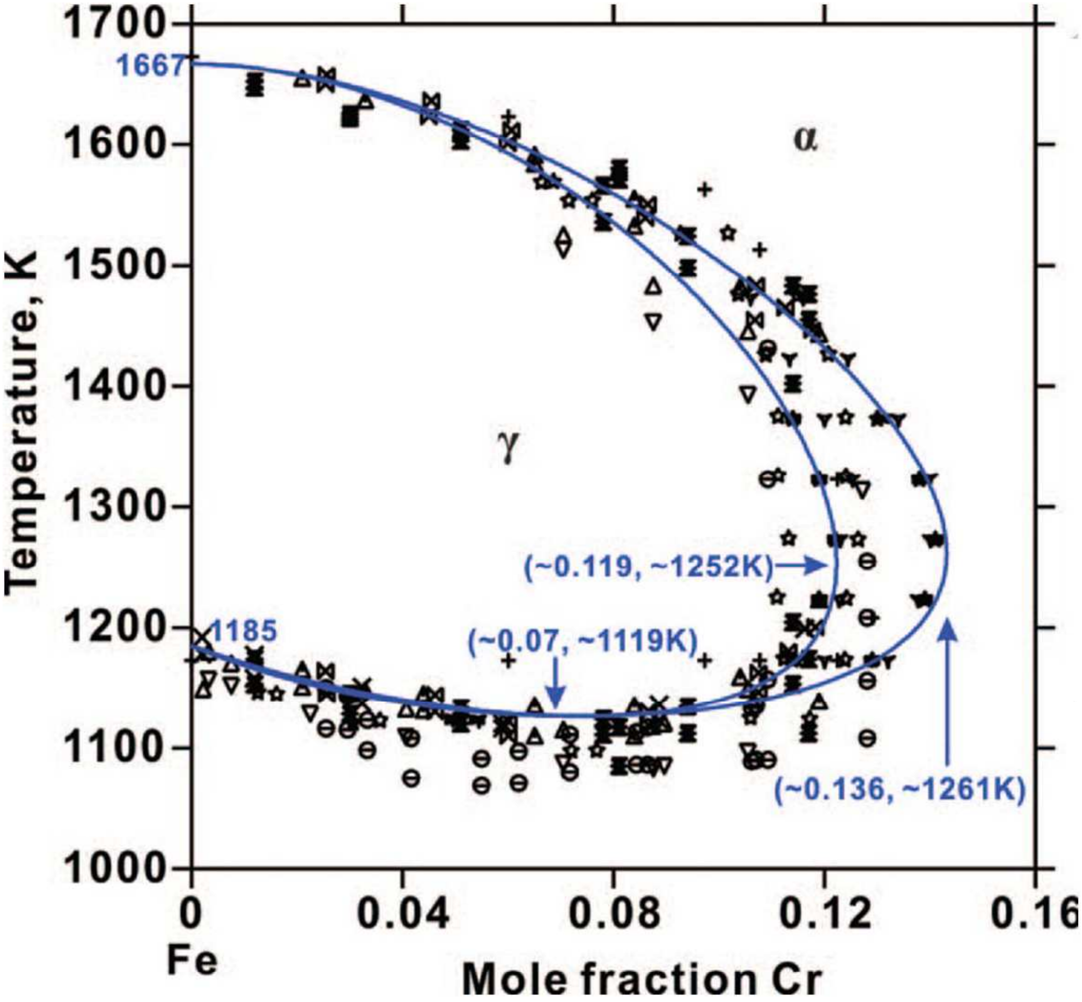

Fig. 1.7 Present status of γ phase field in Fe-Cr system as depicted by Xiong et. al [85] showing huge scatter in experimental data

Moreover, the development of reduced activation ferritic martensitic steels (RAFM) for fusion reactors, wherein Mo is replaced by W in P91 steel is based on the enhanced strength achieved in addition to addressing the activation problem [146-156]. An increase of W from 1 to 2 wt. % is reported to help in retaining the lath martensite structure [151] as it retards the coarsening of $M_{23}C_6$ precipitates during long term thermal exposures [155].

However, the addition of W is also reported to have adverse effects as it retards the martensite formation [147, 150, 152-153]. It is observed that addition of W to 9Cr F-M steels has resulted in the formation of undesired ferrite phase along with martensite even under fast cooling conditions [150, 152-153, 156] which has adverse effect on creep properties. The presence of W in $M_{23}C_6$ also influences its dissolution kinetics, which in turn would alter the transformations characteristics at high temperature. Therefore, the role of W addition on transformation behaviour of Fe-9Cr binary alloy and Fe-9Cr-0.1C multi component alloy needs to be understood. In this background, $\alpha \leftrightarrow \gamma$ transformation temperatures for Fe - (1-13 wt. %) Cr alloys and the effect of W on $\alpha \leftrightarrow \gamma$ transformation characteristics in Fe-9Cr alloys and its consequences on Fe-9Cr-2W-0.1C (P92) multicomponent alloy have been explored in the present thesis.

1.6. Scope of the present thesis

A detailed study of literature has enabled the identification of few gaps in the understanding of phase stability and transformations in Fe-Cr binary and related systems, which has provided the scope for an in-depth experimental and modeling study. In view of the above, present thesis has been taken up to resolve some of the issues namely the investigations on the high temperature thermal stability and thermo-physical properties of Fe-Cr alloys. It also includes the synthesis of σ phase from its parent α phase in Fe-Cr model alloys, study of $\sigma \rightarrow \alpha$ transformation characteristics and the effect of σ phase on the thermal and heat transport properties of α phase. The main themes that have been addressed are as follows:

- Study of equilibrium thermodynamic properties in the anomalous domain of Fe rich dilute Fe-Cr alloy by calorimetry techniques
- Influence of phase separation on thermo physical properties of Fe-Cr alloy system

- Characteristics of $\sigma \leftrightarrow \alpha$ transformation and the temperature limit of sigma phase field in Fe-Cr alloys by calorimetry experiments
- Heat transport and thermo-physical properties of alpha and sigma phases.
- Role of tungsten addition on the $\alpha \leftrightarrow \gamma$ transformation characteristics in Fe-Cr based ternary and multicomponent alloys

Chapter-2

Experimental Methodology

2.1. Experimental methods

Several experimental techniques and modelling tools have been employed for the characterization and measurement of high temperature phase stability, thermo-physical and transport properties of Fe-Cr based alloys. The major experimental techniques used for thermo-physical properties and kinetic measurements are static and dynamic calorimetry. Static calorimetry is used for measurement of enthalpy increment under pseudo equilibrium conditions, while dynamic calorimetry is employed to study the high temperature phase stability and kinetic aspects of phase transformations under non-isothermal conditions. Dilatometry technique was also employed for measurement of temperature dependent thermal expansivity. Laser flash thermal diffusivity technique was employed to measure the temperature dependent thermal diffusivity and thermal conductivity.

Beside these major experimental tools, other supporting techniques such as optical microscopy, scanning electron microscopy (SEM), transmission electron microscopy (TEM), microhardness and X-ray diffraction (XRD) were also employed in this study. The present chapter briefly describes the details of alloy preparation, composition and heat treatments. This is followed by a detailed description on the static and dynamic calorimetry, dilatometry and laser flash thermal diffusivity techniques. Finally, the specimen preparation methods and operating conditions for the characterization techniques such as optical microscopy, SEM, TEM, hardness and X-ray diffraction (XRD) is included.

2.2. Alloy preparation, compositional analysis and heat treatment

The alloy systems investigated in this study are Fe-Cr binary alloys, W added Fe-9Cr and 9 Cr based ferritic martensitic steel. Accurately weighed stoichiometric quantities of pure Fe (99.99 *wt.%* Sigma Aldrich) and Cr (99.99 *wt.%* Sigma Aldrich) pieces was arc-melted in water cooled copper hearth using tungsten electrode, under flowing high pure He to synthesize the Fe-Cr and Fe-Cr-W alloys. The alloys were re-melted three to four times in order to obtain a homogeneous product. The average mass of each ingot was about 5 g and the weight loss after melting was found to be less than 1%. The alloys were subsequently vacuum sealed in argon purged quartz tube and homogenized at 1273 K for about 10 h. After homogenization, the alloys were furnace cooled to room temperature. The chemical composition of the homogenized Fe-Cr and Fe-9Cr-W alloys was analyzed by inductively coupled plasma - optical emission spectroscopy (ICP-OES) technique and is given in **Table 2.1** and **Table 2.2** respectively.

Table 2.1
Chemical composition of Fe - Cr binary alloy

Alloy	Cr (wt.%) (uncertainty ± 0.01)	C (ppm) By mass	Fe (wt.%) (uncertainty ± 0.01)
Fe -1Cr	1.043	32	Balance
Fe-3Cr	2.967	25	Balance
Fe-5Cr	4.983	17	Balance
Fe-9Cr	9.118	25	Balance
Fe-11Cr	11.012	18	Balance
Fe-12Cr	11.985	28	Balance
Fe-15Cr	14.865	30	Balance
Fe-20Cr	20.159	45	Balance
Fe-45Cr	44.665	40	Balance

Multi-component alloy (P92 and P91 steel) plates were supplied by MIDHANI, Hyderabad, India in the normalized and tempered condition. The composition of the sample was determined by ICP-OES technique and is listed in **Table 2.3**. Strips of dimension of 50 X 25 X 10 mm^3 were cut from the plate and solution treated at 1050 ^oC (1323 K) for two hours and water quenched followed by tempering for 1h at 770 ^oC (1043K) for further study.

Table 2.2
Chemical composition of Fe-9Cr-W alloy

Alloy	Cr (wt.%) (uncertainty ± 0.01)	W (wt.%) (uncertainty ± 0.01)	Fe (wt.%) (uncertainty ± 0.01)
Fe-9Cr-0.5W	9.145	0.492	Balance
Fe-9Cr-1W	8.971	1.019	Balance
Fe-9Cr-1.5W	8.919	1.458	Balance
Fe-9Cr-2W	9.056	2.089	Balance

2.3. Basic principles of calorimetry

The basic principle of calorimetry is based on the quantitative measurement of the temperature or its difference in terms of the heat transfer between a sample and a reference under thermal equilibrium [157]. The heat transferred under adiabatic condition is directly proportional to the temperature difference. The relationship between the heat (Q) that is transferred and the change in temperature (ΔT) is given as

$$Q = C(T)\,\Delta T \tag{2.1}$$

In the above equation the parameter *C(T)* is the calorimeter constant, which is generally evaluated using suitable standards with known heat capacity under identical and reproducible conditions.

In a dynamic calorimetry technique the thermal response of a system is monitored as a function of time, during which the temperature of the sample is continuously changing. Therefore, in a dynamic or scanning technique, the measurement is often performed under *non-equilibrium* conditions which can be put to effective use for studying a variety of non equilibrium phenomenon, such as phase transitions, relaxation phenomenon etc [158]. The static calorimetry technique on the other hand is useful in studying the time dependent stability at a fixed temperature which is suited for making equilibrium thermodynamic property measurements of a stable phase as a function of temperature.

Table 2.3

Chemical composition of P91 and P92 steels used in the present study

	Cr	Mo	W	C	Mn	Si	V	Nb	N	Al	Ti	Ni
P91	9.12	0.95	-	0.1	0.40	0.30	0.21	0.07	0.02	0.02	0.002	0.35
P92	9.20	0.51	1.9	0.1	0.36	0.27	0.22	0.07	0.05	0.01	0.002	0.06

2.3.1. Drop and inverse drop calorimetry

In a direct drop calorimeter the relative enthalpy of a specimen at a chosen temperature T is measured with respect to its value at the reference temperature (usually taken as 298.15 K). This is realized by heating the sample to a desired temperature and after equilibration at this temperature for a certain duration, it is dropped into a well-equilibrated calorimeter block or bed that is maintained at fixed reference temperature. The rise in temperature of the calorimeter bed due to the heat transferred from the sample is measured maintaining near-adiabatic conditions. The experiment is usually repeated by dropping the reference calibrant of known mass and known enthalpy under identical experimental conditions to evaluate the calorimeter constant. This calorimeter constant is used to calculate the enthalpy for the sample from the measured heat flow at a fixed temperature. It must be mentioned here that, some thermal loss mechanisms, such as due to radiation are invariably present in any calorimetry set up. However, the heat loss is minimized in a good calorimeter design. The net heat change Q is determined as:

$$Q = C\,(T)\,\Delta V \Delta t \qquad (2.2)$$

Where $C(T)$ is the usual calibration constant which is determined by calibration with known enthalpy standards like α-alumina. The parameter ΔV (in microvolts) stands for the thermopile output which is continuously monitored with time until thermal equilibration ($\Delta T \sim 0$) is complete. By determining $Q(T)$ as a function of temperature T, the curve of enthalpy versus sample temperature is readily obtained. A typical enthalpy or drop curve is shown in **Fig.2.1.** It indicates a sharp change in the enthalpy that is associated with a phase transformation event. In cases where the transformation occurs over a temperature range, the enthalpy exhibits a gradual change of slope. A continuous enthalpy increment versus temperature data is not obtained through drop calorimetry. This has an important bearing on the precise fixation of the transformation temperatures, although the enthalpy change accompanying phase changes are accurately obtained from drop calorimetry.

As the name suggests, in the inverse drop calorimetry mode, the sample at room temperature is dropped into the hot calorimeter bed. The principal advantage of this inverse drop mode over the direct one is that the heat losses due to dropping of hot sample are minimized [159]. Inverse calorimetry has several advantages; namely (i) easily adoptable for small size specimen, (ii) avoids retention of any metastable phase due to high temperature excursion and (iii) useful to study different types of chemical reactions [160]. Inverse drop calorimetry has been extensively used in the present study for measurement of enthalpy increment, which is described in the following section.

2.3.2. Instrument details

In this study a “Multi Detector *HTC Drop Calorimeter 96” supplied by Setaram®,* France has been used. The experimental setup and instrument details are depicted in **Fig. 2.2** and **Fig. 2.3** respectively.

(i) High temperature furnace

The high temperature graphite furnace, supported by the cabinet’s top plate of the calorimeter is displayed in **Fig. 2.3 (a).** A sealed alumina tube running from the top portion of the furnace into the bottom separates the experimental chamber from the furnace atmosphere.

(ii) Measurement head – drop transducer

The experimental chamber containing the transducer is usually called the drop transducer or detector whose cross sectional view is displayed in **Fig. 2.3 (b)**.

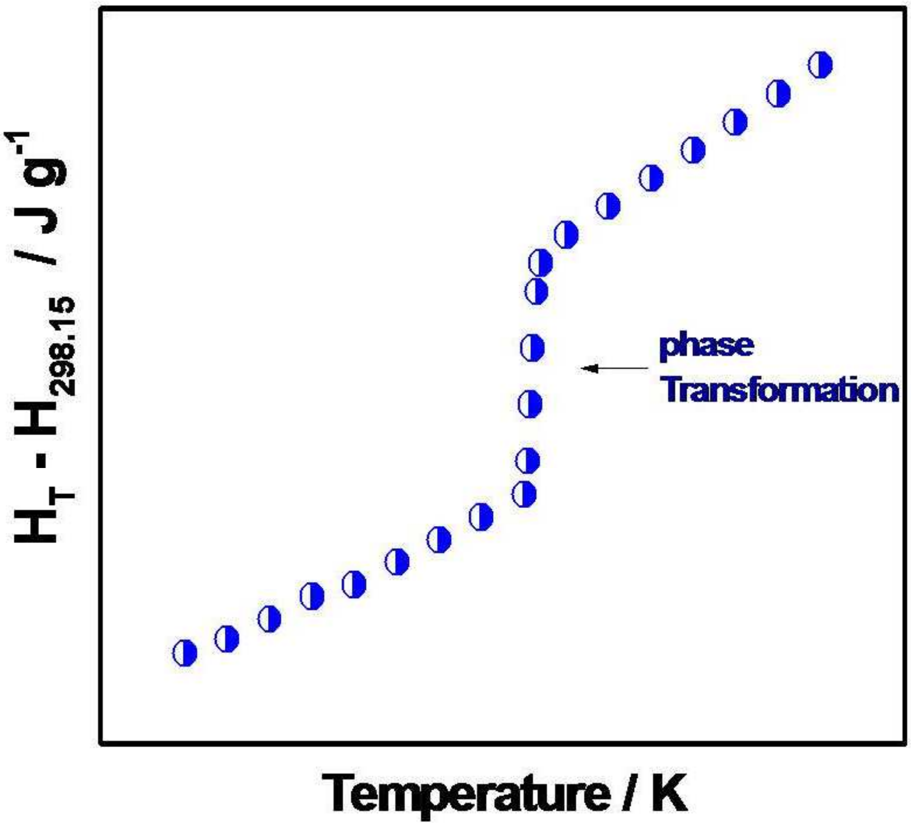

Fig. 2.1 Schematic of the temperature dependent enthalpy increment

This measurement head itself is an integrated structure made of a cylindrical recrystallized alumina tube in which two grooves are cut at its bottom to introduce the sample crucible. The crucible has a working volume of 6.25 cm^3 with dimensions 16.20 mm in diameter and 44.50 mm in height. The temperature of the measuring crucible is monitored by a thermo-cell made of 28 B-type thermocouples distributed over the bottom and along the side of the crucibles. A dummy reference crucible having an identical thermo-cell arrangement is kept beneath the sample crucible. This vertically aligned arrangement of the sample and reference crucible is placed in the uniform temperature zone of the graphite furnace. Measurement of the sample and furnace temperatures is done by two thermocouples of B type (PtRh-6% / PtRh-20%).

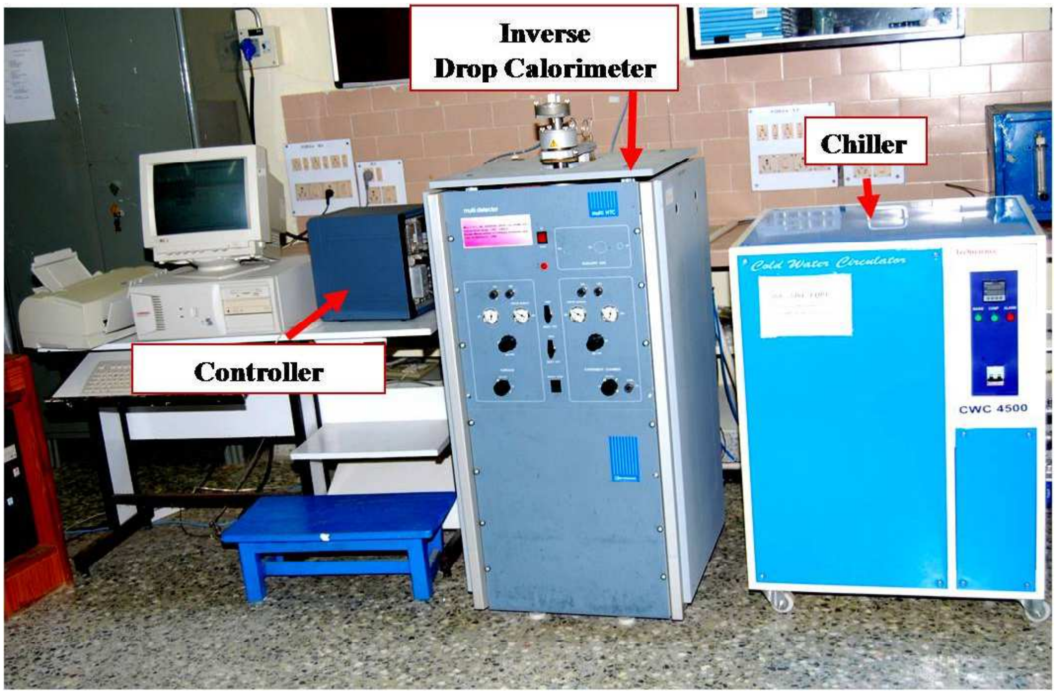

Fig. 2.2 The experimental setup of Inverse Drop Calorimeter

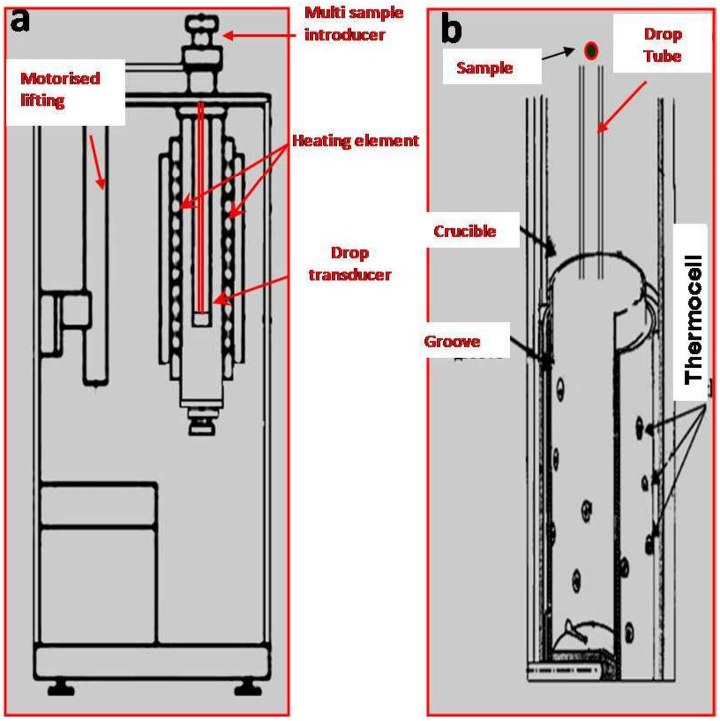

Fig. 2.3(a) High temperature furnace with cabinet **(b)** Measurement Head

(iii) Multi-sample introducer and the drop tube

The multi sample introducer equipped at the top portion of the experimental chamber provides 23 slots to load samples into it. Normally four to six samples are loaded for each measurement. For each sample, a reference sample is also loaded in the adjacent slot. The drop tube called sample-guiding tube guides the sample to fall exactly into the sample crucible during the course of the experiment.

(iv) Gas, vacuum, chill-water circuit and controller

The equipment contains two separate gas circuits, one for the furnace and another for the analysis chamber to maintain the required inert gas atmosphere. An external rotary vacuum pump (EDWARDS) supplied by *Setaram*® is used for evacuating both the experimental and furnace chambers before starting the experiment. An external chill water supply with controlled flow (*Julabo FC 1600 T*) is provided for the furnace cooling. The heating schedule programming, the data acquisition and storage are carried out through the *RS 232*controller interfaced with the personal computer. In the following section, the procedure for performing inverse drop calorimetry experiment is discussed.

2.3.3. Experimental procedure

Samples of dimension (2x2x2) mm and mass 50-75 mg were prepared and loaded in the specimen slots of the multi sample introducer. The standard alumina (α - Al_2O_3) samples weighing 66.8 *mg* (supplied by M/s. Setaram) are also loaded into respective vacant slots. After loading the samples and setting the working crucible in its position, the experimental as well as the furnace chambers are evacuated and flushed with high purity argon gas a few times. When the pressure of argon gas attains one atmosphere in both chambers, circulation of the chilled water supply is started. Then the furnace is gradually heated to a desired temperature at a rate of 3–5 K min^{-1} to a pre-set value within an accuracy of ±0.1 K, the respective samples are dropped into the hot alumina bed through the guiding ceramic drop tube. The heat absorbed by the sample upon dropping produces a sudden change in the temperature of the alumina bed. The thermo-cell measures the temperature difference between the sample and reference and the typical integrated output is given as ΔV vs. time (t) as shown in **Fig. 2.4.** The *RS 232* controller serially interfaced with the computer provides for this digital conversion. An identical experiment is carried out at the same temperature by dropping the known mass of calibration standard to quantify the heat flux, which is measured as area under the ΔV vs. time curve [161]. The typical time for the data acquisition is about 20 to 25 minutes for each drop and after each measurement a time of about 30 minutes is allowed to elapse between successive drops. Normally, about two drops are carried out for each temperature in order to monitor the intrinsic scatter associated with the experiment at any temperature. A total of three experimental schedules covering the temperature range of 400 to 1273 K are conducted. Each experimental schedule consists of a series of successive drop experiments carried out at prefixed discrete temperature steps (approximately 25 K).

2.3.4. Calibration of drop calorimeter

Prior to actual measurements, the temperature of the calorimeter is calibrated by melting of pure element standards such as In, Sn, Al, Ag, Au and Cu. The heat change (Q) calibration is made by dropping the α-alumina standard reference material. The performance of the thermo-cell is also monitored by repeatedly observing the standard deviation of the value of heat change (Q) of the standard α - alumina in the temperature range 200 – 1100 ^{0}C (473 to 1373 K). The temperature variation of Q measured over one typical experimental schedule is graphically shown in **Fig. 2.5.** In this figure, an inset is shown for a typical sensitivity curve used for enthalpy evaluation. The polynomial fit expression used is: $a+b\mathrm{T}+c\mathrm{T}^2+d\mathrm{T}^3$ and the fit coefficients obtained are: $a = 0.248 \pm 0.078$, $b = 7.84 \pm 2\times10^{-4}$, $c = 8.795 \pm 3\times10^{-8}$, $d = -2.5 \pm 1\times10^{-10}$. Different symbols in the figure correspond to different sets of data obtained at different instances of time with standard α-alumina. The individual data points of Q quoted here are taken from more than 10 different experimental runs that have been carried out on alumina when used as the standard during enthalpy measurement. It is found that the standard deviation (σ) of Q is less than 5 up to 537 ^{0}C (810 K) and is less than 15 for higher temperatures.

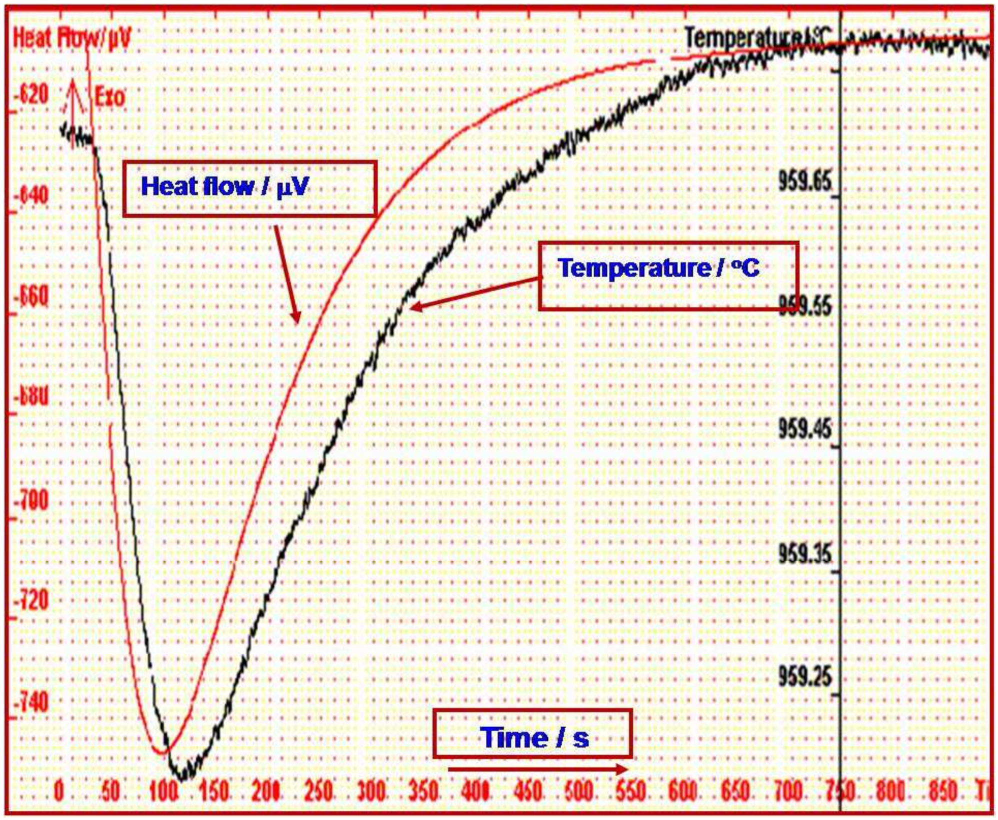

Fig. 2.4 Snapshot of the output signal from the drop calorimeter

2.3.5 Estimation of Enthalpy

Assuming that quasi-adiabatic conditions are maintained in the experimental chamber, the heat energy transported ($Q_S(T)$) from the hot alumina bed to the cold sample can be written as:

$$Q_S\,(T) = C(T) \times (m_S / M_S) \times (H_T – H_{298.15})_S \qquad (2.3)$$

In the above expression, m_S is the mass of the sample, M_S its molecular weight, $(H_T – H_{298.15})_S$ is the measured enthalpy increment with respect to the reference temperature 25 ^{0}C (298 K) and $C(T)$ is the temperature dependent calibration constant. The calibration constant can be obtained from the heat change $Q_R\ (T)$ recorded with the standard alumina reference drop, whose critically assessed enthalpy values are known from literature [162-163]. Thus

$$Q_R\,(T) = C\,(T) \times (m_R\,/\,M_R) \times (H_T\text{–}H_{298.15})_R \qquad (2.4)$$

In this equation, m_R is the mass of the reference and M_R its molecular weight which is taken to be 101.96 Kg m^{-3} [162]. It is worth noting that $C(T)$ remains the same in both expressions. Considering Eq. (2.3) and (2.4) together, it is clear that the quantities $Q_S(T)$, $Q_R(T)$, (heat flux transferred between the sample, reference and the alumina bed) are measured at each temperature, as the respective area under the peak. The quantity $C(T)$, the calibration constant is obtained by substituting in Eq.(2.4) the known enthalpy value $(H_T\text{–}H_{298.15})_R$ of standard reference for each temperature. This calibration constant, $C(T)$ is subsequently used to determine the unknown enthalpy $(H_T\text{–}H_{298.15})_S$ of the sample at each temperature.

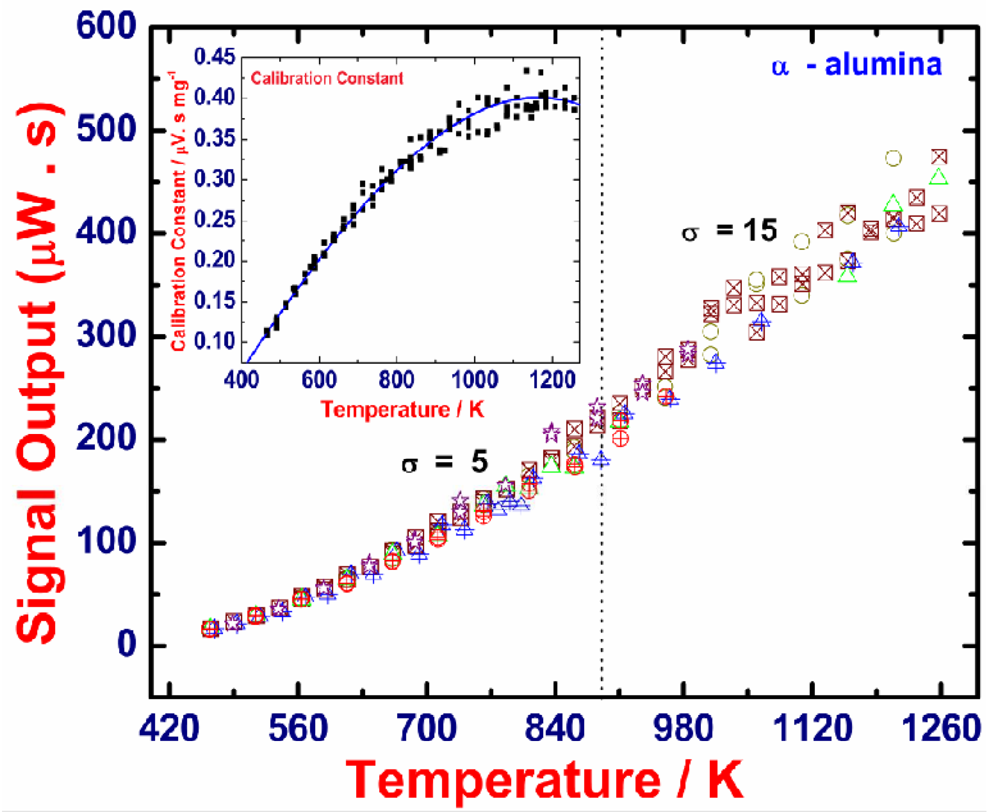

Fig. 2.5 Illustration of the temperature variation of Q for a typical experimental schedule and Calibration constant (inset)

2.4. Differential scanning calorimetry (DSC)

2.4.1 Principle of DSC

The principle of DSC is to compare the heat flow to the sample and to an inert reference material when both are heated or cooled at the same rate. Phase changes that are associated with heat absorption or evolution induce a commensurate change in the differential heat flow between sample and reference, which in effect appears as an uncompensated temperature differential ΔT, spread over the transformation event. Two types of DSC systems are commonly in use and that are power compensating type and heat flux type

In a power compensated DSC both sample and reference materials are heated by two separate identical furnaces at equal heating rate. Any change in the sample or reference temperature is being compensated by means of an electric power from external source to maintain the temperature difference (ΔT) between the sample and reference material either zero or constant. The compensating heating power is linearly proportional to the temperature difference ΔT between sample and reference. However, the use of this type of DSC at high temperature (above 700 ^{0}C (973 K)) is limited because the heat loss is more prominent at high temperature due to radiation.

In heat flux *DSC*, the test specimen *S* and reference material *R* (usually an empty sample pan + lid) are enclosed in the same furnace together with a metallic block of high thermal conductivity that ensures a good heat-flow path between *S* and *R*. Further, the enthalpy or heat capacity changes in the specimen S leads to a temperature difference between both *S* and *R* pans which results in a finite heat-flow between the sample and the reference. The temperature difference ΔT between *S* and *R* is recorded and further related to the enthalpy change in the specimen using calibration experiments. The heat-flux DSC system is thus a slightly modified DTA system with a good heat-flow path between the specimen and reference crucibles. The radiation loss at high temperature is same for both sample and reference materials and hence the heat flow between the sample and reference is not affected due to the radiation loss. The instrument used in the present investigation is a heat-flux type differential scanning calorimeter (*Setaram*® *Setsys 1600*), which is described below.

2.4.2. Equipment Details

Figure 2.6 depicts the heat flux DSC used in the present study (*Setaram*® *Setsys 1600*). The heat flux calorimeter consists of two pans, one for sample and the other for reference, which are connected by a low resistance heat flow path, with the thermocouple meant to sense the differential temperature positioned exactly beneath and midway connecting sample and reference. The accuracy of results obtained with DSC is slightly inferior at high temperature, notwithstanding the possibility of ensuring adequate experimental precaution [164]. The *Setaram*® *Setsys 1600* heat flux differential scanning calorimeter is basically a single structure integrated unit, wherein furnace, measurement head, mass flow controller, gas circuits and the controller are housed on a single mount. The control of equipment is made through the proprietary software that is interfaced with the equipment. The essential components of this DSC are as follows [165].

(i) High Temperature Furnace

The high temperature furnace shown in **Fig. 2.7(a)** is of cylindrical shape with a graphite tube heating element. An inert gas atmosphere is always maintained in the furnace chamber to avoid carbon evaporation at higher temperature. A thermocouple of B-type (PtRh 6%/30%) is placed in the analysis chamber and furnace chamber for respective temperature measurement.

(ii) Measurement Head – DSC Probe

The DSC – plate is called the measurement head which is displayed in **Fig. 2.7(b).** This is a machined metallic plate made of platinized copper-constantan containing two housings for the sample and reference crucible fitted to a narrow alumina rod. The sample and reference crucibles are made of recrystallized alumina having nearly identical mass of about 240–250 mg and a volume of about 100 μL. The metallic plate consists of an embedded thin wire of highly conductive platinum that serves the purpose of *heat resistor* between sample and the reference.

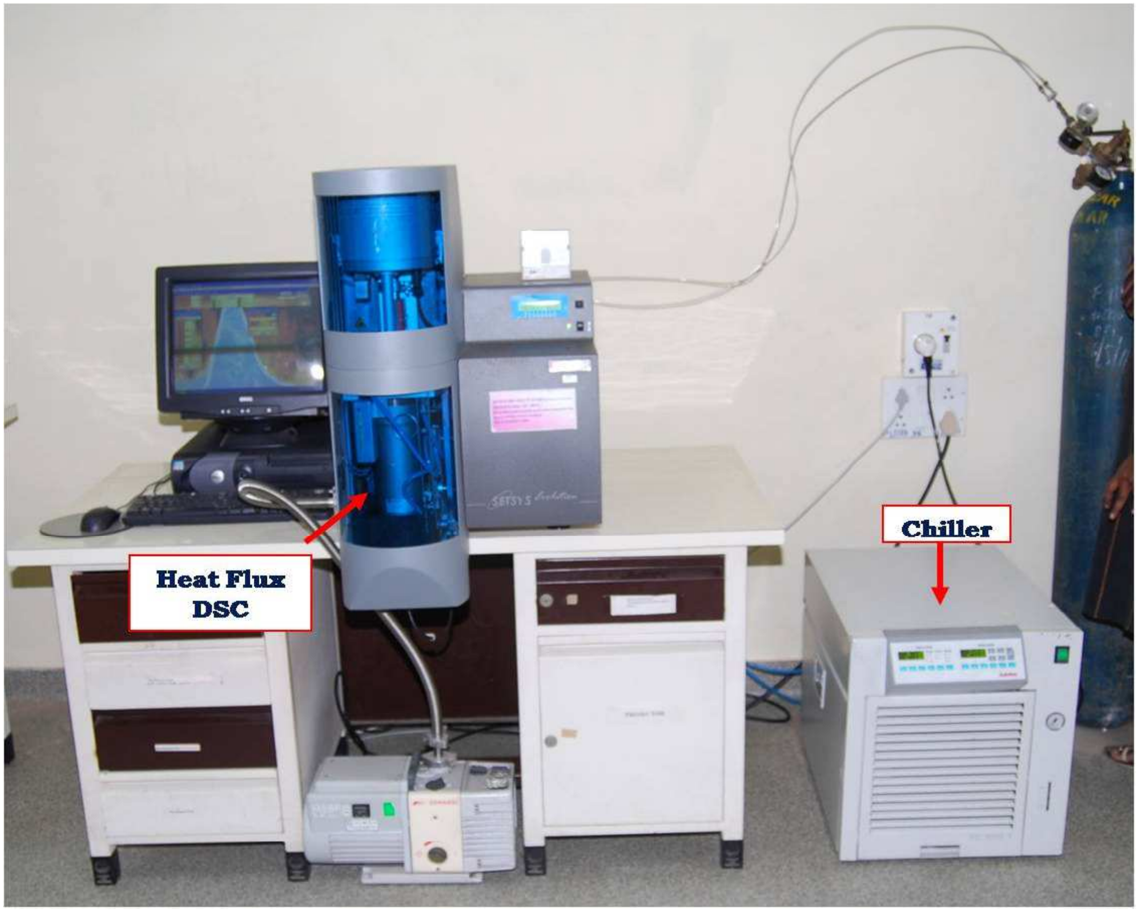

Fig.2.6 The experimental set up for heat flux DSC used in the present study

The differential thermocouple of B-type (PtRh 6%/PtRh 30%) is positioned exactly below the DSC plate and the gap between them is less than 2 mm. In addition, the central section of the DSC plate sensor contains a thermocouple of B- type that measures the sample temperature directly. The whole set up comprising of DSC plate, sample and reference crucibles, thermocouples, guiding alumina tube together make up the heat flux DSC probe which is hung from the top balancing plate. The DSC probe is always kept within the uniform temperature zone of the water cooled graphite furnace.

(iii) Vacuum Circuit, Gas Circuit, Chilled Water Cooling Circuit

A rotary vacuum pump serves the purpose of evacuating both analysis and furnace chamber. A separate chiller (*Julabo FC 1600 T*) for water circulation is connected to cool the graphite furnace. The vacuum and the water supply operations are done through an electro valve command option. The programming and temperature control of the furnace is done by the controller which is integrated with the CPU.

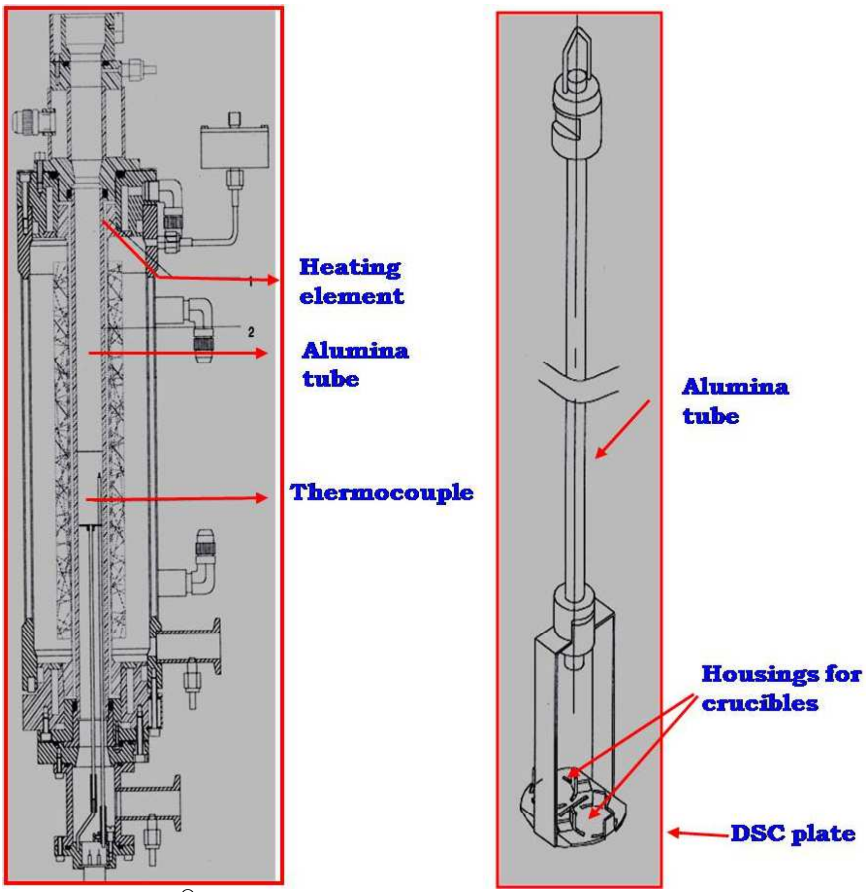

Fig.2.7 (a) *Setaram*® high temperature DSC furnace **(b)** Heat flux DSC plate-rod

2.4.3. Experimental Procedure

In the present study, samples of dimension $2\times 2\times 2\ mm$ of mass 80-100 mg were polished to obtain a flat surface to ensure better heat conduction., An empty cylindrical alumina crucible with a volume of 100 μL is taken as reference and another identical crucible is loaded with the sample. Before starting the experiment, the experimental chamber consisting of DSC probe and the furnace is evacuated and purged with pure argon gas with a flow rate of about 50 *ml* per minute. The flow rate is maintained by means of electronic mass flow controller (MFC) throughout the experiment. An argon pressure of about 1300 *mbar* is maintained in the graphite furnace chamber. In the first step of the experimental schedule, the furnace temperature is gradually raised to 473 K at a heating rate of 5 or 10 K min^{-1} and is allowed to stabilize at this temperature for about 15 minutes. This leads to a smooth baseline which ensures the attainment of thermal equilibrium of the system before starting any measurement, which is essential for quantitative DSC experiments. Following this step, suitable heating and cooling programmes are adopted. The heating and cooling rates adopted are in the range 1-99 K min^{-1}. Fresh samples are employed for each run and a few repeat runs are also carried out for select heating rates (10 and 100 K min^{-1}) in order to ensure the reproducibility at either end of the scan rate spectrum.

The measurement details of the transformation temperature, enthalpy of transformation as well as the estimation of kinetic parameters are described in the following section.

2.4.4. Temperature Calibration in DSC

The temperature calibration is carried out using the melting points of pure aluminum, zinc, tin, copper, silver, gold and iron standards [166]. The onset value T_S of the melting point is determined by the procedure given above. These onset temperatures are determined for various heating rates such as 1, 3, 5, 7, 10, 15, 20, 30 K min^{-1} and the resulting data are plotted in **Fig. 2.8.** In order to obtain the so-called equilibrium onset temperature, the plot in **Fig. 2.8** is extrapolated to hypothetical heating rate of 0 K min^{-1} [167-168].

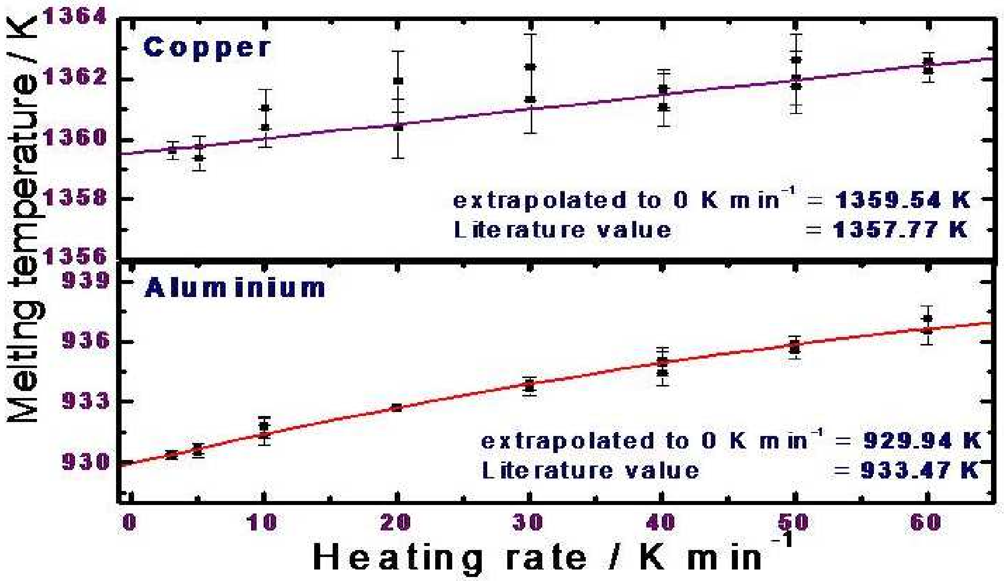

Fig. 2.8 Temperature calibration in DSC with pure Copper and Aluminum standards

These values are compared with the standard literature values in order to estimate the correction to be employed for obtaining the true transformation temperatures. The temperature accuracy in case of low heating rate experiments (1–30 K min^{-1}) is found to be ±2 K for samples of mass up to 50–100 mg; while it is ±4 K for high heating rates (>30 K min^{-1}). The extrapolated melting temperature of Cu and Al is compared with literature values and the deviation is found to be within ± 4 K. The degree of reproducibility is also checked with repeat runs and the error in temperature measurement is found to be ±1 K.

2.4.5 Measurement of phase transformation enthalpy

From a standard non-isothermal DSC scan exhibiting a peak due to distinct phase transformation; it is generally assumed that the heat of phase transformation is directly proportional to the peak area after suitable baseline normalization. Thus,

$$\Delta H_{tr} = k(T) \times (\text{Peak Area}) \qquad (2.5)$$

ΔH_{tr} is the enthalpy change accompanying phase transformation, $k(T)$ is the temperature dependent calibration constant. Peak area is the total area under the transformation peak which is readily obtained by the data processing software after appropriate baseline construction [168-171]. The conversion factor *k(T)* is obtained by measuring the peak area recorded with the melting reactions of standards like pure aluminum, zinc, tin, copper and iron etc. of known enthalpy [171]. In the case of metals it is a usual practice to estimate the calibration constants with small heating rates in order to avoid the effect of undercooling. In addition, it is also desirable to employ a calibrant that shares similar thermophysical characteristics with the alloy under investigation. In view of this, pure iron has been taken as the calibrant in the present study for characterizing accurately the enthalpy effects of steels.

It is important to mentionhere that, with the adaptation of proper calibration procedure, a DSC can also be effectively used to get estimates of specific heat [168-171]. However, in the present study, the specific heat has been estimated from the measured enthalpy increment using drop calorimeter which provides more reliable and accurate heat capacity as the measurements were carried out under near-equilibrium conditions.

2.5 Thermo mechanical Analyser

Thermo Mechanical Analyser (TMA) or Dilatometry is a thermo-analytical technique for measuring the linear thermal dilation (expansion/shrinkage) of a solid material that is subjected to a programmed heating/cooling. The dilation of a specimen with change in temperature is mechanically detected by a pushrod in contact with the sample and is transmitted to a sensor which records the variation of dimension as a function of temperature. In general the push rod dilatometers are mounted in two different designs, namely (i) horizontal and (ii) vertical push rod dilatometers. A horizontally mounted push rod dilatometer gives better temperature uniformity within the furnace although a small tracking force is always required for the push rod to ensure good contact between the sample and pushrod [163]. In contrast, components in a vertical dilatometer can remain in contact under their own weight, which may be at the expense of an inferior thermal gradient in the specimen due to furnace convection currents [163]. **Figure 2.9** portrays the schematic of a vertical push rod dilatometer.

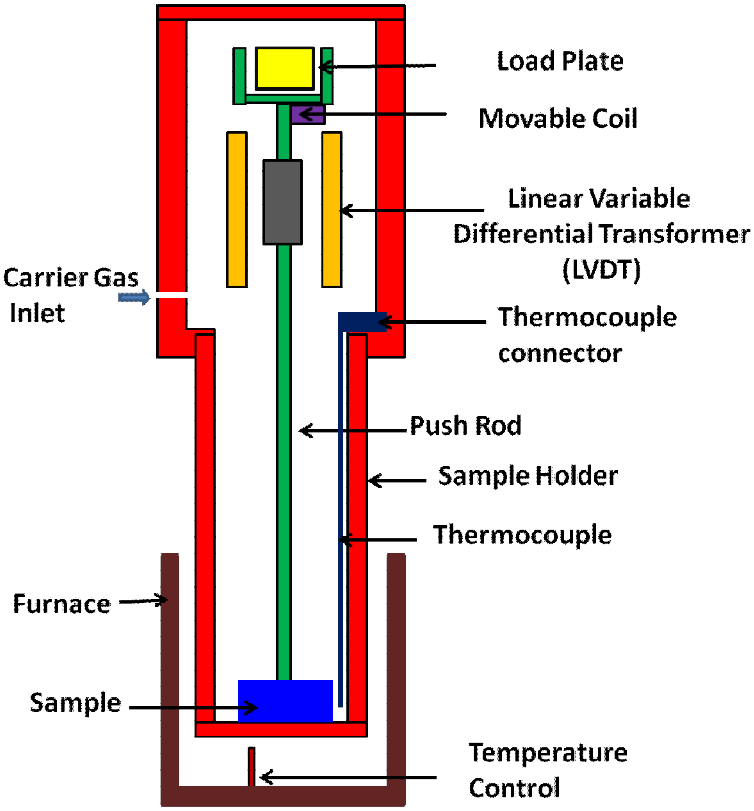

Fig. 2.9 Schematic representation of a vertical push rod dilatometer

The push rod is thermally stabilized and insensitive to mechanical vibration. The specimen is positioned just below the push rod inside the furnace. The linear variable differential transformer (LVDT) which is insulated from the furnace is mounted over the push rod which measures the dimensional change in the sample. The thermocouple is placed very close to the sample in order to measure the furnace temperature precisely. In the present investigation, the dilatational strain has been measured using *Setaram® Setsys evolution TMA 16* equipment. A brief description on the equipment is what follows in the next section.

2.5.1. Instrument details

Setaram® Setsys evolution TMA 16 is a vertically mounted single pushrod type dilatometer equipped with a resistance heated graphite furnace and an LVDT sensor for measuring the temperature induced linear dimensional strain (Δl / l_o) [172]. **Figure 2.10** depicts the experimental set up for the *Setaram® Setsys evolution TMA 16*.

(i) High temperature furnace

The high temperature furnace is made up of a graphite tube which serves the purpose of heating element that surrounds the experimental chamber. A type-B thermocouple (PtRh 6% / PtRh 30%) is fixed along the wall of the sample holder tube to measure the furnace temperature. The temperature controller is placed below the sample holder tube mounted on the bottom of the furnace wall.

(ii) Sample holder and push rod assembly

The sample holder and the push rod assembly consist of a flat-ended recrystallized (RC) alumina sample holder tube and a RC alumina push rod with a hemispherical end. A rectangular cut was made at the bottom end of the sample holder tube to hold an RCA alumina plate over which the sample is positioned. The top end of sample holder tube was fixed with an aluminum support, which is connected to LVDT protective shell for vertical movement of the holder tube. The push rod used is mounted exactly at the center of the sample holder tube, and transmits the dilation signal to LVDT through a connected plunger. The bottom end of the push rod rested on the RCA alumina plate. The push rod is enabled to move up and down from the software control. When the pushrod is moved up, the sample is placed over the RCA alumina plate. Once the sample is placed properly, the pushrod is allowed to move down to touch the sample. For vertical movement of the sample holder and push rod assembly, a motor-controlled lifting mechanism has been positioned on the top. Once the sample is loaded, the entire assembly along with the sample is brought inside the furnace using the motor controller.

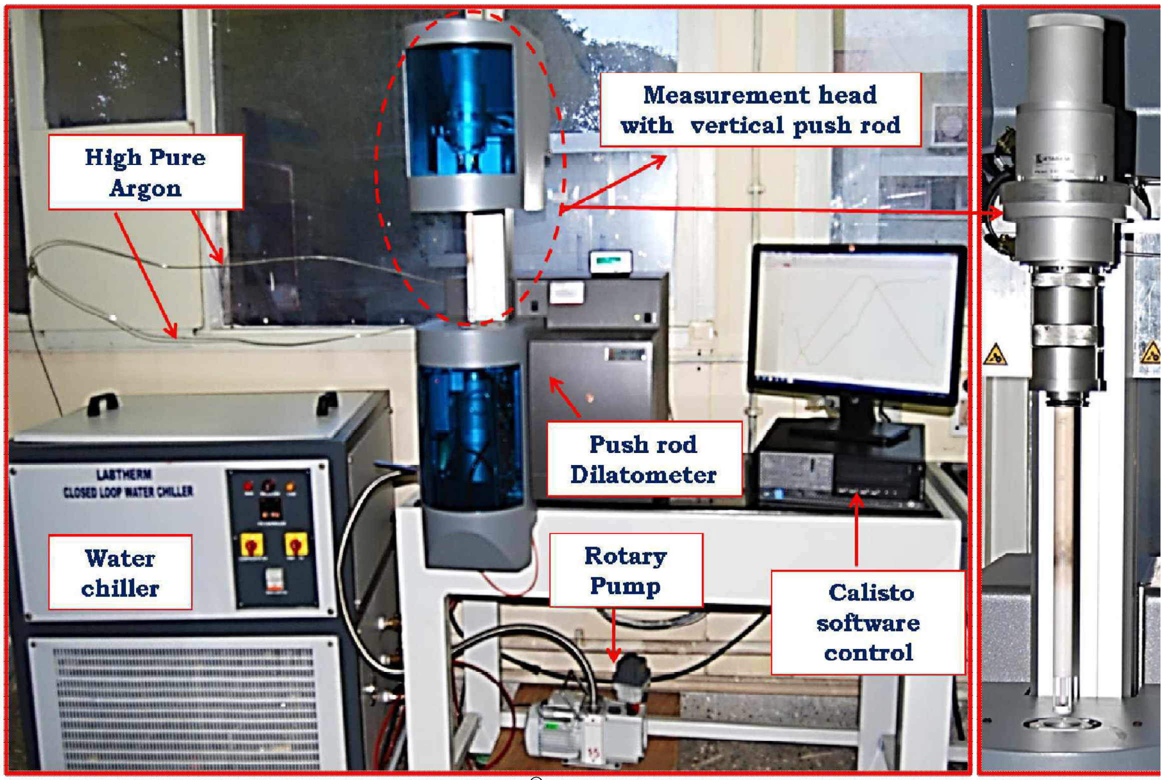

Fig. 2.10. Experimental set up for Setaram® setsys Evolution TMA 16

(iii) Linear variable differential Transformer (LVDT)

The LVDT is connected to the pushrod with a spring load configuration. The maximum range of displacement for the LVDT is ±2 mm. The lower range resolution of the LVDT is 0.23 μm. The output signal (analog) from the LVDT is directly fed to the data analysis software in order to obtain a temperature and time variation of dilatational strain in the measured specimen.

(iv) Gas, vacuum, chill-water circuit and controller

An external rotary vacuum pump (EDWARDS) supplied by *Setaram®* is used for evacuating both the experimental and furnace chambers before starting the experiment. After the pressure inside the experimental chamber reaches 1×10^{-2} mbar, both the chambers were filled with high pure argon gas to maintain atmospheric pressure. An external chill water supply with controlled flow is provided for the furnace cooling. The heating schedule programming, the data acquisition and storage are carried out through controller interfaced with the Calisto software through a personal computer.

2.5.2. Measurement details

Samples for dilatometry are taken in the form of small rectangular (20 x 20 mm) slices with smooth and flat surface. The starting thickness of the sample has been measured by a digital Vernier gauge with least count ±0.01 mm. The entire experiment has been carried out in flowing high purity Ar–gas atmosphere. Pure Sapphire supplied by *Setaram*® with known bulk thermal expansion values are used as calibration standard [173]. **Figure 2.11** portrays the measured dilation ($\Delta l/l$) observed for the sapphire standard supplied by *Setaram*® along with the reported values. The relative accuracy of the measured normalized dilatational strain in percentage ($\Delta l\ /\ l_{298}$) has been estimated to be 5%. The calibration of temperature has been carried by measuring the allotropic transition (α-bcc→γ-fcc) of high purity iron (Sigma Aldrich iron with 80 mass ppm of impurities) samples under slow heating (3 K min^{-1}) conditions. The temperature accuracy was found to be ±2 K. The recorded dilation in a push rod dilatometer for any specimen is the overall dilation due to the sample, the sample holder, as well as the push rod. In order to obtain the dilatational strain due to the sample alone, a baseline correction is essential [163, 174-175]. A brief account of the baseline correction method adopted in this study is presented here. For every experiment with the specimen, one blank run (without sample) has been carried out to monitor the dilatational strain due to the sample holder and push rod assembly.

The measured values of temperature dependent dilation (Δl) with the sample placed on the holder and without sample can be expressed by the following equations.

$$\Delta l_{sample}(T) = \Delta l_{sampleholder}(T) + \Delta l_{pushrod}(T) + \Delta l_{sample}(T) \tag{2.6}$$

$$\Delta l_{blank}(T) = \Delta l_{sample\ holder}(T) + \Delta l_{pushrod}(T) \tag{2.7}$$

For the blank run, the extra length of the pushrod introduced inside the furnace due to the absence of specimen needs to be considered.

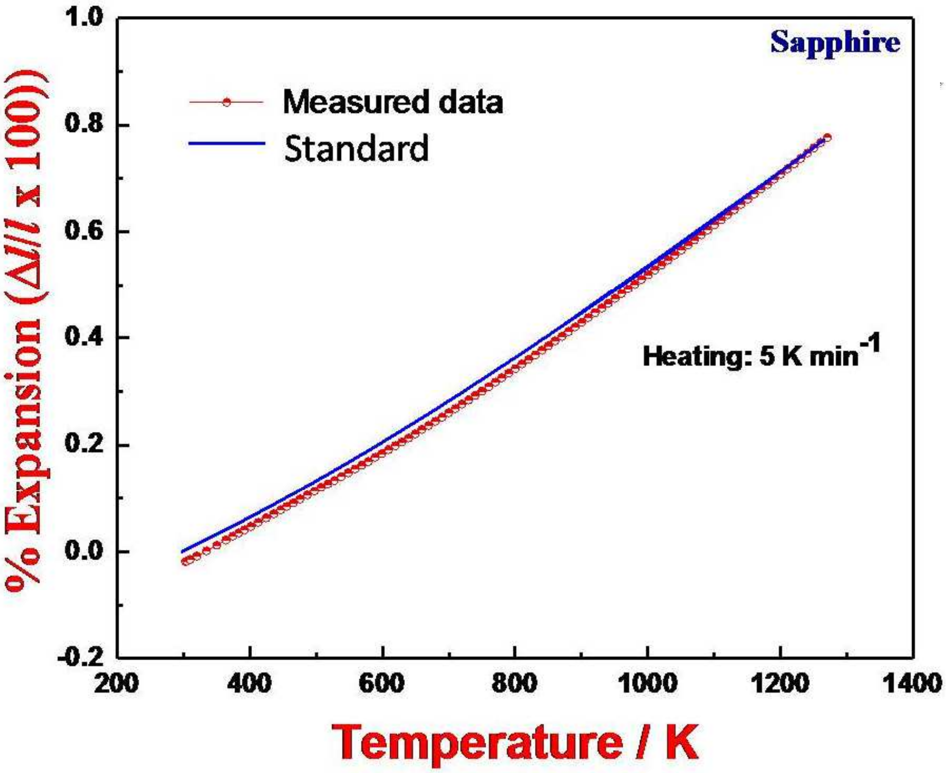

Fig. 2.11. Calibration of push rod dilatometer using sapphire standard

The extra contribution from the (specimen holder + pushrod) towards the dilatational strain in the blank run is an outcome of the extra length of the pushrod (equivalent to the length of the sample). If α_{sample} and $\alpha_{push\text{-}rod}$ are the thermal expansion coefficient of sample and the push rod respectively, then the dilatational strain is represented as

$$\Delta l_{sample} = \Delta l_{sampleholder}(T) + L_{sample} \times \alpha_{sample}(T) \tag{2.8}$$

$$\Delta l_{Blank} = \Delta l_{sampleholder}(T) + L_{pushrod} \times \alpha_{pushrod}(T) \tag{2.9}$$

In a similar manner the temperature dependent dilation can be obtained for a reference specimen with known thermal expansion. The dilation in the reference specimen can be represented as:

$$\Delta l_{reference} = \Delta l_{sample\ holder(T)} + L_{reference} \times \alpha_{reference} \tag{2.10}$$

Subtracting Eq. (2.9) from Eq. (2.10) and Eq. (2.10) from Eq. (2.8) gives

$$\alpha_{sample}(T) = \frac{\left(\Delta l_{sample} - \Delta l_{blank} + L_{pushrod} \times \alpha_{pushrod}(T)\right)}{L_{sample}} \tag{2.11}$$

$$\alpha_{pushrod}(T) = \frac{\left(L_{reference} \times \alpha_{reference}(T) - \Delta l_{reference} + \Delta l_{blank}\right)}{L_{pushrod}} \tag{2.12}$$

Once the $\alpha_{push\text{-}rod}(T)$ is evaluated from Eq. (2.12) using known value of $\alpha_{reference}$ the dilation due to specimen alone and its thermal expansion can be evaluated using Eq. (2.11).

2.6. Laser flash thermal diffusivity

The laser flash method is generally acknowledged as a standard and reliable method for measuring thermal diffusivities of solids above room temperature [176-177]. This is because the method employs non-contact, non-destructive temperature sensing to achieve high accuracy [178]. The basic principle of a laser flash thermal diffusivity is the measurement of the temperature rise of one surface of the specimen as a function of time when the other surface is irradiated with a programmed laser flash. The resulting measuring signal computes the thermal diffusivity. If the temperature dependence of density and specific heat (C_p) is known for the sample, the thermal conductivity of the sample is estimated from the measured thermal diffusivity values.

2.6.1. Instrumental details

In the present study the measurement of temperature dependent thermal diffusivities was carried out using a *Linseis*® laser flash apparatus (LFA). The experimental set up for the thermal diffusivity measurement carried out in this study is portrayed in **Fig. 2.12.** The major components of the LFA are described below:

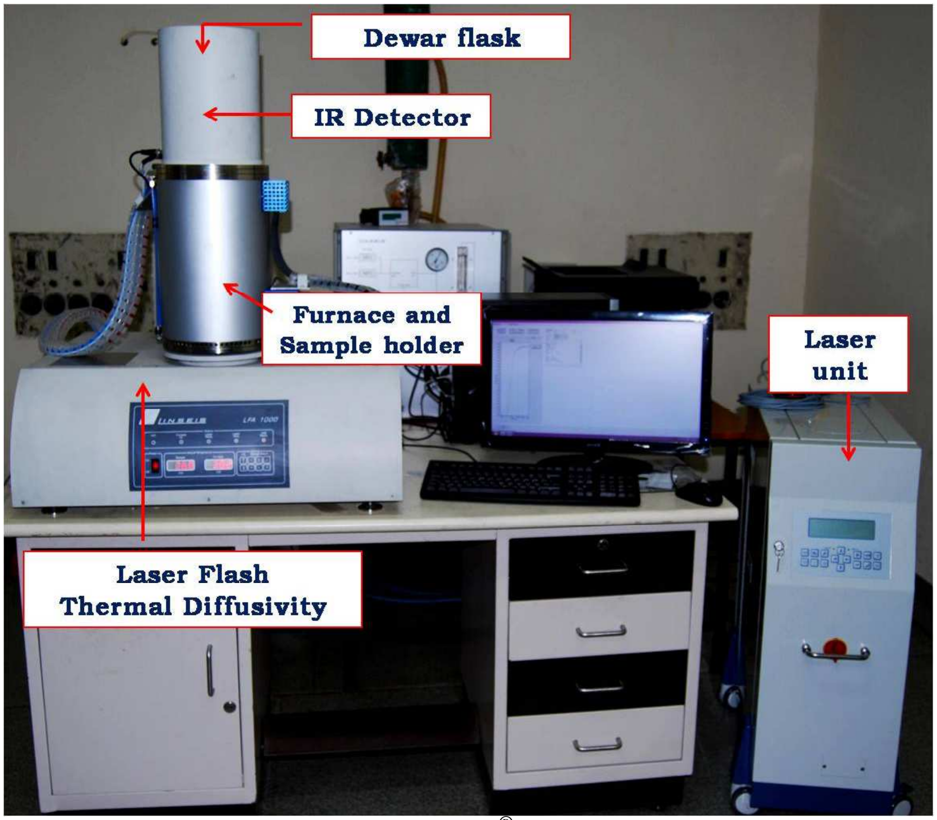

Fig. 2.12. Experimental set up for the Linseis® laser flash apparatus

(i) Laser source

The sample was irradiated with an Nd-YAG laser source with adjustable incident pulse energy and a pulse length of 300 μs. The maximum pulse energy of the laser source is 25 J per pulse. Both the power and the pulse length are easily adjustable d by the controlling software.

(ii) IR detector

The diffusivity system is equipped with one InSb infrared detector at the rear end of the sample. The transient thermal energy conducted through the thickness of the thin sample after the irradiation of laser flash is detected at the back surface of the flat sample by the rise in temperature (ΔT). The infrared detector is cooled with the help of liquid N_2 at regular intervals during an experimental schedule.

(iii) High temperature furnace

The high temperature SiC furnace is positioned inside the diffusivity set up. The maximum temperature achieved by the furnace is 1600 ^{0}C (1873 K). The heating rate can be varied from 2 K min^{-1} to 50 K min^{-1}, depending on the experimental conditions. In the present investigation an optimal heating rate of 7 K min^{-1} has been chosen for the measurement of thermal diffusivity.

(iv) Sample holder

A fully motorized sample robot is placed at the center of the furnace which can carry up to 6 samples. There are three sample slots for square shaped (side - 10 mm) as well as circular disc shaped specimens with the diameter of 25.4 mm. This design allows uninterrupted throughput. Liquid samples can also be measured in special containers.

(v) Gas, vacuum, chill-water circuit and controller

An external turbo molecular pump (10^{-5}mbar) attached to the furnace chamber is used for evacuating the furnace chamber. Further a manual or automatic software controlled gas control box (2, 3 or 4 gases) is also attached to generate specific gas atmospheres. The recorded data from the IR detector is analyzed through the LFA software provided by *Linseis* which evaluates the thermal diffusivity by the selection of appropriate conduction model which best fits the measured time variation of temperature data.

2.6.2. Measurement details

In order to ensure the maximum absorption of heat from the incident laser pulse, the sample was coated with a thin layer of graphite. It is noteworthy to mention here that, with increase in temperature, the absorptivity of laser is changed depending on the temperature dependence of electrical conductivity of the specimen. In case of stainless steels, the absorptivity increases as the electrical conductivity decreases with increase in temperature [179]. However, the absorptivity can be enhanced to a great extent using graphite coatings which gives the surfaces a near black body behavior [180-181]. In addition, the measurements of diffusivity are carried out under vacuum which eliminate the possibility of gaseous convection of heat from the specimen after it is exposed to the laser pulse. Under such situations, it is assumed that the incident laser energy is fully absorbed on the irradiated surface which ensures adiabatic conditions. As soon as the back surface of the specimen is irradiated with the laser flash, the transient thermal energy is conducted through the thickness of the thin sample in a short time interval. This is detected at the back surface of the flat sample by the rise in temperature (ΔT) through the infrared detector. The measured temperature rise as a function of time (t) is recorded by a suitable electronic data collection and analysis protocol. The observed ΔT versus t variation is fitted to a standard predefined one-dimensional conduction model through a thin metallic slab, which enables the precise estimation of the quantity $t_{1/2.}$ Physically $t_{1/2}$ represents the time required for the back surface to reach half of the maximum measured temperature rise ($\Delta T/2$). Then it emerges that the thermal diffusivity of the sample is given by the following expression [180-181].

$$\lambda = \frac{1.73\,\mathrm{L}^2}{\pi^2 t_{1/2}} \tag{2.13}$$

Where L is the thickness and λ is the thermal diffusivity of the sample. A minimum of five concordant measurements were carried out at 50 K temperature interval. The average of these five measurements was taken as typical thermal diffusivity estimate at the measurement temperature. The accuracy of each measurement is found to be ±3 %. In case of materials where the conduction is the mode of heat transmission, the flash method has been shown to have an maximum uncertainty of ±4% at elevated temperatures [181]. The accuracy in the temperature measurement is observed to be ± 2 K.

2.7. Microstructure characterization and hardness measurement

2.7.1. Optical metallography

Optical microscopy images were obtained using a *Leica MeF4A®* optical microscope fitted with a Leica digital camera and associated proprietary software for image acquisition and analysis. The specimen surfaces were prepared using established metallography procedures. Mounting of sample was done using cold setting resin (epoxy resin) and some samples through hot mounting press (thermosetting plastic – phenolic resin), which were then ground systematically from coarser to finer emery grades (wet silicon carbide paper) with rotating discs. Finally, the samples were polished with alumina and diamond paste and thoroughly cleaned. Etching was done by swabbing the surface with the appropriate etchant.

2.7.2 X-Ray Diffraction (XRD)

XRD analysis was carried out using an Inel XRG 3000 -X-Ray diffractometer which makes use of a curved position sensitive X-ray detector. Such type of detectors can measure up to 120 degrees of 2θ simultaneously and have high speed of data acquisition. Thin slices of specimen of dimensions 10 mm×10 mm and thickness of ~ 2 mm were flattened by grinding and loaded. The voltage and the current level in X-ray tube were set as 40 kV and 30 mA respectively. Cu-K_α source of wavelength 1.5406 Å with a nickel filter was used in the present study. The diffraction pattern for each sample was recorded for duration of 1 h. The diffractometer was calibrated with annealed silicon powder obtained from NPL, India. The recorded peak positions, full width at half maximum and *d*-spacings were compared with the standard values from JCPDS data.

2.7.3 Scanning Electron Microscopy (SEM)

Scanning electron microscopy studies were carried out with *Philips XL30 ESEM* attached with *Energy Dispersive Spectrometer* for microchemical analysis. The specimens were prepared in a similar manner to that for optical microscopy. Secondary electron modes are used for the microstructural observations. Conducting carbon tapes were used for grounding the charge to prevent the buildup of electrostatic charge. The magnification calibration was made with standard cross grating samples of 20 lines/mm and 2160 lines/mm. Resolution was calibrated with gold nanoparticles embedded on carbon film, whose spacing was of the order of 20 Å. Energy dispersive X-ray analysis was carried out for qualitative identification of elements with atomic number greater than 10.

2.7.4 Microhardness measurement

Vickers hardness measurements were carried out with *Leitz* Vickers micro hardness tester using loads of 50 or 100 *g* load. About eight to ten measurements was taken for each data point and the average value is reported. The probable error calculated by taking 15 indentation measurements on the standard sample was found to be within ±3 %. The Vickers hardness number (VHN) is calculated using the following formula

$$\mathrm{VHN}=1.854\times(F/D^2). \tag{2.14}$$

with F is the applied load and D^2 is the area of the indentation.

Chapter-3

Phase stability of Fe-16 at. % Cr alloy: A calorimetry and modelling based approach to elucidate the role of magnetic interactions

3.1. Introduction

Although the Fe-Cr alloys are well studied there is not enough literature on high temperature thermodynamic properties and its interpretation in terms of physical based modelling protocols, to yield a wholesome picture of phase stability in Fe-Cr system. Moreover, the thermal properties of the anomalous domain of Fe rich dilute Fe-Cr alloy has not been systematically studied under equilibrium condition as a function of temperature and composition, since the pioneering studies of Dench [25] and Normanton *et al.*[33]. This puts a constraint of not having adequate data to model the magnetic contribution to Gibbs energy, ΔG^{mag} [95-98]. Recent spin polarized density functional theory (DFT) calculations with disordered localized moment [65-78], have offered some insights into low temperature region of Fe-Cr equilibrium diagram. The DFT calculations suggest some revisions with respect to α'/α'+α"– *solvus* boundary and also on the skewed nature of α'+α" miscibility gap [85]. These changes are in tune with the findings of small angle neutron scattering experiments on iron rich Fe-Cr alloys [54-57]. In order to address the ambiguity on the solubility of Cr in α - Fe and the anomalous behavior of dilute Fe rich Fe-Cr alloy, it is essential to determine the equilibrium thermal properties at low and high temperatures. The present study aims to filling up this gap partially. In specific terms, equilibrium measurements of high temperature enthalpy increment (H_T-$H_{298.15}$) have been made on Fe-16 a*t* % Cr alloy using inverse drop calorimetry in the temperature range, 25 -1050 ^{0}C (298 to 1323 K). The Curie temperature and the transformation enthalpy associated with the magnetic transformation have been experimentally determined. Further, a consolidated physically based modelling approach has been developed which fully describes the thermodynamic properties of ferromagnetic α phase for Fe-rich Fe-Cr alloys (0-16 at. %Cr). Therefore, by generation of high temperature calorimetry data and possible integration of these in terms of simple and physically based modelling protocols, a wholesome conceptual basis of phase stability in Fe rich Fe-Cr system has been established.

3.2. Characterisation of Fe-16 a*t.* % Cr alloy

The room temperature XRD pattern of a slow cooled homogenized Fe-16 *at.* %Cr alloy is shown in **Fig. 3.1(a).** It reveals the presence of single α-bcc phase with a lattice parameter value, a_{α}= 0.2868 nm.

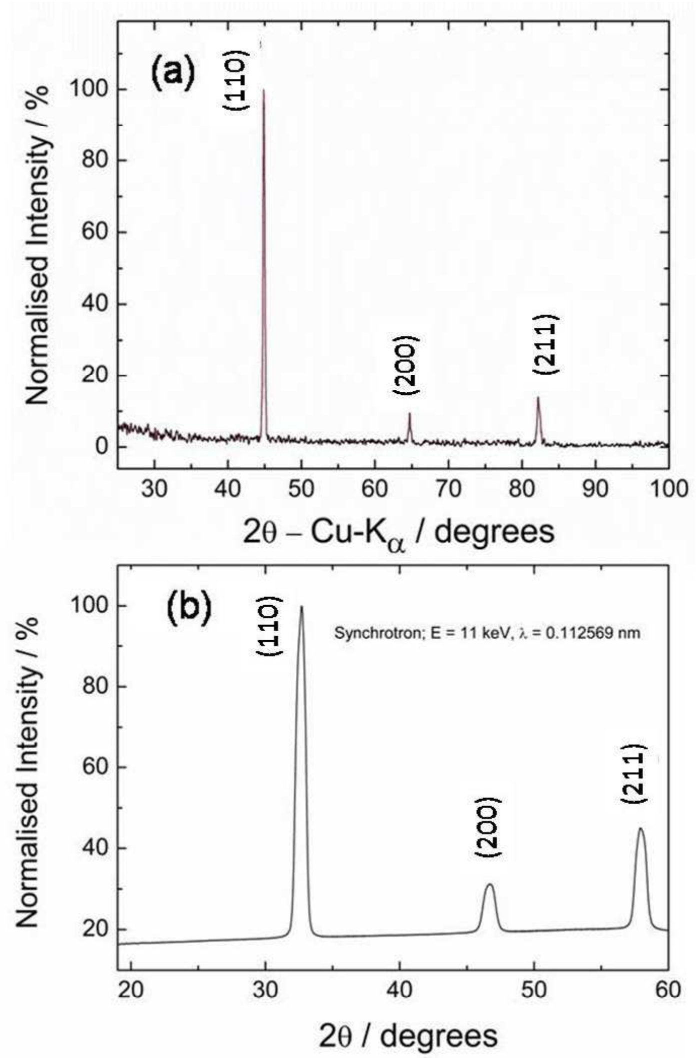

Fig. 3.1(*a*). Room Temperature X-ray diffraction pattern of homogenized Fe-16 a*t*.% Cr alloy and (***b***) diffraction pattern obtained using 11 keV synchrotron source.

In the widely accepted Fe-Cr equilibrium diagram [85], the Fe-16 *at.*% Cr alloy is reported as a two-phase mix of Fe-rich α' and Cr-rich α" phases at room temperature. However, the XRD profile in **Fig. 3.1(a)** shows no evidence for the presence of Cr-rich α"-bcc phase. In order to rule out the presence of low volume fraction of α"-phase, high resolution diffraction data has been obtained using 11 keV synchrotron source at Indus II, RRCAT Indore. The synchrotron based XRD pattern is shown in **Fig. 3.1(b)** where in no evidence is observed for Cr-rich α"-phase. Further, the lattice parameter of α-ferrite phase obtained from the principal reflections of both conventional XRD (0.2868 nm) and synchrotron source (0.2864 *nm*) are in good agreement. The microstructure of the alloy is shown in **Fig. 3.2** which reveals an equiaxed homogeneous grain structure.

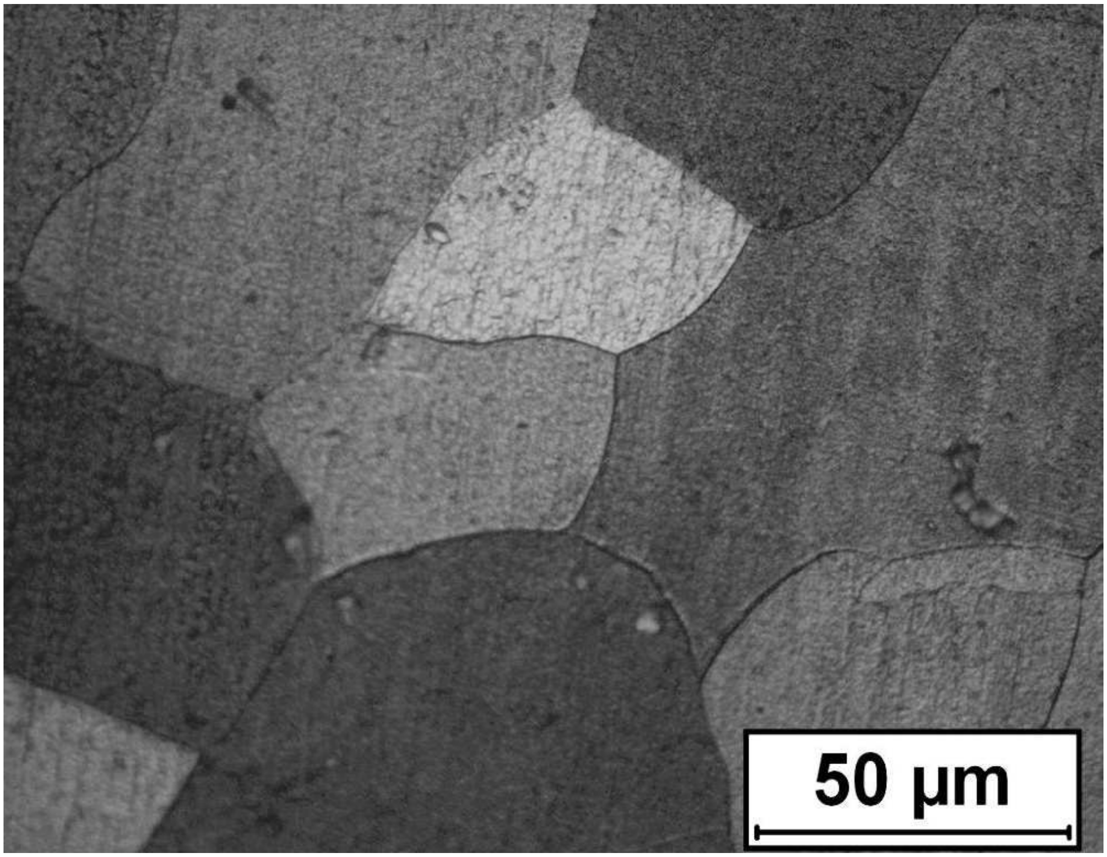

Fig. 3.2. Optical micrograph of homogenized Fe-16 a*t*.% Cr alloy

3.3. Evaluation of thermodynamic properties using calorimetry methods

The baseline calibrated DSC thermogram recorded at 10 K min^{-1} heating and cooling cycle is presented in **Fig. 3.3**. The figure shows two sharp thermal arrests at 711 ^{0}C (984 K) ± 5 ^{0}C and 1512 ^{0}C (1785 K) ±10 ^{0}C during the heating cycle. These correspond to magnetic transformation of $\alpha_{ferro}\rightarrow\alpha_{para}$ (T_c) and α-ferrite → Liquid transformations respectively. The measured transformation temperatures are in good agreement with the currently reported values for T_c and melting [40]. The temperature variation of measured enthalpy increment values, H_T-$H_{298.15}$/J mol^{-1} obtained by drop calorimetry is graphically shown in **Fig. 3.4**. The enthalpy data (circled in **Fig. 3.4**) exhibits a steady increase with temperature; and in the temperature domain associated with magnetic transition T_c, there is a marked change in slope, suggesting that $\alpha_{ferro}\rightarrow\alpha_{para}$ phase transition is accompanied by a continuous enthalpy change, ΔH_{mag}(T).

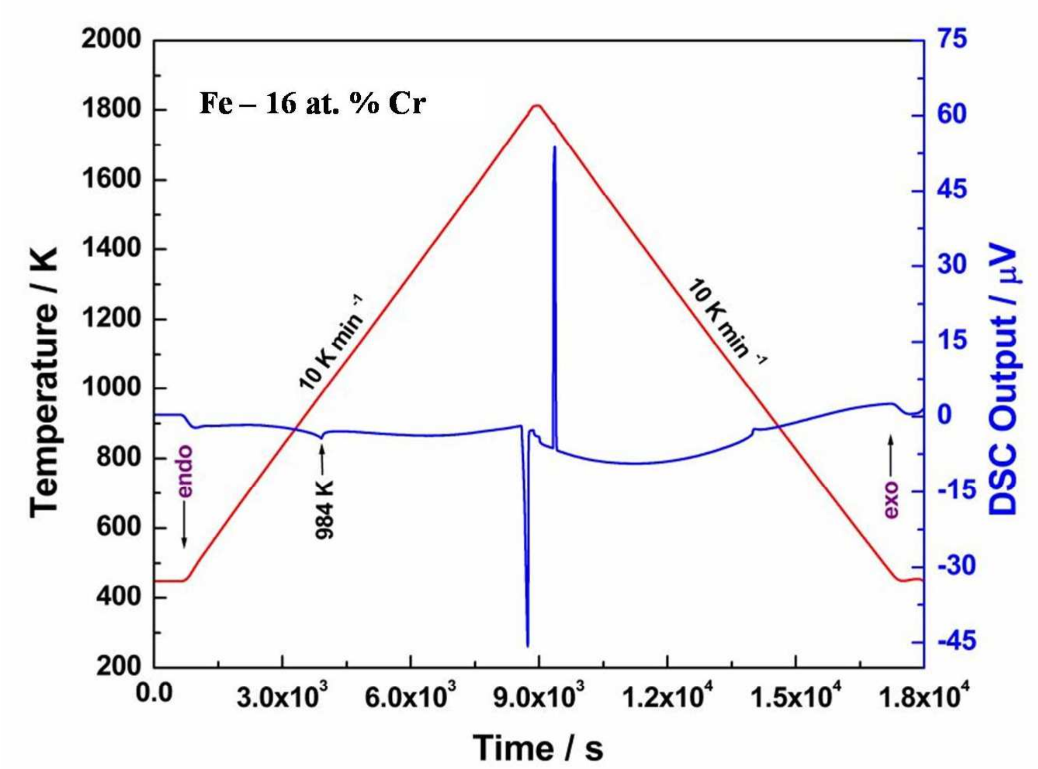

Fig. 3.3. Differential scanning calorimetry trace of annealed Fe-16 a*t*.% Cr alloy at 10 K min^{-1} heating and cooling rate.

In the present case, a value of about 2.2±0.2 kJmol^{-1} for the magnetic transformation enthalpy ΔH_{mag}, has been estimated for Fe-16 a*t*. % Cr alloy. The method of evaluating ΔH_{mag} from experimentally measured temperature dependent enthalpy increment values has already been detailed in Chapter 2. The value estimated in this study is lower than 7.32 kJ mol^{-1}, the value reported for Fe-16 at.% Cr alloy, by Normanton *et al* [33]. However, the T_c measured in this study compares very well with the interpolated estimate of Normantan *et al*.[33]. This difference could probably be due to H_{700} being used as a reference enthalpy value by Normantan *et al*. in place of $H_{298.15}$ used conventionally.

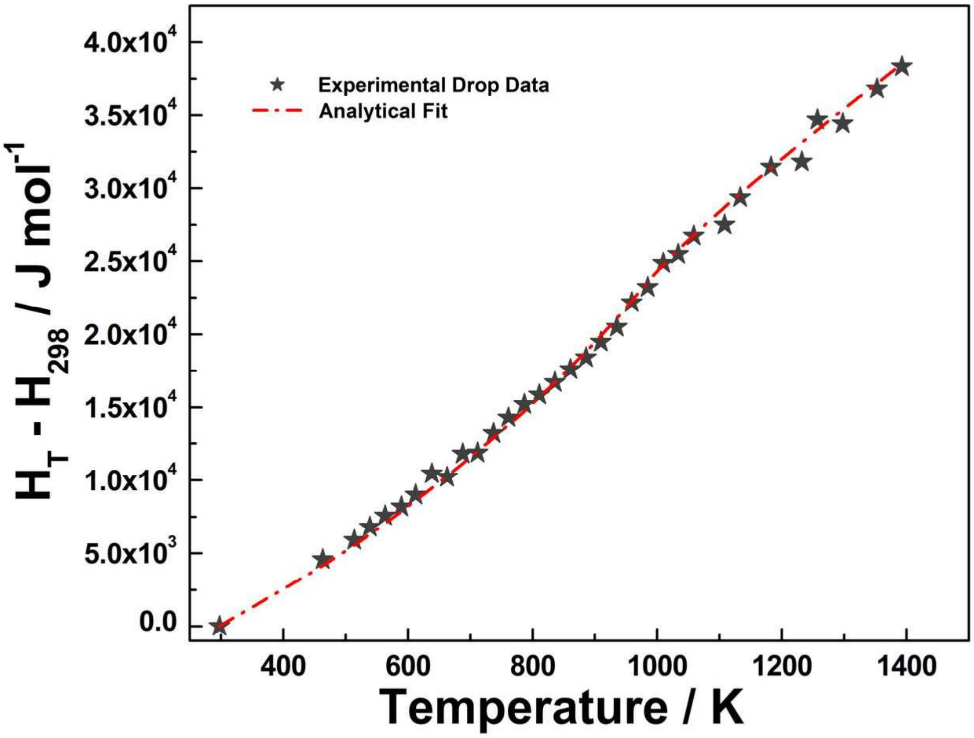

Fig. 3.4. Temperature variation of experimentally measured enthalpy increment H_T-$H_{298.15}$ values plotted along with the fit data

Study of available literature shows a wide variation in the reported ΔH_{mag} values in Fe-Cr alloys. A comparison with zero Kelvin spin-polarized DFT estimate of Ruban *et al*.[75], for $\Delta^{o}E_{mag}$ indicates that the present experimental value of ΔH_{mag} is lower than the theoretical one by a factor 3 [87]. However, it is known that the theoretical ΔE_{mag} pertains to the difference in total calculated total (cohesive) energies between a ferromagnetic ground state and hypothetical paramagnetic one at zero Kelvin. The ferromagnetic ground state energy is calculated for the equilibrium value of the total average magnetic moment $<M_o>$ estimated at corresponding equilibrium atomic volume, V_o. On the other hand, the experimental ΔH_{mag} corresponds to the change in enthalpy associated with $\alpha_{ferro} \rightarrow \alpha_{para}$ transition measured at T_c= 711 ^{0}C (984±5 K). It is well known that at finite temperatures, $0 \leq T \leq T_c$, the measured value of saturation magnetic moment $<M>$ is less than its value at zero Kelvin, $<M_o>$. In fact, for itinerant ferromagnetic alloys, it is generally found that $M(T) \cong M_o(1-T/T_c)^{\beta}$; with β=0.32-0.36 [95]. In view of this fact, it is evident that ΔE_{mag} would be a strongly decreasing function of temperature, and further at temperatures close to T_c, it is only expected to be a small fraction of its maximum value at zero Kelvin. It is necessary to emphasize here while comparing experimental and theoretical estimates of thermodynamic quantities, that different theoretical values for M_o, V_o and ΔE_{mag} would be obtained depending on the level of technical sophistication and calculation methodologies adopted for treating the magnetic part of total binding energy. Thus, for example, the disordered localized moment-ferromagnetic-local spin density approximation (DLM-FM-LSDA) based calculations of Ruban *et al.* [75], yield for $\Delta^o E_{mag}$ a value of 15.1 kJ mol^{-1}(11.5 mRy/at); while the calculations by same authors in DLM-FM-GGA (generalized gradient approximation) return a higher estimate of 17.06 kJ mol^{-1} (13.0 mRy/at) [74, 87]. In comparison, the Calphad estimate is placed somewhat lower at 9.2 kJ mol^{-1} (7 mRy/at) [40]. Interestingly, another earlier theoretical calculation by Klaver *et al.*, [66] on Fe-Cr system gives ΔE_{mag} values, which are lower than the latter theoretical estimates of Ruban *et al* [75, 87]. It is also interesting to recall that there is about 10% difference between various computed ground state magnetic moment $<M_o>$ values [78, 98], which might partly account for the above difference in computed estimates of ΔE_{mag}. In addition, it must also be mentioned that the experimental estimate of ΔH_{mag} is subjected to ± 10% error. In view of the above discussions, the present experimental estimate of ΔH_{mag} =

2.2±0.2 $kJmol^{-1}$ for Fe-15Cr alloy is considered to be well within the accepted uncertainty bounds. This is also consistent with the observed decrease in the average magnetic moment <M> with increasing Cr-concentration in Fe-Cr system [40, 66, 78, 87, 98]

3.4. Analytical data fitting procedure

The measured H_T-$H_{298.15}$ variation with temperature (T) has been fitted to the following empirical form.

$$H_T-H_{298.15} = A+ BT+ CT^2 +D/T + \Delta H_{mag} \tag{3.1}$$

The first four terms on the right-hand side of *Eq.* (3.1) belong to the classical Maier-Kelley empirical formulation for representing the temperature dependence of heat capacity $C_p(T)$ of paramagnetic solids in the high temperature region ($T \geq \theta_D$). Since Fe-15Cr alloy is ferromagnetic, the magnetic contribution to H_T-$H_{298.15}$ is treated separately as an additive contribution, using the phenomenological Hillert-Jarl model [97], which requires only the knowledge of T_c and β, the average total magnetic moment as a function of alloy composition. Thus, $\Delta H_{mag}(T)$ may be given as,

$$\Delta H_{mag}(T)= RT\, ln(\beta+1)\times h(\tau) \tag{3.2}$$

Where, R is the gas constant, $h(\tau)$ is a function of scaled temperature, $\tau = T/T_c$ and is given as,

$$h(\tau)=\{(-79\tau^{-1}/140\ p) + (474/497)\times(1/p-1)[(\tau^3/2)+(\tau^9/15)+(\tau^{15}/40)]\}/D;\ \text{for } \tau\leq 1. \tag{3.3}$$

$$h(\tau)=\{(\tau^{-5}/2)+(\tau^{-15}/21)+(\tau^{-25}/60)\}/D;\ \text{for } \tau>1. \tag{3.4}$$

In the above expression, D is an empirical constant given by the expression

$$D = (518/1125) + (11692/15975)(1/p-1) \tag{3.5}$$

The parameter, p is the fraction of magnetic enthalpy absorbed above T_c and is normally dependent on structure [96, 97]. It takes the value, $p = 0.40$; and D = 1.55828482 for bcc or B2 ordered structure; while, $p = 0.28$ and D = 2.342456517 otherwise [183]. The corresponding expression for magnetic contribution to specific heat $\Delta C_p^{mag}(T)$ is given as follows.

$$\Delta C_p^{mag}(T) = R\, ln(\beta+1)\times C(\tau) \qquad (3.6)$$

$$C(\tau) = \{(474/497)*(1/p-1)[(2\tau^3)+(2\tau^9/3)+(2\tau^{15}/5)]\}/D;\ \text{for } \tau\leq 1 \qquad (3.7)$$

$$C(\tau) =\{(2\tau^{-5})+(2\tau^{-15}/3)+(2\tau^{-25}/3)\}/D;\ \text{for } \tau >1 \qquad (3.8)$$

In a similar way, the magnetic contribution to entropy $\Delta S_{mag}(T)$, is given by the following set of expressions.

$$\Delta S_{mag}(T) = -R ln(\beta+1)\times f(\tau) \qquad (3.9)$$

$$f(\tau) = 1-\{(474/497)\times(1/p-1)\times[(2\tau^3/3)+(2\tau^9/27)+(2\tau^{15}/75)\}/D;\ \text{for } \tau\leq 1 \qquad (3.10)$$

$$f(\tau) = \{(2\tau^{-5}/5)+(2\tau^{-15}/45)+(2\tau^{-25}/125)\}/D;\ \text{for } \tau >1 \qquad (3.11)$$

For Fe-15Cr alloy, there are no experimental estimates of saturation magnetic moment β. In view of this, the theoretical estimate of $\beta = 1.75$, coming from spin-polarised DFT calculations is adopted in this study [65, 85, 87]. For T_c, the present experimental estimate of 984±5K is used.

The fitting of measured enthalpy increment data to Eq. (3.1-3.5) by means of nonlinear regression yielded the following set of values for the fit-coefficients. In the temperature range, $298.15\leq T\leq 1323$ K.

$$A\ /J\ mol^{-1} = -12656.62 \pm 352.1;$$

$$B\ /J\ mol^{-1}\ K^{-1} = 31.04 \pm 3.15;$$

$$C/J\ mol^{-1}\ K^{-2} = 0.00012 \pm 0.0003;$$

$$D/J\ K\ mol^{-1} = 1018574.08 \pm 9752.6;$$

$$\text{With, } R^2\ (\text{fit}) = 0.98 \qquad (3.12)$$

The experimental enthalpy increment data together with the above described analytical fit (line joining the experimental data points) have been co-plotted in **Fig. 3.4** and they are in good agreement. The total heat capacity C_p that is consistent with the above fit is given as,

$$C_p = B+2CT-D/T^2+\Delta C_p^{mag} \qquad (3.13)$$

In the above expression, ΔC_p^{mag}, the magnetic contribution to C_p is given Eq. (3.6-3.8). It is clear that the first three terms in the above expression stand for paramagnetic C_p. The magnetic part, ΔC_p^{mag} at $T_c = 711\ ^0C$ (984 K) is estimated to be 23.3 J mol^{-1} K^{-1}. At present, there are no reported experimental calorimetry estimates of this quantity for Fe-15Cr alloy. Nevertheless, the present value is in good agreement with the estimated value of 21 J mol^{-1} K^{-1} for an alloy of close composition namely Fe-13 *at.%* Cr for which the reported value of T_c is higher by about 23 K [40]. The experimentally estimated total C_p and ΔC_p^{mag} values are plotted as a function of temperature for Fe-16 a*t.* %Cr alloy in **Fig. 3.5**. This figure also contains experimental data on Fe-13Cr alloy, taken from the recent work of Xiong *et al* [40]. The experimental values of H_T-$H_{298.15}$, C_p, ΔC_p^{mag} values tabulated for Fe-16 *at.* % Cr alloy in **Table 3.1** are given for select temperatures. For comparison, the fit values of H_T-$H_{298.15}$ data have also been included.

3.5. Modelling of thermodynamic parameters of Fe-Cr alloys using Debye-Grüneisen formalism

It is well-known that thermodynamic properties of condensed phases can be computed either on *ab initio* basis or through suitable phenomenological equation of state (EoS), if reliable input data are available on EoS parameters [183-184]. In the present study, the Debye-Grüneisen formalism is adopted for computing the vibrational contribution to the thermodynamics of Fe-Cr alloys [183]. The temperature or in effect, the volume dependence of Debye characteristic temperature θ_D is taken care of by Grüneisen parameter γ_G. The vibrational contribution to enthalpy is also taken into account by the small conduction electronic contribution to heat capacity ΔC_p^{el}. Finally, as described in the previous section, the magnetic contribution is separately accounted for by the Hillert-Jarl model [97].

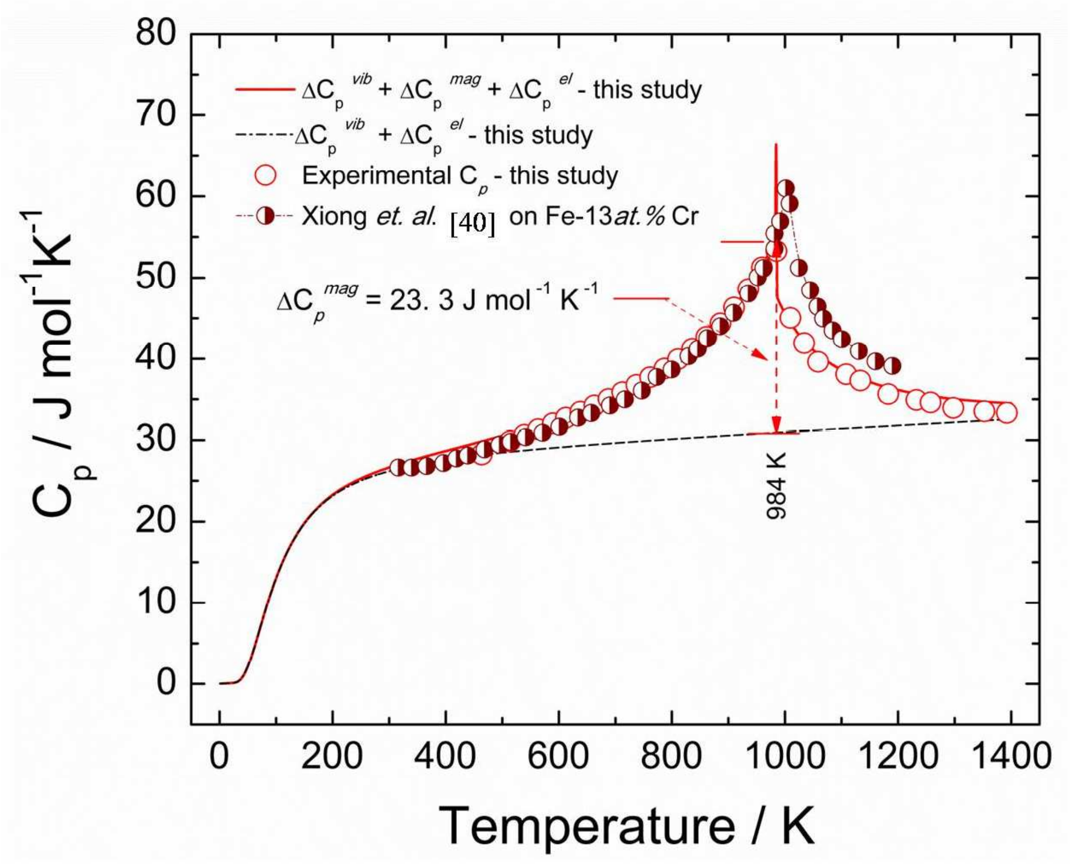

Fig. 3.5. Specific heat computed by Debye-Grüneisen model are plotted together with experimentally estimated values. For comparison, the experimentally determined values of C_p for Fe-13 *at.%* Cr alloy are also presented [40].

The total enthalpy H(T) at any pressure and temperature may be written as a sum of following partial contributions [183]:

$$H_T = E_o(V) + (\Delta E_{vib} + \Delta E_{el} + \Delta E_{mag} + \Delta E_{others}) + P\Delta V \qquad (3.14)$$

The first term, $E_o(V)$ stands for the Zero Kelvin contribution which is dependent on only volume. This is also called the potential or cold pressure term, as it is independent of temperature. To this zero Kelvin energy term, are added the thermal or vibrational contribution ΔE_{vib}, electronic contribution ΔE_{el} and other corrections coming from lattice defects and higher order contributions to anharmonicity, collectively given as ΔE_{others}.

Table 3.1

Tabulation of experimentally measured enthalpy increment (H_T-$H_{298.15}$) values together with corresponding fitted ones for select temperatures. The percentage deviation (δ) of fit enthalpy values from experimental data, the total specific heat C_p and its magnetic contribution ΔC_p^{mag} are listed

Temperature (K)	H_T–$H_{298.15}$ (J mol^{-1}) Experiment	H_T–$H_{298.15}$ (J mol^{-1}) Fit values	H_T–$H_{298.15}$ (J mol^{-1}) Model Estimated	$\delta=100\times(\Delta H_{Exp} - \Delta H_{Fit})/\Delta H_{Exp}$ (%)	C_p Expt. (J $mol^{-1}K^{-1}$)	ΔC_p^{mag} (J $mol^{-1}K^{-1}$)
Ferromagnetic α-Phase						
464	4574	4118	4394	9.98	28.23	1.5
514	5908	5560	5808	5.88	29.86	2.2
539	6819	6323	6559	7.27	30.65	2.6
563	7581	7063	7263	6.84	31.34	3.0
590	8195	7883	8038	3.81	32.06	3.4
613	8996	8622	8735	4.16	32.74	3.9
638	10446	9464	9537	9.40	33.48	4.4
663	10219	10279	10291	-0.59	34.23	5.0
712	11877	11996	11911	-1.00	35.87	6.3
737	13199	12897	12749	2.29	36.77	7.1
761	14298	13790	13573	3.55	37.73	7.9
787	15218	14747	14454	3.10	38.78	8.8
811	15859	15686	15323	1.09	39.94	9.9
836	16717	16702	16295	0.08	41.25	11.1
861	17603	17728	17224	-0.70	42.71	12.5
886	18401	18808	18228	-2.18	44.39	14.1
910	19476	19901	19276	-2.18	46.33	15.9
935	20480	21088	20375	-2.96	48.60	18.1
959	22183	22274	21487	-0.41	51.27	20.7
984	23230	23597	22717	-1.58	53.30	23.4
Paramagnetic α-Phase						
1010	24847	24761	25723	0.35	45.06	14.4
1034	25476	25791	26767	-1.24	41.95	11.3
1058	26730	26794	27808	-0.24	39.61	8.9
1108	27483	28713	29902	-4.48	38.08	7.2
1133	29363	29632	30974	-0.92	37.30	6.4
1183	31455	31406	32941	0.16	35.63	4.7
1232	31823	33136	34734	-4.13	34.92	3.9
1257	34696	33991	35774	2.03	34.61	3.6
1298	34436	35366	36691	-2.70	33.94	2.8
1353	36796	37186	38440	-1.06	33.52	2.3
1392	38326	38522	40170	-0.51	33.34	2.1

*Uncertainty associated with experimental temperature measurement is ± 2 K; the measured temperature stability as a function of time is better than ±0.01 K. Enthalpy increment H_T–$H_{298.15}$ values are accurate to ± 2% upto 700 K and ± 5%, upto 1400 K.

The PΔV is the thermal expansion correction for any chosen temperature T, and pressure P.

Of these, $E_o(V)$ is the baseline contribution, and being temperature independent does not contribute to C_v. It basically serves to define volume at zero Kelvin temperature V_o, since, the potential or cold pressure, is given as $P_c=-dE_o(V)/dV$. At thermodynamic equilibrium, this so-called internal pressure is fully balanced by the pressure offered by thermal and other contributions [184]. In normal practice, the quasiharmonic thermal contribution ΔE_{vib} may be satisfactorily approximated by either, Einstein, Debye or Nernst-Lindemann models, by incorporating a volume dependent characteristic temperature θ through appropriate mode averaged or bulk Gruneisen parameter γ_G [183-184]. In the present study, the Nernst-Lindemann interpolation scheme is followed for $\Delta E_{vib}(T)$.

$$\Delta E_{vib}(T)= (3/4)\, n\, R\, \theta\, [\{2/(e^{\theta/T}-1)\}+\{1/(e^{\theta/2T}-1)\}] \quad (3.15)$$

Θ is the characteristic temperature, can also be treated as a fit parameter and *n* is the number of molecules in one formula unit of substance under consideration. In the present case, $n=1$. The volume variation of θ is given as,

$$\gamma_G = -d\ln\theta/d\ln V \quad (3.16)$$

Or,

$$\theta(V) = \theta o(V/Vo)^{-\gamma G} \quad (3.17)$$

Neglecting the mode dependence of the Grüneisen parameters, the bulk thermal γ_G can be expressed as

$$\gamma_G = \alpha_v B_T V/C_v \quad (3.18)$$

Where, α_V is the volume thermal expansion coefficient, B_T is the isothermal bulk modulus and C_V is specific heat at constant volume. Alternately, where experimental data on α_v and C_v at 298 K are lacking for certain compositions, one may also use the following approximation correlating γ_G with Poisson ratio, σ [185].

$$\gamma_G = 3/2\{(1+\sigma)/(2-3\sigma)\} \quad (3.19)$$

$$1+\sigma = E/2G \quad (3.20)$$

$$1-2\sigma=E/3B \tag{3.21}$$

In the above expressions, E, G and B represent Young's, shear and bulk modulus values respectively. Finally, when reliable information on isothermal pressure-volume equation of state parameters is available through *ab initio* calculations, it is possible to estimate γ_G at zero Kelvin from the knowledge of pressure derivative of isothermal bulk modulus B'_T. Thus, using Slater's approximation, γ_G may be given as,

$$\gamma_G = \tfrac{1}{2}B'_T - 1/6 \tag{3.22}$$

The γ_G values estimated by different approximations exhibit minor differences. In the present study, Eq. (3.18) is employed to estimate γ_G, where reliable experimental thermophysical property data are available; otherwise, Eq. (3.19) is uniformly employed using the theoretical computed σ values for all Fe-Cr alloys in the range, 0-20 *wt.%* Cr. The electronic contribution to internal energy ΔE_{el}, is written as [183]

$$\Delta E_{el}/\text{atom} = (2\pi^2 k_B^2\, N(E_F)/3)(T^2/2) \tag{3.23}$$

$N(E_F)$ is the electron density of states/atom at the Fermi level, k_B is Boltzmann constant. The corresponding expression for ΔC_p^{el} is given by the following relation.

$$\Delta C_p^{el} = \Gamma_{el}\, T \tag{3.24}$$

$$\Gamma_{el} = 2\pi^2 k_B^2 N(E_F)/3 \tag{3.25}$$

It needs to be mentioned that wherever reliable experimental values for $N(E_F)$ and its composition dependence are available , these values are preferred. In **Table 3.2**, the input data for the model parameters are listed. It is necessary to state that for $x_{Cr} \leq 13$ at. %, the Fe-Cr alloys undergo α-ferrite→γ-austenite transformation at high temperatures. Calorimetry based studies in the γ-phase of Fe-Cr system is scarce, other than that of Normanton *et al* [33], which is even more limited in case of theoretical studies. Consistent set of theoretical estimates of molar volume, bulk modulus, Grüneisen parameter, Debye temperature, Poisson ratio, saturation magnetic moment, electronic density of states at Fermi level *etc*., are not available for *fcc* Fe-Cr alloys In view of this situation, the modelling approach could not be extended for γ-*fcc* Fe-Cr alloys. There is a need to reinvestigate the thermodynamics of *fcc* Fe-Cr alloys, through a combination of key experiments and theory. In addition to estimating total enthalpy or heat capacity as a function of temperature and composition, the Debye-Grüneisen formalism can also be successfully employed to arrive at a consistent estimate of volume thermal expansion [183]. The following expression is used for representing the temperature variation of molar volume, arising purely from the vibrational contribution.

$$V_T = V_0\{[E_{vib}/(Q_0 - k\,E_{vib})]+1\} \tag{3.26}$$

Where, $Q_o = B_T V_o/\gamma_G$ and $k = (B'_T - 1)/2$, V_o is the molar volume at reference temperature T_o = 298.15 K, B_T is isothermal bulk modulus and B'_T is the corresponding pressure derivative at 298.15 K. In case of magnetic alloys, the above expression needs to be further augmented with magnetic contributions to molar volume, ΔV_{mag} again as a function of temperature and Cr content. Although, the scope of this study is mainly restricted to calorimetric elucidation of high temperature phase stability, it is nevertheless useful to mention that accurate thermal expansion measurements can also be employed to unravel the role of magnetic interactions in Fe-Cr alloys. In **Fig. 3.5**, a comparison is made between the estimated contributions to specific heat C_p, as obtained by above mentioned modelling route and experimental values. A reasonably good agreement is seen. Interestingly a similar degree of match is also found between the model based estimated enthalpy increment values and the experimental data of Normanton *et. al.,* (H_T-H_{700}) for a variety of compositions [33]. This is illustrated in the collage given in **Fig. 3.6,** for few compositions, including pure iron. Since Normanton's work reports values only for temperatures exceeding 700 K, the predicted values could not be tested for their relative accuracy at lower temperatures.

Table 3.2

List of input parameters used in the Debye-Grüneisen+Hillert-Jarl model based estimation of vibrational and magnetic contributions to enthalpy and specific heat.

Alloy Designation (*at.%* Cr)	Fe	Fe-3Cr	Fe-9Cr	Fe-12Cr	Fe-16Cr	Fe-21Cr
Lattice parameter at 298K / *nm* [186]	0.2866	0.2867	0.2870	0.2870	0.2871	0.2872
Molar Volume /10^{-6} m^3 [186]	7.08	7.1	7.117	7.125	7.126	7.132
B_T /(GPa) [72]	193.9	180.6	180.4	183.8	186.7	192.7
Θ_D /*K* [72]	427	427	441	445	449	454
Poisson ratio (σ) [72]	0.291	0.278	0.263	0.262	0.262	0.265
γ_G (Eq. 3.19)	1.71	1.64	1.56	1.55	1.7	1.68
$N(E_f)$/eV. states [65]	1.04	0.956	0.831	0.859	0.91	0.97
Γ_e / J mol K^{-2} [65]	0.00497 (0.0049)	0.00461 (0.00452)	0.00426 (0.00393)	0.00396 (0.00406)	0.00377 (0.0043)	0.004125 (0.00458)
Average Magnetic moment (μB) [85]	2.224	2.147	1.99	1.91	1.82	1.75
T_c/K [40]	1043	1049	1027	1007	977 984 (this study)	929 925

However, it is interesting to note that simple quasiharmonic Debye-Grüneisen formalism in combination with Hillert-Jarl description of magnetic contribution, can quantitatively account for the measured variation of enthalpy with temperature to a good degree of accuracy.

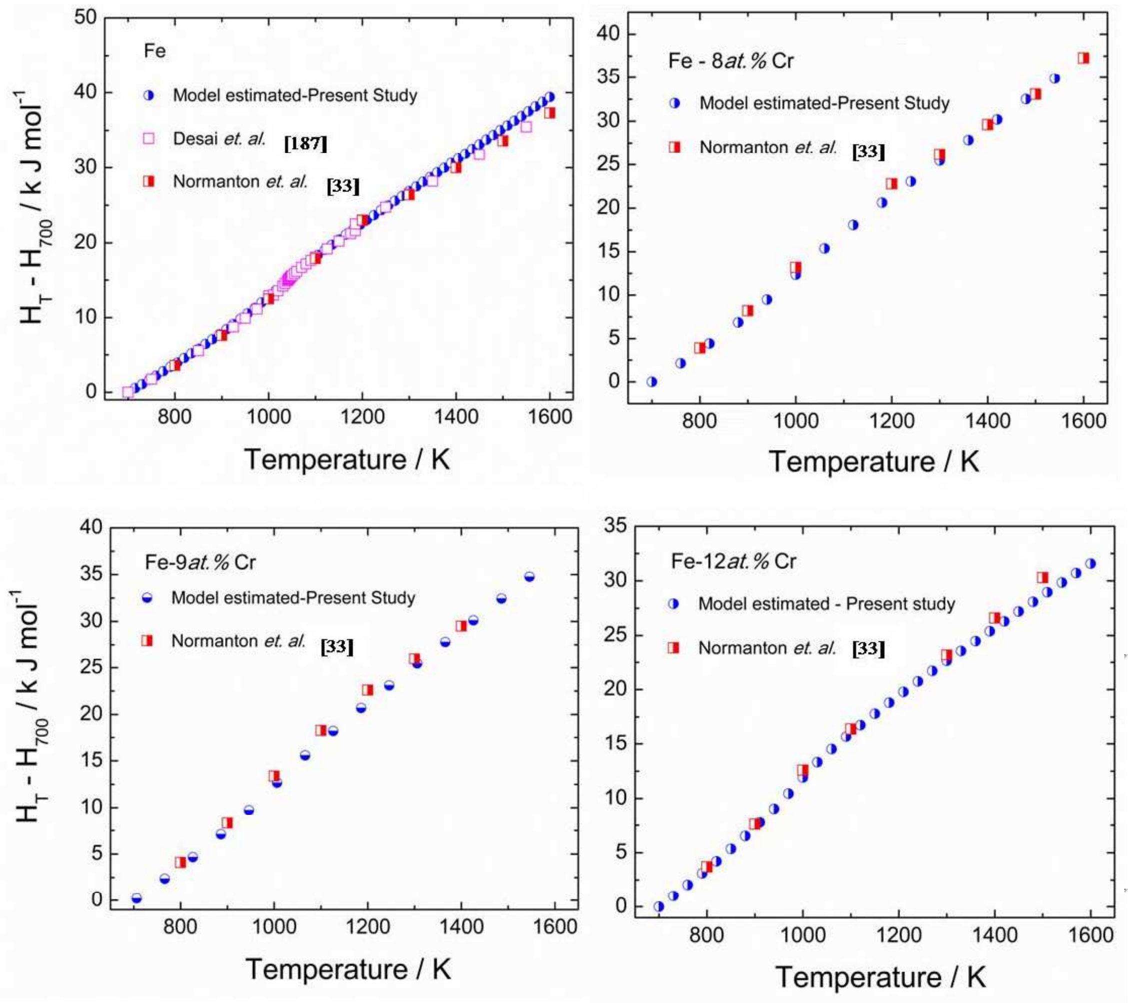

Fig.3.6. Comparison of experimental and estimated H_T-H_{700} values for Fe-0, 8, 9 and 12 *at.%* Cr alloys. For iron, the experimental data are taken from Desai [187], while for Fe-Cr alloys, the corresponding data are from Normanton [33].

Is is very useful to carry out fresh measurements on low temperature heat capacity and thermal expansion in Fe rich Fe-Cr alloy, so that the composite data could provide a clear description of the role of magnetic contribution to phase stability and thermophysical properties. In **Table 3.3**, the model-based predictions of ΔH^{mag}, ΔC_p^{mag}, and total C_p, inclusive of all major contributions, are listed along with experimental values wherever available, for a few select Fe-Cr compositions.

Table 3.3

Comparison of model based estimated ΔH^{mag}, C_p and ΔC_p^{mag} values for select compositions, with experimental data, wherever available.

at.% Cr	T_c (K)	ΔH^{mag} (kJ mol^{-1})	C_p *at* T_c (J mol^{-1} K^{-1})	$\Delta C_p^{\ mag}$ (J mol^{-1} K^{-1})
Fe-0Cr	1043	3.601	82.84	43.39
Fe-3Cr	1049	3.432	81.10	42.33
Fe-9Cr	1027	3.112	77.06	40.22
Fe-12Cr	1007	2.469	74.39	38.68
Fe-16Cr (This study; -expt.)	984	2.647 (2.2)	68.73 (56)	37.65 (23.4)
Fe-21Cr	925	2.857	70.51	35.40

Notwithstanding the limitations that are intrinsic to the model and uncertainty associated with the theoretical input used in this estimation, a reasonably good degree of agreement is observed. It is only for higher Cr content, where there is an acute shortage of magnetization data, the predictions are somewhat poor. Certainly, more remains to be done to fill the gap. The modelling framework adopted here is simple and besides, is designed to make full use of the available theoretical results of rigorous first principles calculations. accepted that a rigorous calculation of the thermodynamic properties of Fe-Cr alloys is difficult owing to the simultaneous and interacting presence of chemical [187] and magnetic short-range order in this system [84]. Therefore, the availability of any new and key experimental input is added advantage in fine tuning the theoretical assessment of Fe-Cr binary system, which is addressed to some extent in the present study.

3.6 Conclusions

Fe-16 a*t*.% Cr alloy in its equilibrium state is reported to be in the miscibility gap region in Fe–Cr phase diagram and exist as a two-phase mixture of Fe rich α'+ Cr rich α" phases. However, no evidence for phase separation was observed in this study due to kinetic factors in achieving *true* equilibrium. This could be due to sluggish diffusivity of Cr in Fe matrix below 600 ^{0}C (873 K).

- Enthalpy increment data measured under near equilibrium conditions have been modelled to obtain quantitative information on the magnetic contribution to enthalpy and entropy of phase transformation. The magnetic phase transformation, $\alpha_{ferro} \rightarrow \alpha_{para}$ is found to take place at 711 ± 5 ^{0}C (984 K). The enthalpy associated with this transformation is found to be 2.2 ± 0.2 kJ mol^{-1}.
- The temperature variation of enthalpy for Fe rich Fe-Cr alloys has been estimated from fundamental contributions arising from lattice vibration, magnetism and conduction electron contributions. Although the proposed model gives a good quantitative estimate of enthalpy data, in good agreement with experimental data, the anharmonic contribution needs to be taken into account for a better agreement at high temperatures

Chapter – 4

Influence of phase separation on thermal properties in Fe-21 at. %Cr binary system

4.1. Introduction

Phase equilibrium in Fe-Cr alloys has been a subject of intense research over several decades and there has been diversity in the assessment of the phase diagram especially around the miscibility gap region on Fe rich side. This is largely due to the difficulty in theoretically incorporating the combined effect of magnetic and chemical contributions to phase stability, particularly its dependence on composition and temperature, in the absence of reliable experimental data [85]. Owing to the emerging importance of high Cr ferritic and ferritic-martensitic steels in nuclear fission and fusion reactor applications [5-7], the Fe-Cr binary system has elicited significant attention from nuclear materials community. The attractive combination of physical, mechanical and nuclear properties of high Cr-ferritic-martensitic steels [6] has triggered a great deal of interest in understanding the defect dynamics in model Fe-Cr alloys [79, 83]. Further, owing to the importance of the α'+α'', decomposition reaction in influencing the long-term microstructural characteristics of technologically important Fe-Cr based ODS alloys, extensive characterization studies on the effect of thermal aging has been carried out using a spectrum of sophisticated experimental techniques, such as analytical electron microscopy, three dimensional atom probe tomography [40, 85, 131], and small angle neutron scattering (SANS) [54-57]. In particular, mention must be made of the recent investigations of Capdevila and coworkers [84] in highlighting the importance of time and temperature dependent thermal aging of highly metastable and supersaturated high temperature α (bcc) phase in the α'+α'', miscibility gap, in governing the evolution of nanoscale microstructural features and their eventual bearing on mechanical properties. Hence, it is necessary to possess an in-depth understanding of the thermo-kinetic aspects of α'+α'', decomposition reactions in Fe-Cr binary itself as a first step towards the knowledge driven design of high Cr ferritic and ODS alloys mainly those with Cr contents > 12 weight percent for demanding nuclear and other power plant applications. In view of the above a systematic study has been carried out on the high temperature phase stability and its effect on thermal properties in model Fe-21 at.% Cr alloy, the results of which will be described in the subsequent sections.

4.2. Characterization of Fe - 21 at.% Cr alloy

The room temperature X-ray diffraction profile of the Fe-21 at. % Cr alloy solution annealed at 1150 ^{0}C (1423 K) for 5 h followed by slow cooling are shown in **Fig. 4.1 (a-d)**.

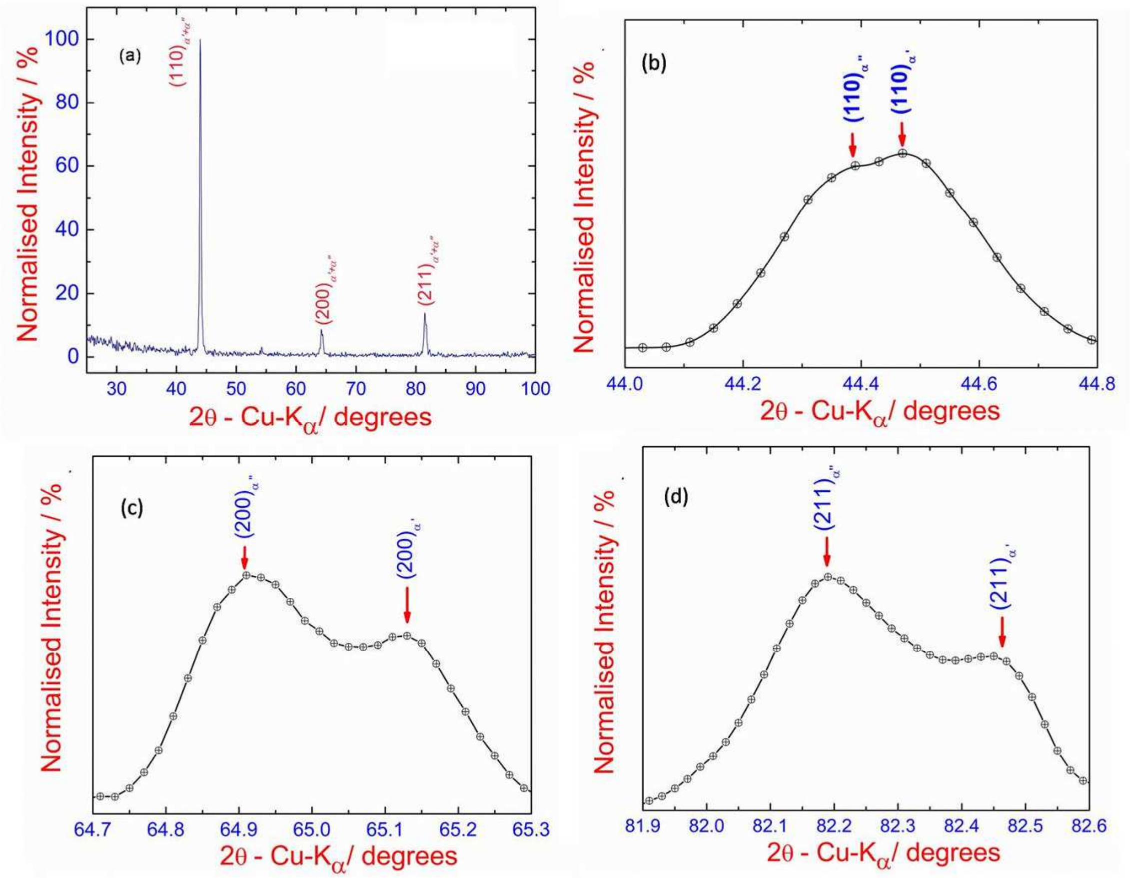

Fig. 4.1 (*a*) Room temperature X-ray diffraction pattern of homogenized Fe - 21 at.% Cr alloy. The split-nature of (110), (200) and (211) bcc peak profiles are clearly marked in (b), (c) and (d) respectively.

Analysis of the pattern in **Fig. 4.1(a)** shows weak signatures for the presence of bcc α' and α" phases. Since the difference in lattice parameter is small between α' (0.2852 nm) and α" (0.2864 nm) phases, the splitting of bcc diffraction peaks is rather minute and not readily observed in the XRD profile in **Fig. 4.1(a)**. However, in the expanded views of (110), (200), and (211) peak profiles shown in **Fig. 4.1(b)**, 4.**1(c)** and 4.**1(d)** respectively, the split nature of peaks provides evidence for the two phase α’+α” structure.

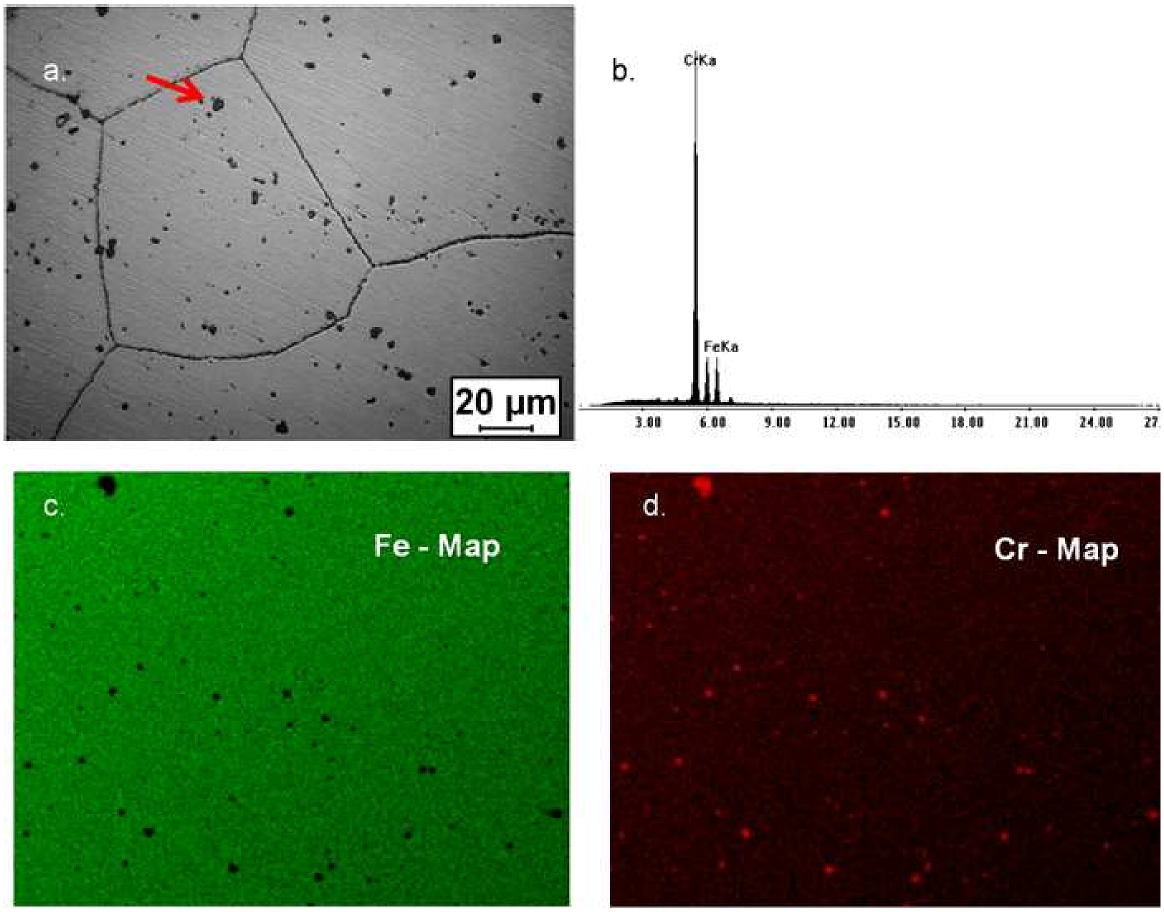

Fig. 4.2 **(a)** Microstructure of Fe-21 at.% Cr alloy, **(b)** EDX spectra of marked phase shows relative enrichment of Cr. The pseudo coloured X-ray maps obtained with (c) Fe-K_{α} and (d) Cr-K_{α} lines attest to the two-phase nature of alloy

The micrograph of the annealed alloy is shown in **Fig. 4.2(a).** The presence of α” in the form of embedded precipitates (arrow marked) in the α’ matrix is clearly observed. The EDX spectra as well as the pseudo colored X-ray elemental maps shown in **Fig. 4.2(b), 4.2(c) and 4.2(d)** respectively clearly establish the enrichment of Fe and Cr in α’ and α” phases respectively. In order to establish the characteristics of the α’ and α” phases in the actual calorimetry sample, an ion milled thin foil specimen of a drop calorimetry sample taken from the two-phase zone (~550 ^{0}C (823 K)) was examined by transmission electron microscopy (TEM). A typical TEM micrograph of alloy is shown in **Fig. 4.3**.

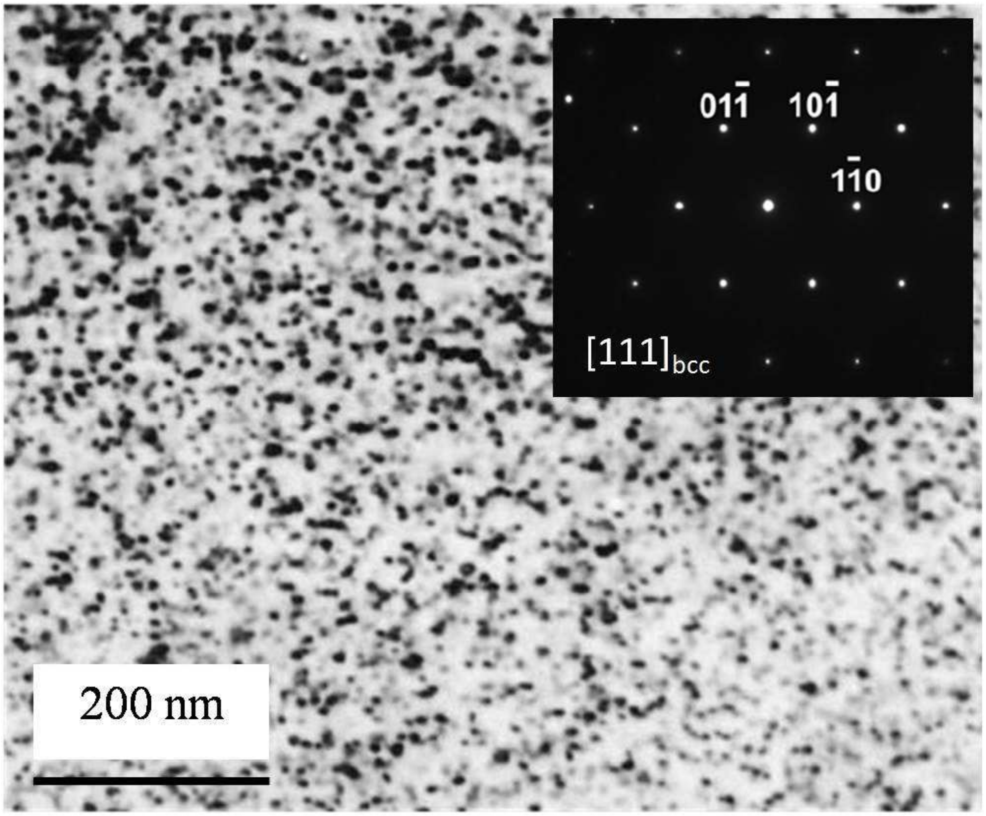

Fig.4.3 Transmission electron micrograph showing the α'+α" two phase structure, The SAD pattern in the inset shows $[111]_{bcc}$.

The presence of α" (Cr rich bcc) phase is seen as dark slightly elongated particles dispersed in the α' matrix phase which forms the matrix continuum. Since the lattice parameters of α'(bcc) and α"(bcc) phases are rather close, the selected area diffraction (SAD) pattern did not provide any additional information. It appears that slow cooling of the specimen in α'+α" two phase zone, coupled to the fact that during an actual isothermal measurement, the alloy does spend some additional time for decomposition to proceed, make it certain that measured enthalpy data actually pertain to α'+α" two phase structure. However, it is instructive to note that true thermodynamic equilibrium has not yet been realized in this study. In the present study, no further attempt has been made to characterize the microstructure in any detail, as it is primarily oriented towards investigating the thermodynamic aspects of phase transformation using calorimetry.

4.3 Enthalpy variation with temperature

The temperature variation of measured enthalpy increment (H_T-$H_{298.15}$) obtained by drop calorimetry measurements is graphically portrayed in **Fig. 4.4(a)**. **Figure 4.4(b)** shows an expanded view of the data in the temperature range of 327-827 ^{0}C (600-1100 K). The continuous line marked as #3 in **Fig. 4.4(a)** serves to identify the observed variation of measured enthalpy with temperature. As seen clearly in **Fig. 4.4(b),** starting from room temperature, the enthalpy of α'+α" two phase microstructure increases with temperature up to about 447 ^{0}C (720 ± 10 K). At this temperature a clear kink or inflection in an otherwise monotonically increasing feature is observed. At about 652 ^{0}C (925 ± 10 K), the enthalpy variation suffers another significant change in the slope (**Fig. 4.4 (b)**). In the intervening region, that is $720 \leq T \leq 925$ K, the enthalpy increase is fairly steady, although at about 597 ^{0}C (870 K) a cusp like feature is observed. Thus, going by these general characteristics of the enthalpy curve, and recognizing the fact that a discontinuous change in the temperature variation of enthalpy that is, ($\partial \Delta H/\partial T$) actually marks the incidence of a phase transformation in thermodynamic sense, these inflections or discontinuities in enthalpy versus temperature curve can be correlated with distinct phase changes in Fe - 21 at. % Cr alloy. At this stage, further interpretation of the enthalpy data requires the knowledge of Fe-Cr equilibrium diagram. Although the real nature of Fe-Cr phase diagram, especially in the vicinity of α → α'+α" miscibility gap is rather controversial, a particular version of α'+α" two phase region that is reported in one of the recent assessments [85] is reproduced in **Fig. 4.5** For comparison, **Fig. 4.5** also incorporates few other experimental and theoretical results on α/α'+α" boundary.

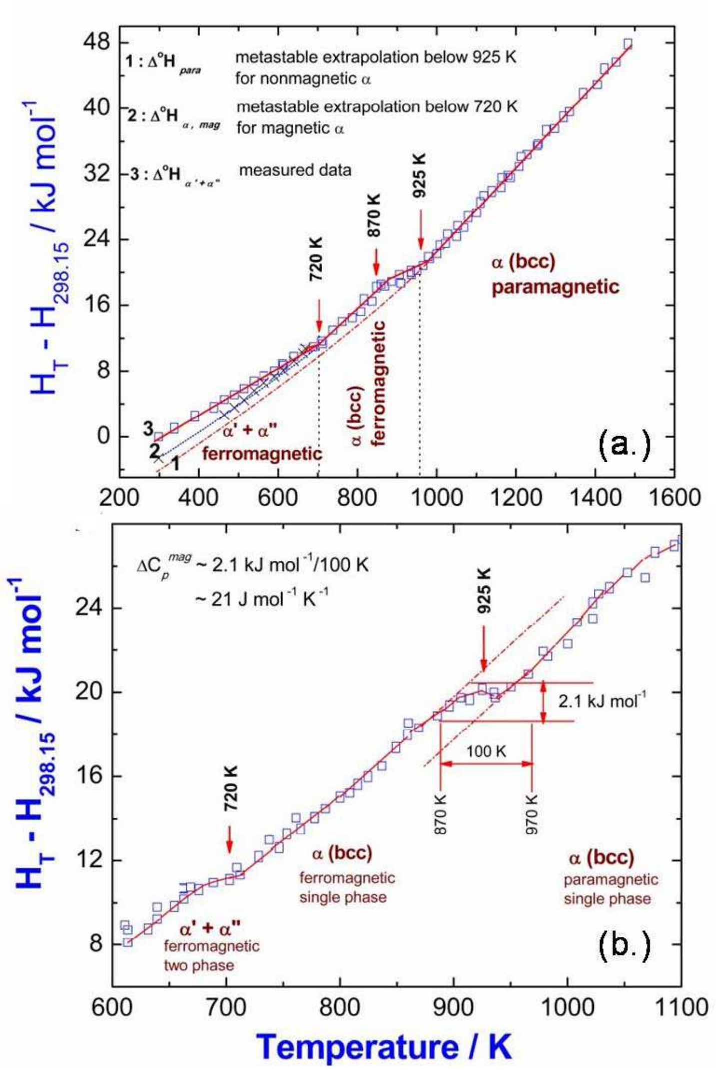

Fig. 4.4 (**a**) Temperature variation of measured enthalpy increment for Fe - 21 at.% Cr alloy and (**b**) the expanded view around α'+α"→α ferro and $\alpha_{\text{ferro}} \rightarrow \alpha_{\text{para}}$ transformations

According to **Fig. 4.5,** Fe - 21 at.% Cr alloy upon heating first undergoes a transformation from two phase α'+α" into α-single phase domain. The system in this temperature domain is still in ferromagnetic domain. This α'+α"→α transformation temperature, as observed from **Fig. 4.5** varies from 477 to 573 ^{0}C (750 to 810 K), depending on various estimates. It is seen that different theoretical studies estimate the α'+α"→α transformation temperature with varying degrees of accuracy [85]. Nevertheless, the available data support the interpretation that the inflection seen at 447 ^{0}C (720 K) in the present drop measurements (**Fig. 4.4**) is most likely to be associated with α'+α"→α transformation.

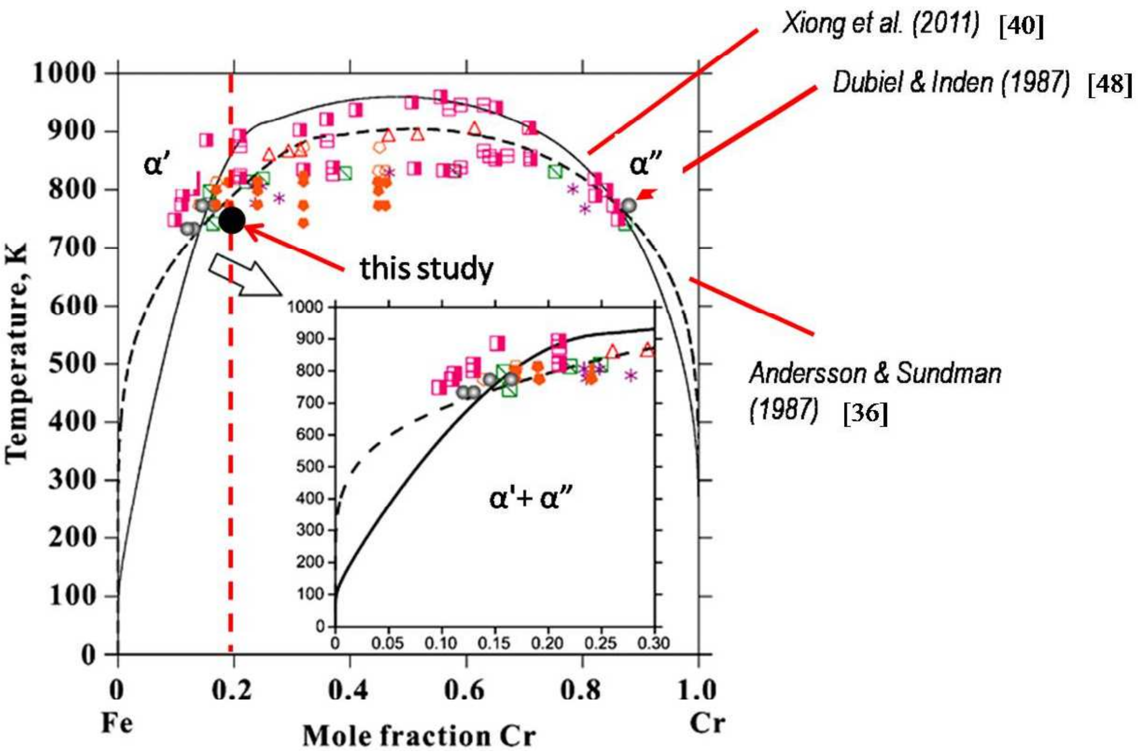

Fig. 4.5 Assessed α→α'+α" miscibility gap domain co-plotted with some of the theoretical estimates

The data on variation of ferromagnetic to paramagnetic transition temperature Tc with X_{Cr}, the mole fraction of chromium is collated in **Fig. 4.6.** These data are mainly taken from the assessment review of Xiong et al. [85]. It is clear that the inflection marked in the drop curve at 652 ^{0}C (925 K) for Fe - 21 at.% Cr alloy is in agreement with the expected Tc of 652 to 667 ^{0}C (925 to 940 K). Hence, the second inflection temperature seen in the drop curve is associated with $\alpha_{ferro} \rightarrow \alpha_{para}$ magnetic transformation. It is recalled that this magnetic phase transition takes place in the single α phase field. To summarize, the drop calorimetry data obtained in this study lends support for the following transformation sequence:

(i) (α'+α") → α at 447±10 ^{0}C (720±10 K);

(ii) $\alpha_{ferro} \rightarrow \alpha_{para}$, at 652±10 ^{0}C (925 ±10 K).

In **Fig. 4.4(a)**, the dash-dotted line marked as #1 represents the metastable extrapolation of enthalpy of high temperature paramagnetic α phase down to room temperature. It is clear from the above discussion that paramagnetic single phase α_{para} is thermodynamically stable only above 652 ^{0}C (925 K). In a similar manner, the dotted line marked as #2 stands for the metastable extrapolation of the enthalpy of ferromagnetic bcc single phase α_{ferro}. The line marked as #3 portrays, the actual measured data, which for temperatures less than 447 ^{0}C (720 K), stands for ferromagnetic α'+α" two phase mixture. Between 447 and 652^{0}C (720 and 925 K), the measured data correspond to ferromagnetic single phase, and for T > 652 ^{0}C (925 K), it is for paramagnetic single phase. These graphical extrapolations into metastable domains are necessary to understand and quantify the enthalpy changes involved in α'+α"→α and $\alpha_{ferro}\rightarrow\alpha_{para}$ phase transformations. This aspect will be taken up for a detailed discussion in the following section.

4.3.1. Data analysis

In view of the occurrence of two phase change events, it is not possible to treat the observed temperature dependence of enthalpy in the temperature domain 25 to 1200 ^{0}C (298 to 1473 K) by a single phenomenological model. It is already mentioned that the alloy exists as α'+α" two phase mixture in ferromagnetic state between 25 and 447 ^{0}C (298 and 720 K). In the legend of **Fig. 4.4(a),** the measured data (#3) in this two-phase domain are denoted as $\Delta^oH_{\alpha'+\alpha''}$. Being bi-phasic as well as ferromagnetic, it is somewhat cumbersome to treat the temperature dependence of enthalpy in the region 25≤T≤447 ^{0}C (298≤T≤720 K) by a simple physical model. As temperature increases, the unmixing reaction α'+α"→α proceeds continuously resulting in a change of volume fractions of both α' and α". The effect of this change on enthalpy variation is difficult to model accurately. To avoid this complexity, the two-phase nature is decoupled and a simple fit is made for the enthalpy $\Delta^oH_\alpha^{ferro}$ of ferromagnetic single phase α down to room temperature. This is done by allowing for the metastable downward extrapolation of experimentally measured data from 447 ^{0}C (720 K) down to 25 ^{0}C (298 K). This downward metastable extrapolation is denoted as #2 in **Fig. 4.4(a).**

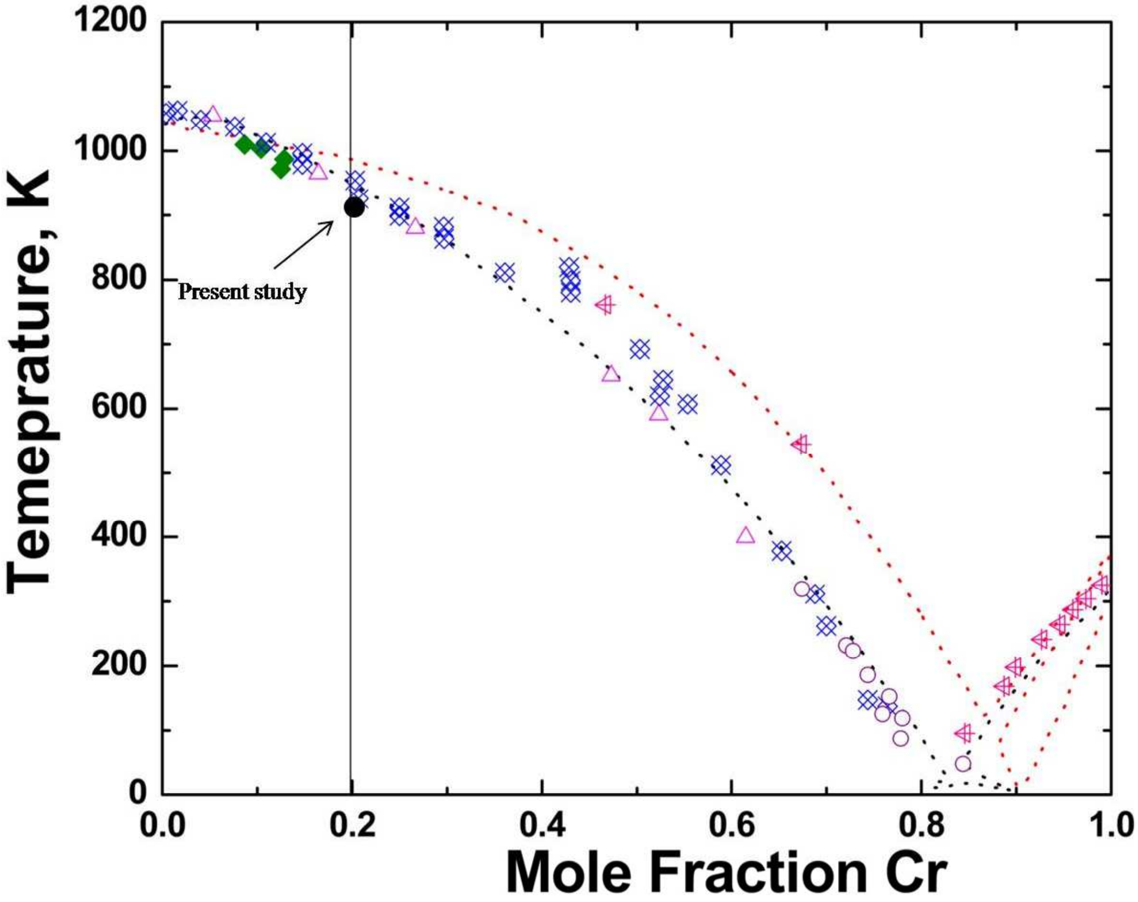

Fig. 4.6 Variation of magnetic transition temperature with Cr content. The plots are adopted from the work of Xiong et al [85]

It must again be recalled that both enthalpy curves, #3 and #2 stand for ferromagnetic state only; therefore the measured difference between the two, that is $(\Delta^oH_{\alpha'+\alpha''}{}^{ferro})_{\#3}-(\Delta^oH_{\alpha}{}^{ferro})_{\#2}$ essentially gives the relative enthalpy of α'+α" two phase mixture over single α phase. Thus, once an estimate of $\Delta^oH_{\alpha}{}^{ferro}$ is obtained for T ≤ 447^0C (720 K), it is then combined with the actual measured data for the temperature domain 447≤T≤597 ^{0}C (720≤T≤870 K). This combined dataset is then subject to a robust fitting over the temperature range, 25≤T≤597 ^{0}C (298≤T≤870 K). The cut off temperature for fitting $\Delta^oH_{\alpha}{}^{ferro}$ is taken as 597 ^{0}C (870 K) in this case, since as seen from **Fig. 4.4(a),** measured enthalpy varies in an irregular fashion in the interval 597≤T≤652 ^{0}C (870≤T≤925 K). The following empirical expression has been used for fitting $\Delta^oH_{\alpha}{}^{ferro}$ as a function of temperature.

$$\Delta^{o}H_{\alpha}^{\ ferro} = aT+bT^{2}+c/T+d. \qquad (4.1)$$

This expression is consistent with the standard Maier-Kelly analytical form (Eq. 4.2) used for fitting the specific heat C_p of regular solids. Thus,

$$C_p^{\alpha,\ ferro} = a'+b'T+c'T^{-2}; \qquad (4.2)$$

It is clear that $a'=a$; b'=2b; and c'= -c. The following fit parameters are obtained for the data obtained in this study.

a /J mol^{-1} K^{-1} = 18.6862±0;

b/J mol^{-1} K^{-2} = 0.01489±0.00045;

c/J K mol^{-1} = 415070.57±0;

d/J mol^{-1} = -9497.13±213;

R^2(fit) = 0.97.

In all these expressions, T is given in K and $\Delta^{o}H_{\alpha}^{\ ferro}$ in J mol^{-1} units. In the second step of data analysis, an estimate of $[(\Delta^{o}H_{\alpha'+\alpha''})-(\Delta^{o}H_{\alpha}^{\ ferro})]$, that is the relative enthalpy of ferromagnetic α'+α" two phase mixture over that of ferromagnetic single phase α is obtained in the temperature range $298.15\leq T\leq 720$ K In this procedure, the difference $\Delta^{o}H_{\alpha'+\alpha''}-\Delta^{o}H_{\alpha}^{\ ferro}$ takes the value of zero at T=447 ^{0}C (720 K) and is gradually increasing in magnitude with decreasing temperature. Thus,

$$\Delta^{o}H_{\alpha'+\alpha''}-\Delta^{o}H_{\alpha}^{\ ferro} = A+B/T+C/T^{2} \qquad (4.3)$$

A/J mol^{-1} = -1631.02 ± 22;

B/J K mol^{-1} = 1086973.44 ± 0;

C/J K^2 mol^{-1} = 153940619 ± 5268;

R^2(fit) = 0.99.

From Eq. (4.1) and (4.3), it is possible to estimate $\Delta^{o}H_{\alpha'+\alpha''}$, the enthalpy of ferromagnetic two-phase mixture as given under.

$$\Delta^{o}H_{\alpha'+\alpha''} = (A+B/T+C/T^{2}) + \Delta^{o}H_{\alpha}{}^{ferro} \qquad (4.4)$$

Substituting for $\Delta^{o}H_{\alpha}{}^{ferro}$ from Eq. (4.1), we get,

$$\Delta^{o}H_{\alpha'+\alpha''} = (A+B/T+C/T^{2}) + (aT+bT^{2}+c/T+d) \qquad (4.5)$$

It is obvious that the above equation is valid only for $T \leq 447\ ^{0}C$ (720 K), since the first contribution on the right-hand side is valid for only $T \leq 447\ ^{0}C$ (720 K). Differentiation of eq. (4.4) with respect to temperature yields temperature dependent C_p values for the α'+α" two phase region. It is very important to note that the magnetic contribution to enthalpy of α'+α" two phase mixture, which in itself is temperature dependent, is only implicitly included in the above data fitting procedure.

Nevertheless, in order to obtain explicitly an experimental estimate of the magnetic contribution to enthalpy and hence to specific heat, one needs to obtain first $\Delta^{o}H_{\alpha}{}^{para}$ (T), the baseline enthalpy for the paramagnetic single phase. If $\Delta^{o}H_{\alpha}{}^{para}$ (T) is known, then it is a straight forward exercise to get magnetic contribution to enthalpy, simply as the difference between $\Delta^{o}H_{\alpha}{}^{para}(T)$ and $\Delta^{o}H_{\alpha}{}^{ferro}(T)$ in the concerned temperature domain. Now following the same procedure as that adopted for obtaining $\Delta^{o}H_{\alpha}{}^{ferro}$, one can obtain an analytical fit for $\Delta^{o}H_{\alpha}{}^{para}$, the enthalpy increment for the paramagnetic single phase α in the temperature region 25 to 1200 ^{0}C (298 to 1473 K). Again this is done by combining the extrapolated data in the metastable temperature domain ($298 \leq T \leq 925$ K) with the actual measured data in the range, $925 \leq T \leq 1473$K. The metastable downward extrapolation for the enthalpy of paramagnetic bcc phase is marked as # 1 in **Fig. 4.4(a).** Without going into further elaboration and adopting the same procedure as described above, the final analytical expression for $\Delta^{o}H_{\alpha}{}^{para}(T)$ is obtained as follows.

$$\Delta^{o}H_{\alpha}{}^{para} = eT+fT^{2}+g/T+h \qquad (4.6)$$

The values of fit coefficients are:

$e/\mathrm{J\ mol^{-1}\ K^{-1}} = 23.11\pm0$

$f/\mathrm{J\ mol^{-1}\ K^{-2}} = 0.01012\pm0.00014$

$g/\mathrm{J\ K\ mol^{-1}} = 655844.98.\pm0$

$h/\mathrm{J\ mol^{-1}} = -13384.44\pm 977.93$

$R^2(\mathrm{fit}) = 0.98$

It may be noted that Eq. (4.6) is valid in the entire temperature range of 25 – 1200 ^{0}C (298-1473 K). Thus, in the final analysis, Eq. (4.1), (4.5) and (4.6) yield a compact numerical representation of the temperature dependencies of three enthalpy increments, namely $\Delta^oH_\alpha{}^{\mathrm{ferro}}$, $\Delta^oH_{\alpha'+\alpha''}$ and $\Delta^oH_\alpha{}^{\mathrm{para}}$ respectively. These expressions can be used to obtain respective specific heats as well. Before closing this section, it is useful to note from **Fig. 4.4(b),** that in the vicinity of $\alpha^{\mathrm{ferro}}\rightarrow\alpha^{\mathrm{para}}$ magnetic transformation, i.e in the temperature range of 597-697 ^{0}C (870 to 970 K) the observed enthalpy variation temperature is such that the enthalpy and specific heat cannot be described by a simple polynomial fitting as this would give rise to spurious oscillations in C_p. However, an approximate estimation of the maximum magnetic contribution to specific heat at the Curie temperature 652 ^{0}C (925 K) is still possible graphically. In **Fig. 4.4(b),** the method of obtaining $\Delta C_p{}^{\mathrm{mag}}$ is illustrated. As judged from the observed trend in **Fig. 4.4(b),** the effect of magnetic transition on enthalpy is rather diffuse and spread over 100 K temperature domain on either side of T_c. In the present study, it is estimated that a net enthalpy difference $\Delta H_{\mathrm{mag}} = 2.1$ kJ mol^{-1} is involved over a temperature interval of ~100 K. This enthalpy change corresponds to a net change in specific heat $\Delta C_p{}^{\mathrm{mag}} = \Delta H^{\mathrm{mag}}/\Delta T$, of ~21 J mol^{-1} K^{-1}. This estimated value is in excellent agreement with 22.52 J mol^{-1} K^{-1}, that is reported for Fe-21 at.% Cr alloy [40]. In the following section, a physically based modeling of specific heat in terms of contributions such as, vibrational, electronic and magnetic ones is attempted. It must however be added that this modeling is only for the specific heat of single phase α (bcc) and as such does not incorporate the $\alpha'+\alpha''\rightarrow\alpha$ phase transformation effect encountered for T less than 447 ^{0}C (720 K).

4.4. Modelling of specific heat

In general terms, the isobaric specific heat C_p of a condensed phase is related to C_v, the isochoric specific heat by the following relation [183].

$$C_p = C_v\,(1+\gamma_G\alpha_v T) \qquad (4.7)$$

In the above expression, C_v is the isochoric specific heat, γ_G is the thermal Grüneisen parameter and α_v is the coefficient of volume thermal expansion. The thermal Grüneisen parameter is given as,

$$\gamma_G = \alpha_v B_s V_m/C_p \qquad (4.8)$$

Here, B_s, and V_m stand for adiabatic bulk modulus and thermodynamic (molar) volume respectively. Further, it is customary to express C_v in terms of following phenomenological contributions.

$$C_v= C_{vib}^{h} + C_v^{a} + C_v^{mag} + C_v^{el} \qquad (4.9)$$

In Eq. (4.9), C_{vib}^{h} is the harmonic contribution (approximation) to vibrational specific heat, often expressed in terms of Einstein, Debye or superposed Einstein+Debye models [184]; C_v^{a} is the anharmonic correction term, that can be represented in terms of quasi-harmonic formalism to the first order approximation, if information is lacking about the full details of phonon spectra; C_v^{mag} is the magnetic contribution; and C_v^{el} is the electronic contribution to specific heat. In line with this approach, the total specific heat Cp of single phase ferromagnetic α in the complete temperature region -273 to 1200 ^{0}C (0 to 1473 K) is expressed by the following set of expressions.

$$C_v^{\,ferro}(T) = C_{vib} + \Gamma_e T + p_1 T + p_2 T^2 + p_3 T^4 + C_p^{mag} \qquad (4.10)$$

$$C_{vib} = 3R\times(\theta_E/T)^2\{(\theta_E/T)/(e^{\theta_E/T}-1)^2\} \qquad (4.11)$$

$$C_p^{mag}/R= \ln(\beta+1)\times C(\tau) \qquad (4.12)$$

$$C(\tau) = \{(474/497)\times(1/p-1)\times(2\tau^{3}+2\tau^{9}/3+2\tau^{15}/5)\}/D; \qquad (4.13)$$

$$\text{for } \tau=(T/T_c)\leq 1 \qquad (4.13a)$$

$$C(\tau) = (2\tau^{-5}+2\tau^{-15}/3+2\tau^{-25}/5)\}/D; \qquad (4.14)$$

$$\text{for } \tau=(T/T_c)>1 \qquad (4.14a)$$

Eq. (4.10) is a slightly modified form of the expression used by Chen and Sundman [188]. In the present study, Einstein model is used for representing the harmonic contribution to vibrational specific heat. θ_E is the Einstein temperature; and Γe is the coefficient of electronic specific heat; p1, p2 and p3 are empirically adjusted fit parameters. The anharmonic contribution is not explicitly incorporated, but it is implicitly accounted for in the empirical fit constant p1. The magnetic contribution is given in terms of Hillert-Jarl phenomenological model [97]. Alternately, other classical models due to Inden [96] or Chuang [35] can also be used. β is the average magnetic moment (in Bohr magneton unit) per atom; $C(\tau)$ is a series expansion in the dimensionless temperature $\tau=T/Tc$; p is a structure dependent parameter characterizing the fraction of magnetic enthalpy absorbed above Tc. It takes a value of 0.4 for bcc lattice with an associated value for D=1.55828482 [182]. At present, there seems to be no information on experimentally determined saturation magnetic moment value for Fe - 21 at. % Cr composition. Fortunately, theoretical estimates of this quantity are available [71]. In the present study, the value of $\beta=1.6$ is used, which is taken from the spin polarized DFT calculations of magnetically ordered Fe-Cr alloys [71]. With a β value of 1.6, the application of Hillert-Jarl model at Tc = 652 ^{0}C (925 K) gives a value of 2.65 kJ mol^{-1} for magnetic enthalpy ΔH_{mag}. This compares well with the present model independent experimental estimate of 2.1 kJ mol^{-1} (**Fig. 4.4(b)**). The value of ΔC_p^{mag} at Tc = 652 ^{0}C (925 K) as estimated by the Hillert-Jarl model is 22 J mol^{-1} K^{-1}.

For estimating the vibrational contribution, θ_E can be approximately set equal to $0.77\theta_D$, where θ_D is the Debye characteristic temperature [184]. The electronic coefficient of specific heat Γ_e as well as θ_D can be estimated if low temperature ($T \leq \theta_D/50$) C_p data are available. At present, experimental C_p data for such low temperatures are not available for Fe - 21 at.% Cr composition. However, Γ_e can also be obtained from the theoretically calculated electron density of states at the Fermi energy $N(E_F)$, by using the formula [183],

$$\Gamma_e = \pi^2 k_B^2 N(E_F)/3 \qquad (4.15)$$

k_B is the Boltzmann constant. In the present study, the value of $N(E_F) = 13$ states/Ry, taken from the theoretical study of Korzhavyi et. al, [71] is used. This gives for Γ_e, a value of 2.252 mJ mol^{-1} K^{-2}. There have been some estimates of θ_D for Fe-Cr alloys as a function of composition, both from *ab-initio* elastic property calculations [72-73], Mossbauer spectroscopy [59], and X-ray Debye-Waller factor studies [189]. The Mossbauer θ_D values differ slightly from elastic θ_D estimates and further do not bear the same systematic trend with Cr concentration, as for example borne by θ_D elastic values. In the present study, elastic θ_D is independently estimated using Moruzzi's approximate formula involving molar volume (V_m), molar mass (M) and isothermal bulk modulus (B_T) [190].

$$\theta_D = 0.617(6\pi^2)^{1/3}\,(h/2\pi k_B)(V_m^{1/3}B_T/M)^{1/2} \qquad (4.16)$$

Substituting the values of constants in Eq. (4.16), and assuming $V_m^{1/3} \propto r_o$, the equilibrium value of the near neighbor distance,

$$\theta_D/K = 41.63\times[r_oB_T/M]^{1/2} \qquad (4.17)$$

r_o in the above expression is given in atomic units (1 a.u.=0.529×10^{-10}m) and B_T in kbar units. For Fe-21Cr, r_o =4.6545 a.u. (this study); B_T =1930 kbar is adapted from the theoretical study of Zhang et al., [72]. Although there is a small spread among diverse theoretical estimates of elastic properties, the chosen bulk modulus value reflects the trend exhibited by available limited experimental data [48]. The calculated θ_D is 260 ^{0}C (533 K) for Fe-21 at.% Cr, while the reported θ_D varies from 181 to 119 ^{0}C (454 to 392 K) [59, 72, 77, 189]. In fact, in two different theoretical studies, Zhang et al., gave two estimates of θ_D = 181 ^{0}C (454 K) and 260 ^{0}C (533 K) for Fe - 21 at.% Cr alloy [72, 77]. In the present study, the value of 260 ^{0}C (533 K) for θ_D is taken, as it gives a good match for the estimated room temperature C_p with the only experimental estimate due to Schroder [52]. Thus, the calculated value of $C_v = C_v + \Gamma_e T$ = 21.75 J mol^{-1} K^{-1}, which agrees well with the value 20.95 J mol^{-1} K^{-1}reported by Schroeder [52].

The thermal Grüneisen parameter γ_G, required to get C_p from C_v is estimated from Eq. (8). γ_G at 25 ^{0}C (298 K) is estimated to be 1.67, with $\alpha_v = 3.38\times10^{-5}$ K^{-1} [191]; C_v=21.27 J mol^{-1} K^{-1}(present study); $V_m = 3.8524\times10^{-6}$ m^3 (present study) and $B_T = 193\times10^9$ Nm^{-2} [72, 77]. It may also be added that γ_G, can also be estimated independently from the knowledge of Poisson ratio (σ) [72, 77], which is directly obtained from the principal elastic modulii E and G. Thus, γ_G^{el}

$$\gamma_G^{el} = 3/2\{(1+\sigma)/(2-3\sigma)\}. \tag{4.18}$$

$$1+\sigma = E/2G. \tag{4.19}$$

$$1-2\sigma = E/3B. \tag{4.20}$$

Based on the available theoretical estimates of E and G [x], σ for Fe - 21 at.% Cr alloy is found to be in the range, 0.203-0.265. Accordingly, γ_G^{el} varies from 1.297 to 1.575, which compares reasonably well with a value of 1.67 obtained for thermal Grüneisen parameter using Eq. (4.8). Having thus estimated all the necessary input parameters, the $C_p^{para}(T)$ of hypothetical paramagnetic single-phase Fe - 21 at.% Cr alloy can be set up in the following manner.

$$C_p^{para}(T) = C_v(1+\gamma_G\alpha_v T) + \Gamma_e T + p_1 T + p_2 T^2 + p_3 T^4 \tag{4.21}$$

The constants, p1, p2 and p3 are obtained by means of nonlinear least square regression of the experimentally obtained C_p^{para}(T) data, which is given by the differential of Eq. (4.6).

p_1/J mol^{-1}K^{-2} = 0.011 ± 0.003

p_2/J mol^{-1}K^{-3} = $1.9\times10^{-6} \pm 4.3\times10^{-8}$

p_3/J mol^{-1}K^{-5} = $7.59\times10^{-15} \pm 3.29\times10^{-17}$

The magnetic contribution, C_p^{mag} is then calculated independently using Eq. (4.12), (4.13) and (4.14), with β =1.6 and added to Eq. (4.21) to obtain C_p^{ferro}(T). In **Table 4.1**, the list of input parameters used in model-based estimation of C_p is presented. In **Fig. 4.7(a)**, the different contributions to model-based C_p are graphically displayed along with the experimental data coming from the present study and the low temperature values taken from Schroder [52]. **Fig**. 4.**7(b)** highlights the experimentally determined paramagnetic and ferromagnetic contributions to specific heat. It is well known that in Fe-base alloys containing magnetic transition metal elements, the possibility of complex magnetic ordering can play a decisive role in dictating thermodynamics and phase stability, especially at low temperatures [84]. The contribution of this magnetic order to thermal stability is rather substantial as for example seen from the magnitude of C_p^{mag} estimated in this study (**Fig. 4.7(b)**). Notwithstanding the numerous theoretical first principles and semi empirical studies on Fe-Cr binary system, a rigorous, transparent treatment of the role magnetic short-range order in influencing phase stability incorporating in it, the compositional and temperature effects on equal footing is proving to be elusive yet. On the experimental front, achieving true thermodynamic equilibrium is also difficult as this requires substantially long annealing times at moderate temperatures.

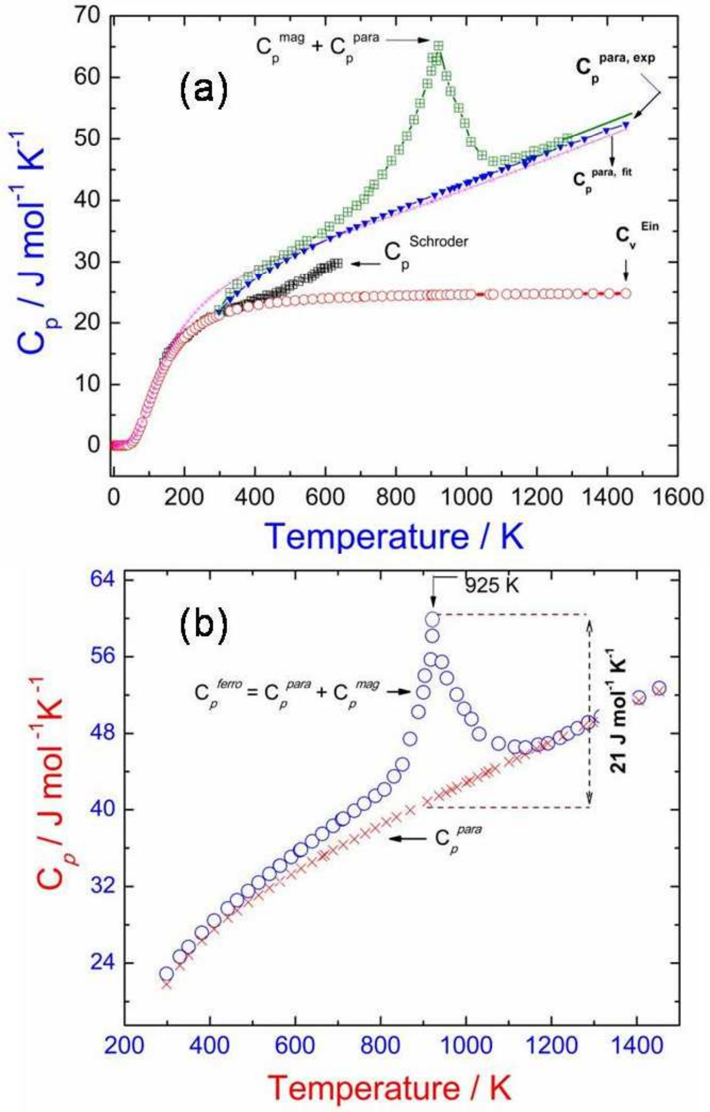

Fig. 4.7 Different contributions to model based C_p are compared with the experimental data coming from this study and that of Schroder [52] at low temperatures

In view of this, the available phase boundary data on (α'+α")/α miscibility gap are expectedly shrouded with considerable uncertainty and variations. It is interesting to note that the present calorimetric estimate of 447±10 ^{0}C (720 ±10 K) as the temperature of α'+α"→α transformation in the ferromagnetic state, is in accord with the theoretical estimate of 447 ^{0}C (720 K), which as noted in the work of Wallenius *et al.*, signifies the drastic change in the unmixing kinetics in Fe-Cr alloys [86]. To the best of my knowledge, no recent thermal analysis or other direct determination of α'/α'+α"phase boundary has been made as a function of Cr concentration to facilitate a good comparison. Naturally, more experimentation on alloys with varying Cr content is necessary for getting further insight into this important gap area. Further, it is equally important to carry out such thermal analysis studies on specimen that have been aged for long durations of time at moderate temperatures well within the α’+α” two phase domain.

Table 4.1

List of input parameters used in the model-based estimation of C_p values.

Lattice parameter at room temperature (nm)	0.2852 (α’-Fe rich bcc) 0.2864 (α”-Cr rich bcc)	Present Study
B_T at 27^0C (300 K) (GPa)	194	Korzhavyi et al. [71]
	193	Zhang et al. [72]
	196	Razumovskiy et.al. [74]
C_P at 25^0C (298.15 K) ($\mathrm{J\ mol^{-1}\ K^{-1}}$)	21.75	Present study
	20.95	Schroder [52]
Cp^{mag} (T_c) ($\mathrm{J\ mol^{-1}\ K^{-1}}$)	21.73	Present study
	22.52	Xiong et al. [40]
H^{mag} (T_c) $\mathrm{kJ\ mol^{-1}}$	2.64	Hillert-Jarl Model with T_c=652^0C (925 K)
	2.0	Present experimental estimate
Θ_D (K)	181 ^{0}C (454 K)	Zhang et al. [72]
	260 ^{0}C (533 K)	Zhang et al. [72]
	190^0C (463 K)	Jithender et al. [189]
	260^0C (533 K)	Present study
α_v at 25^0C (298.15 K)/ K^{-1}	3.382×10^{-5}	Linderoth and Larsen [191]
T_c (K)	652^0C (925 K)	Present Drop Study
	656^0C (929 K)	Xiong et al. [85]

The (α’+α”)/α transus data thus obtained would be of immense help in assessing the extent of deviation from true thermodynamic equilibrium. The experimental value of Curie temperature Tc = 652^0C (925 K) recorded in this study is good agreement with many reported literature data [85]. Also, the magnitudes of the magnetic specific heat and enthalpy estimated in this study are in good agreement with independent theoretical estimates of Ruban et al. [75].

In **Table 4.2**, the measured enthalpy and specific heat values for select temperatures are presented.

Table 4.2

Experimentally obtained enthalpy increment and specific heat values for Fe - 21 at.% Cr alloy tabulated for select temperatures. Percentage deviation is defined as 100×(Exp.-Fit)/Exp.

Temperature (K)	H_T–$H_{298.15}$ (J mol^{-1}) Experiment	H_T–$H_{298.15}$ (J mol^{-1}) Fitted	Deviation from Fit (%)	C_p (J mol^{-1}K^{-1})
		(α'+α") –Ferromagnetic two phase domain		
25 ^{0}C (298 K)	0	0	-	21.75
177 ^{0}C (450 K)	4135.7	4393.9	-5.88	28.04
227 ^{0}C (500 K)	5658.4	5557.3	1.82	30.03
277 ^{0}C (550 K)	6950.4	6893.4	0.83	31.95
327 ^{0}C (600 K)	8450.1	8375.0	0.90	33.80
377 ^{0}C (650 K)	10164.1	9984.1	1.80	35.60
427 ^{0}C (700 K)	11403.01	11708.2	-2.61	37.36
		Ferromagnetic single α Phase		
477 ^{0}C (750 K)	12908.0	13446.5	-4.17	39.08
527 ^{0}C (800 K)	15474.9	15500.2	-0.16	39.90
577 ^{0}C (850 K)	17426.3	17632.5	-1.18	40.64
627 ^{0}C (900 K)	20158.6	19842.5	1.57	41.46
		Paramagnetic α Phase		
677 ^{0}C (950 K)	19547.5	18386.5	5.9	41.76
727 ^{0}C (1000 K)	21506.6	20493.8	4.7	42.85
777 ^{0}C (1050 K)	23733.5	22654.9	4.5	43.93
827 ^{0}C (1100 K)	25698.3	24869.6	3.2	45.00
877 ^{0}C (1150 K)	28370.1	27137.3	4.3	46.07
927 ^{0}C (1200 K)	30217.6	29457.8	2.5	47.13
977 ^{0}C (1250 K)	31953.2	31830.7	0.38	48.18
1027 ^{0}C (1300 K)	34016.3	34255.9	-0.70	49.23
1077 ^{0}C (1350 K)	35882.9	36733.3	-2.4	50.28
1127 ^{0}C (1400 K)	38994.1	39262.6	-0.69	51.33
1177 ^{0}C (1450 K)	41122.7	41843.6	-1.8	52.37

To the best of my knowledge, this is the first reported high temperature thermodynamic data on Fe - 21 at.% Cr over the temperature region, which spans two technologically important phase transformations. As mentioned in the introduction, there are not many high temperature calorimetry investigations in Fe-Cr alloys in the composition range of interest to nuclear industry. The most extensive calorimetry data on Fe-Cr system available as on date are from the pioneering work of Normantan *et al* [33]. However, even in this classical study, an explicit determination of the magnetic contribution to specific heat has not been made for Fe - 21 at.% Cr alloy. As it is obvious from the plethora of recent theoretical studies on Fe-Cr system, it is certain that a realistic incorporation of magnetic contribution to total Gibbs energy is mandatory for capturing the full and correct description of phase equilibria in magnetic transition metal systems [95-97]. While DFT based theoretical calculations, depending on the extent of technical sophistication, are of great help in estimating the magnetic part of total free energy at zero Kelvin temperature, a realistic incorporation of the mutually influencing effects of temperature and Cr concentration is rather difficult on purely *ab-initio* grounds. It is in this context, that accurate calorimetry measurements of high temperature thermodynamic quantities are of immense help, since this would effectively supplement the vast theoretical database that is already building up on Fe-Cr system. The present study is a small contribution in this direction.

4.5. Summary and Conclusions

(i) High temperature drop calorimetry measurements have been made on solution annealed Fe-21 at. %Cr alloys in the temperature range of 25 to 1200 ^{0}C (298.15 to 1473 K). X-ray diffraction and metallography supported the presence of α’ (Fe rich bcc) +α” (Cr rich bcc) two phase microstructure.

(ii) The following sequence of phase transformations with increasing temperature has been established based on calorimetry data: α'(Fe-rich)+α"(Cr-rich)→α at 447±10 ^{0}C (720 ±10 K) and α_{ferro}→α_{para} at 652±10 ^{0}C (925 ±10 K).

(iii) The unmixing reaction, α'(Fe-rich)+α"(Cr-rich)→α(single homogeneous bcc) occurred continuously with increasing temperature and reached a culmination at 447 ^{0}C (720 K), at which temperature, the enthalpy curve exhibited a small inflection, which makes it difficult to associate a definite jump in enthalpy with this transformation. However, the $\alpha'+\alpha''\to\alpha$ transformation takes place well within the domain of ferromagnetic stability, implies that the enthalpy of α'(Fe-rich) phase is influenced by magnetic contributions.

(iv) The measured enthalpy data have been treated individually in different temperature domains, by resorting to downward metastable extrapolations. Thus, a phenomenological separation of the relative enthalpy of $\alpha'+\alpha''$ over single phase α is achieved in the temperature regime, where ferromagnetic single phase α is metastable. On similar lines, the enthalpy of paramagnetic single phase α has also been obtained in the entire temperature region of measurement. In this manner, explicit fitting of enthalpy data for ferromagnetic two-phase mixture, ferromagnetic single phase and paramagnetic single phase have been obtained as a function of temperature.

(v) The magnetic contribution to specific heat ΔC_p^{mag} estimated at Tc = 652^{0}C (925 K) by Hillert-Jarl model is in agreement with the experimental estimate. The magnetic contribution to enthalpy is estimated to be about 2 kJ mol^{-1} at Tc=652^{0}C (925 K), while the value of ΔC_p^{mag} is found to be 21 J mol^{-1} K^{-1}.

Chapter – 5

Study of sigma (σ) → alpha (α) transformation characteristics in Fe-Cr model alloy by dynamic calorimetry

5.1 Introduction

Sigma (σ) phase is reported to form after long term exposure at high temperature under hostile corrosive environment for ferritic [99-100], austenitic [101-103] and duplex steels [20, 104-105]. Formation of σ phase affects mechanical properties namely creep ductility [111] and low cycle fatigue [112]. The corrosion resistance [113] of structural materials is also affected by sigma phase formation. Many in-service failures were also reported due to σ-phase formation. The premature failure of 316 SS secondary super heater boiler tube due to enhanced creep cavitation associated with σ formation is reported by Chastell and Flewitt [117]. Accelerated ageing of Gas Tungsten Arc Welds of 316FR SS also lead to the nucleation of σ at δ/γ interphase boundary which was predicted to affect the repair weldability of the steel [120]. It is worth mentioning here that the nucleation of sigma phase in advanced steel, be it ferritic, austenitic or duplex, has its origin in the Fe-Cr binary system. In Fe-Cr binary, σ is a stable equilibrium phase which exists at high temperature and can be stable upto 77 GPa and has low compressibility than both the constituent elements [21]. There has been a wealth of literature on the metallurgical aspect of sigma phase of Fe-Cr and related systems [21, 85]. However, very few studies were reported on high temperature thermal stability and thermo-physical properties of sigma (σ) phase [85]. In this chapter, a comprehensive evaluation of high temperature phase stability and phase transformation kinetics is carried out in the temperature range of 100 – 1200 ^{o}C (373 K to 1473 K) for sigma and parent alpha phase of $Fe_{54}Cr_{46}$ alloy by Differential Scanning Calorimeter.

5.2 Synthesis and characterization of σ phase

Binary alloys of nominal composition $Fe_{54}Cr_{46}$ were prepared by arc melting of accurately weighed high pure Fe and Cr granules under flowing high pure Ar atmosphere. In order to maintain chemical homogeneity, melted alloys were re-melted several times under similar atmosphere. Homogenization treatment of these alloys was carried out at 1050 ^{0}C

(1323 K) for 24 h in a vacuum furnace to obtain the parent phase. A part of the alloy was vacuum sealed (10^{-6} Pa) in a quartz tube.

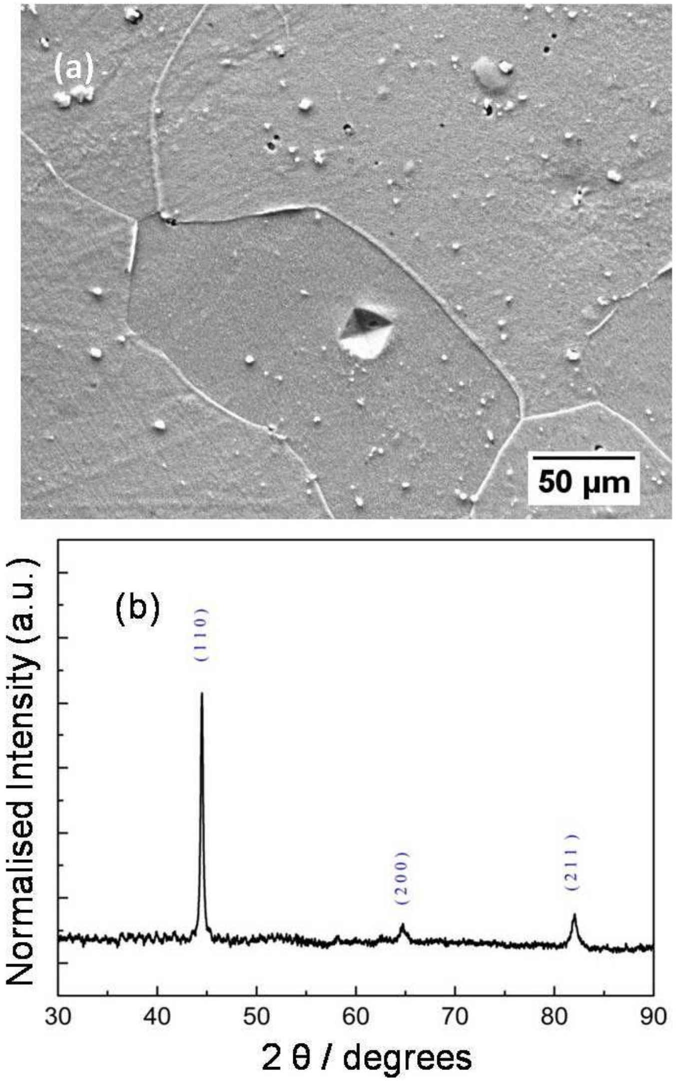

Fig. 5.1 (a) Microstructure and (b) XRD profile of homogeneous $Fe_{54}Cr_{46}$ alloy

The vacuum sealed alloy was first heated to 1000 ^{0}C (1273 K) held for 15 minutes and then annealed for 360 h at 700 ^{0}C (973 K) for synthesis of sigma phase (product phase) followed by water quenching. SEM micrograph of parent phase in **Fig. 5.1(a)** shows a typical polygonal ferrite microstructure with grain size varying in the range of 30 - 100 µm. Average Vickers hardness of this phase has been measured as 320 VHN. The room temperature XRD of parent phase is presented in **Fig. 5.1(b).** Three distinct peaks corresponding to (110), (200), (211) of bcc ferrite are observed for parent α phase. The lattice parameter was estimated as 0.287 nm which is in good agreement with literature [85]. Based on the above observations, it is evident that parent phase exists as single phase α ferrite. The microstructure of annealed alloy is shown in **Fig. 5.2(a)**.

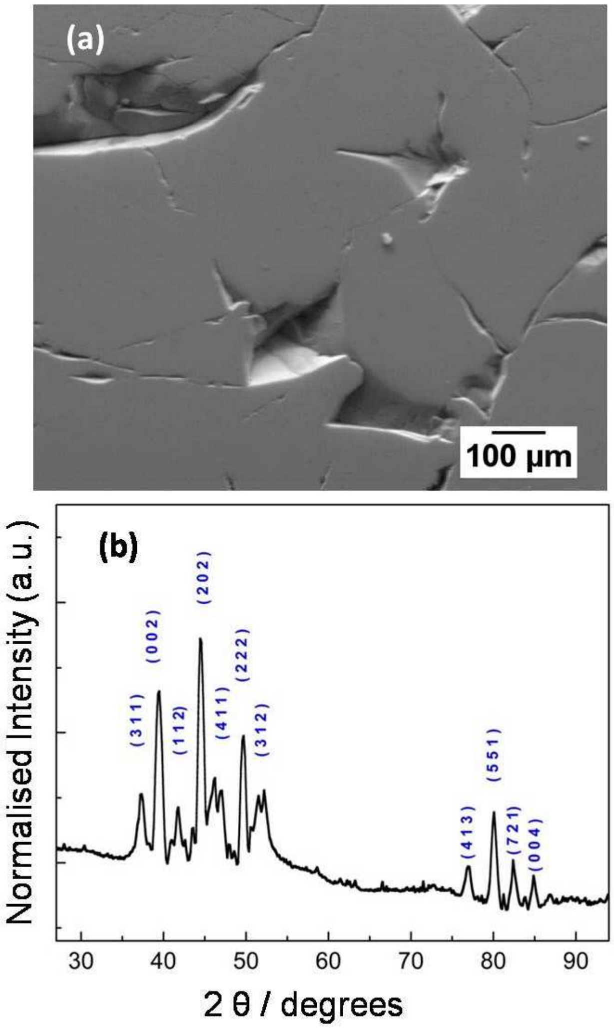

Fig. 5.2 (a) Microstructure and (b) XRD profile of product phase of (annealed at 700 ^{o}C (973 K) for 360 h) $Fe_{54}Cr_{46}$ alloy

The average Vickers hardness of annealed alloy is measured as 1180 VHN which is much higher than the hardness (320 VHN) of the parent alpha phase. Several microcracks are clearly observed in **Fig. 5.2(a)** which indicates the hard and brittle nature of sigma phase in contrast to its parent alpha phase. The XRD pattern of the long term annealed alloy (product phase) is given in **Fig. 5.2(b)**. A critical analysis of XRD spectrum in **Fig. 5.2(b)** reveals the presence of a phase with tetragonal structure and lattice parameter of a = 0.882 nm and c =

0.455 nm. The atomic planes corresponding to each peak position in the pattern have been identified and shown in **Fig. 5.2(b)**. It is evident that the structure corresponds to sigma phase. It is important to mention here that no residual bcc phase is observed in **Fig. 5.2(b)** which confirms the complete conversion of alpha to sigma during the annealing treatment.

5.3. Phase transformation characteristics of α and σ phase by DSC

The DSC thermogram of heating/cooling profile for alpha phase carried out using heating/cooling rate of 10 K min^{-1} upto 1100 ^{0}C (1373 K) is shown in **Fig. 5.3**.

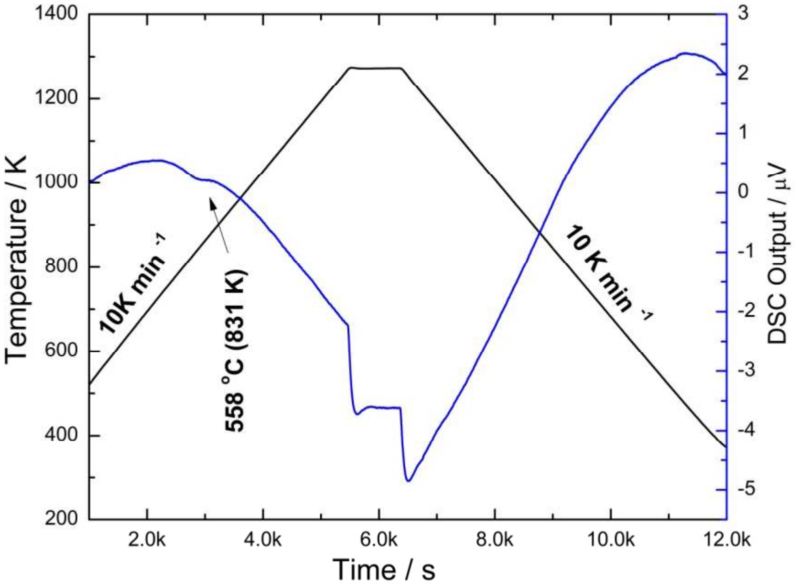

Fig. 5.3 DSC heat flow diagram of homogenized alpha phase (α) of $Fe_{54}Cr_{46}$ alloy at 10 K min^{-1} heating and cooling rates

A single phase transformation event is observed at 558 ^{0}C (831 K) in the heating profile from **Fig. 5.3**. This is attributed to the ferro to para magnetic transformation of α phase. The measured Curie temperature of this alloy is 558 ^{0}C (831 K) which is in aggrement with literature [85]. No other phase transformation is observed for alpha phase upto 1100 ^{0}C (1373 K). A repeat DSC run was carried out with the previously DSC cooled sample under identical experimental schedule which yielded the same results. This suggests that the $\alpha \rightarrow \sigma$ phase transformation cannot be studied by dynamic thermal hysterisis due to its extremely sluggish kinetics. The DSC thermogram of the σ phase (product phase) employing the same heating/cooling rate of 10 K min^{-1} is shown in in **Fig. 5.4**.

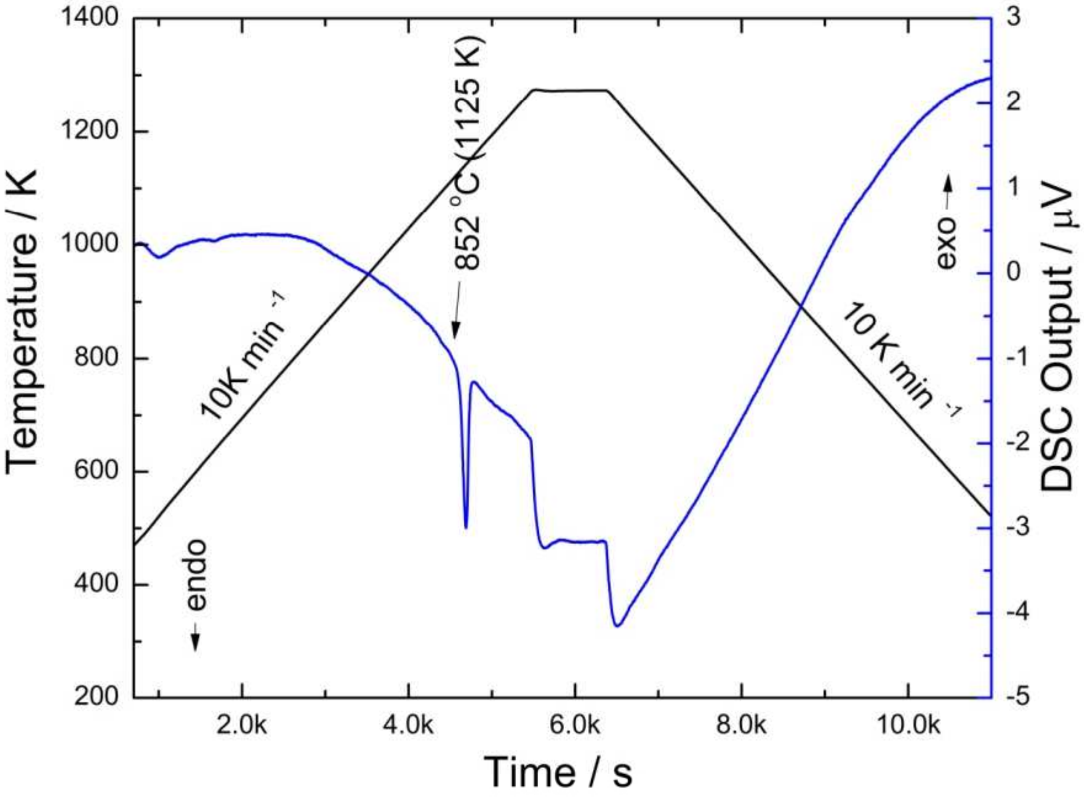

Fig. 5.4. DSC heat flow diagram for sigma (σ) phase of $Fe_{54}Cr_{46}$ alloy at 10 K min^{-1} heating and cooling rates

The thermogram clearly shows an event at 852 ^{0}C (1125 K) during heating which corresponds to the σ →α phase transformation. It is important to mention that the reverse transformation of α →σ is not observed during cooling in **Fig. 5.4**. The results of repeat DSC experiments with the another sigma phase sample is illustrated in **Fig. 5.5**. This repeat experiment shows a therogram identical to that observed for alpha phase in **Fig. 5.5**. These experiments lead to the inference that the sigma phase once decomposed to alpha phase does not revert back during cooling, which is understood as owing to the slow kinetics of α →σ phase transformation.

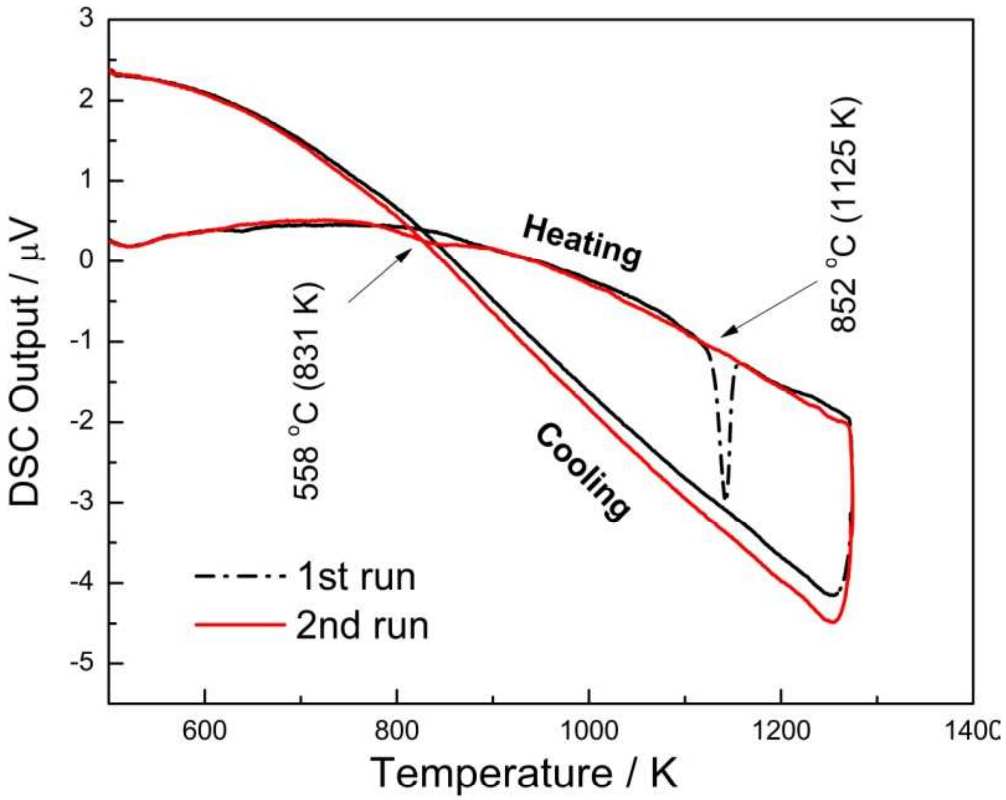

Fig. 5.5. Heat Flow diagram of repeat experiments for sigma (σ) phase of $Fe_{54}Cr_{46}$ alloy at 10 K min^{-1} heating and cooling rates

The microstructure and hardness of post DSC cooled sigma phase samples show identical behavior as observed for alpha phase. It is observed from **Fig. 5.5** that the σ → α phase transformation temperature is about 852 ^{0}C (1125 K) at 10 K min^{-1} heating rate which is ~ 32 K higher then the accepted temperature of 820 ^{0}C (1093 K) reported in the latest Fe-Cr phase diagram by Xiong et al [85]. This may be due to the relatively higher heating rate (10 K min^{-1}) employed in this study which shifts the transformation at higher temperatures. Hence, the σ → α phase transformation has been studied as a function of heating rate to obtain the transformation temperature under pseudo equlibrium condition. Various heating rates of 1 - 50 K min $^{-1}$ was employed to study the σ → α phase transformation. The heat flow curves of σ → α phase transformation of DSC thermogram as a function of various heating rates is illustrated in **Fig. 5.6**. The σ → α transformation temperature is measured as 852 °C (1125 K) and 863 °C (1136 K) for heating rates of 10 and 50 K min^{-1} respectively.

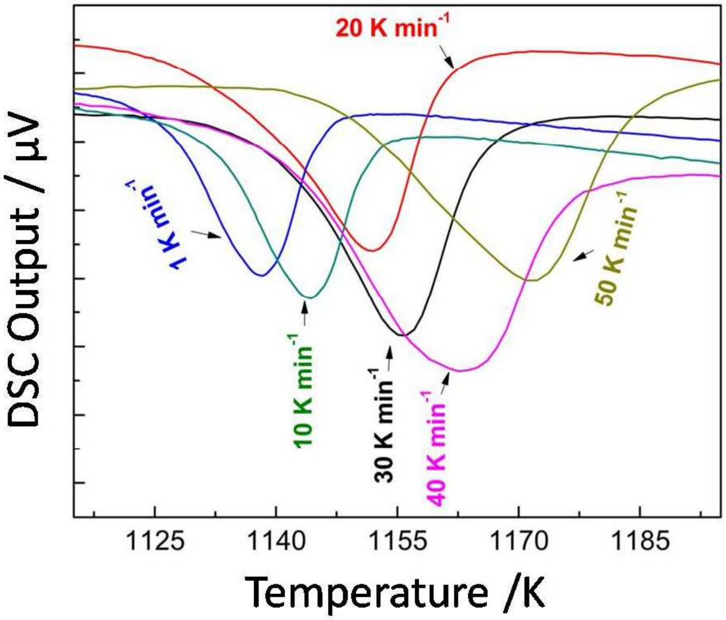

Fig. 5.6 Effect of heating rate on sigma (σ) to alpha (α) phase transformation in $Fe_{54}Cr_{46}$ alloy

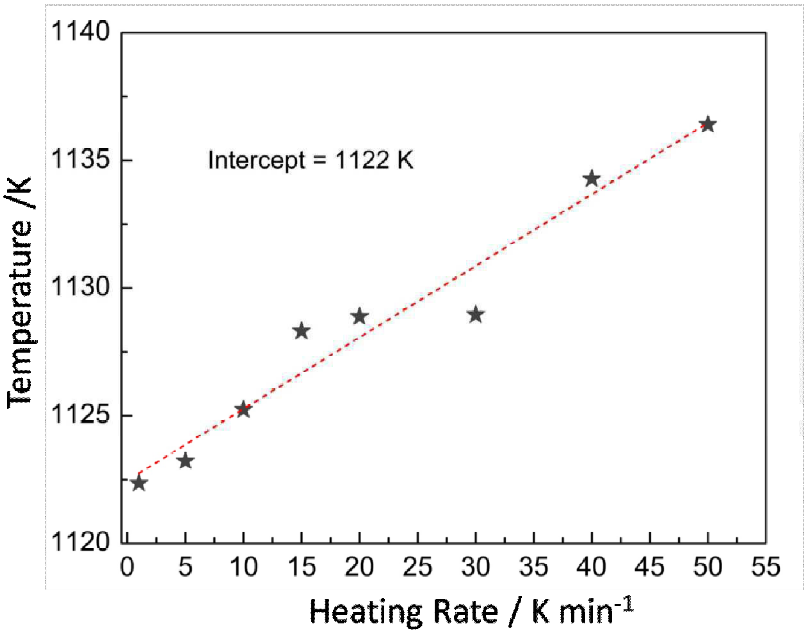

Fig. 5.7. Evaluation of pseudo equilibrium transition temperature of sigma (σ) to alpha (α) phase in $Fe_{54}Cr_{46}$ alloy

It is therefore clear that the increase in heating rate shifts the transformation to higher temperature which is quite understandable as the change in temperature is very rapid for the transformation to proceed by nucleation and growth process. The effect of variation in heating rate on the transformation temperature is shown in **Fig. 5.7**, which shows a nearly linear relationship. Therefore, the data was fitted linearly and extrapolated to zero K min^{-1} heating rate to obtain the near equlibrium transformation temperature. The equlibrium $\sigma \rightarrow \alpha$ phase transformation temperature measured in the present study is 849 ^{0}C (1122 K) as against the reported temperature of 820 ^{0}C (1093 K) by Xiong et al [85]. The measured equlibrium transformation temperature, is coploted in **Fig. 5.8** with the latest version of optimised sigma phase field along with the experimental data points of Fe-Cr phase diagram [85] which shows a difference of 29 K. Further, the kinetics of phase transformation has been modelled with non isothermal Kissinger and KJMA model.The details of kinetic modelling and analysis with a brief outline on the theoretical background is discussed in the next section.

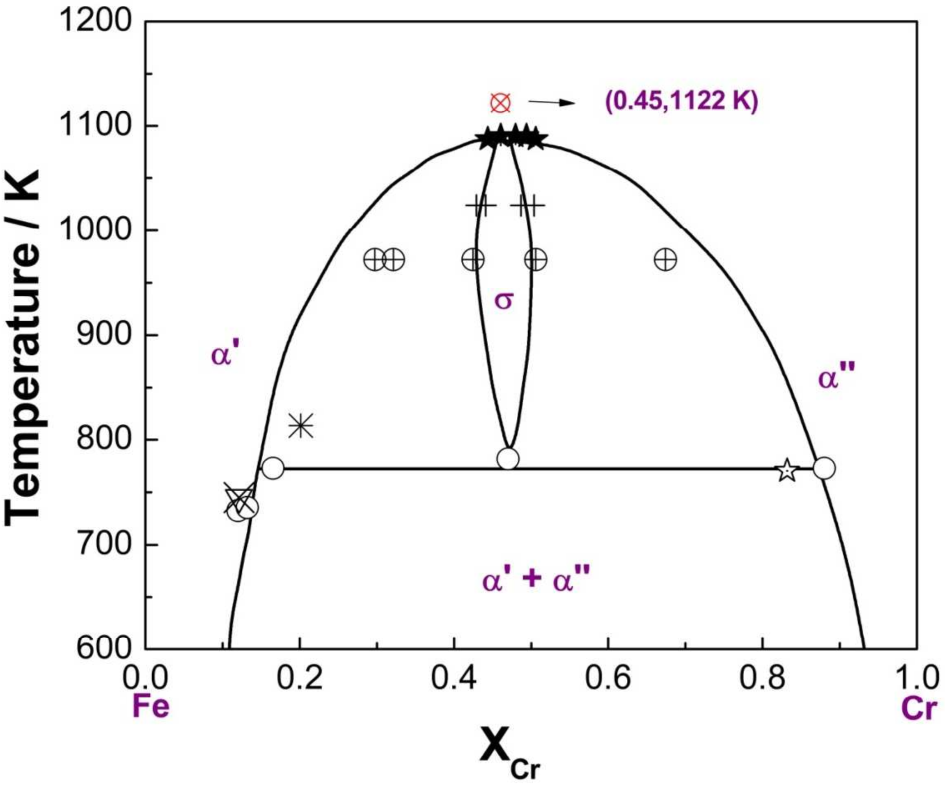

Fig. 5.8 Comparison of experimental upper temperature limit of sigma (σ) phase field with literature [85]

5.4. Theory of Non-isothermal Kissinger model:

Kissinger method [192] has been a widely used one to determine the activation energy [193-194] in the study of non-isothermal kinetics. The rate of transformation (d*x*/dt) under dynamic heating condition is a function of temperature dependent kinetic factors k(T) and fraction transformed f(*x*). This is applicable for non-isothermal transformation where the above two variables are separable [195] and can be written in following product form i.e.

$$C = dx/dt = k(T).\ f(x) \tag{5.1}$$

The kinetic factor k(T) exponentially depends on the temperature according to Arrhenius relation

$$k(T) = A \exp(-E_a / RT) \tag{5.2}$$

Where A is the pre-exponential factor, E_a is activation energy, R is the gas constant. Under constant heating rate (β) the rate equation has the following form

$$dx/dt = A / \beta \exp(-E_a / RT)\ f(x) \tag{5.3}$$

Kissinger model assumes that the rate of transformation is maximum at peak temperature T_p. Therefore, at peak temperature

$$dC / dx = 0 \tag{5.4}$$

Under this condition, the following form can be derived from Eq. (5.3)

$$d\ln(\beta/T_p^2) / d(1/T_p) = -E_a / RT \tag{5.5}$$

Eq. (5.5) can also be rearranged as

$$\ln(\beta/T_p^2) = \ln(E_a/R) - E_a / RT \tag{5.6}$$

Eq. (5.6) represents the well known Kissinger equation. It must be stated here that this equation is valid for first order phase transformations under constant heating rates. It can also be used for higher order kinetics provided the fraction transformed is independent of heating rate. In the present study, the variation of the quantity $\ln(\beta/T_p^2)$ with T_p^{-1} is shown in **Fig. 5.9**. Fairly linear relationship between $\ln(\beta/T_p^2)$ and $1/T_p$ is apparent from **Fig. 5.9**. The activation energy for σ → α phase transformation is estimated as 369.24 kJ/mole, which is found to be higher than the value estimated for the reverse transformation of α → σ phase [109-110].

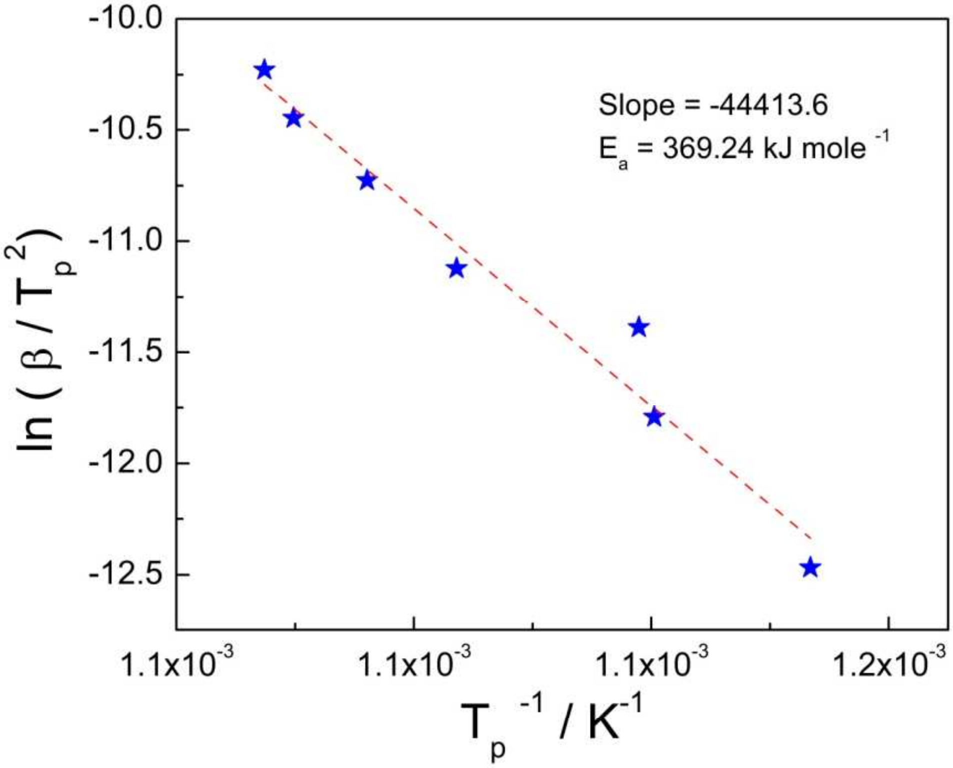

Fig. 5.9 Kissinger analysis of transformation kinetics of sigma (σ) to alpha(α) phase

5.5. Theory of non-isothermal KJMA model:

The Kolmogorov–Johnson–Mehl–Avrami (KJMA) model provides an analytical description of the kinetics of diffusive phase transformations. The KJMA model has been derived based on the three main aspects of diffusive phase transformation namely nucleation, growth and impingement effects. The nucleation process is assumed as either continuous nucleation where the rate of nucleation changes with temperature or site saturation when the growth process commences only after the completion of nucleation. The growth process has been considered as either diffusion controlled or interface controlled. It is required to mention here that although the KJMA model [196-198] has a number of limitations, it still provides an easy empirical formalism to obtain the kinetic parameters for diffusive transformation. The fraction transformed (*f*) in any diffusive solid state transformation under dynamic heating condition in DSC can be written as

$$f = \int_{Ts}^{T} \Phi(T)dT \Big/ \int_{Ts}^{Tf} \Phi(T)dT \qquad (5.7)$$

where T is the temperature and $\Phi(T)$ is the baseline corrected heat flow. The fraction transformed in an isothermal solid state transformation typically follows a sigmoidal behavior which can be modeled with the non-isothermal KJMA expression in the following form

$$f(T) = 1 - exp[k\ (R(T-T_s)^2 / \Phi\ Q_{eff})^n] \qquad (5.8)$$

$$k = k_0\ exp\ (-Q_{eff} / RT) \qquad (5.9)$$

where n represents order of the reaction or kinetic exponent, Q_{eff} is the activation energy associated with the transformation, k is the Arrhenius rate constant, T_s is the temperature of onset of transformation. It is not convenient way to estimate the activation energy by KJMA model because the three kinetics parameters in the above equation cannot be varied simultaneously to obtain the correct fit value. It is more convenient to get the activation energy from the Kissinger model and use it as input for the above expression to free float the other two parameters. The fraction transformed calculated by Eq. (5.7) for different heating rates is displayed in **Fig. 5.10.** It is seen that the fraction transformed curves shows a sigmoidal behavior which is fitted with the KJMA expression given in Eq. (5.8). **Figure 5.10** clearly reveals that the steepness of fraction transformation curve for the lower heating rates until 10K min^{-1} is different from those of the higher heating rates. It is apparent that heating rate not only influences the start temperature of σ → α phase transformation but also the transformation characteristics. The values obtained for rate and order parameters by fitting the fraction transformed data into KJMA model by Eq. (5.8) is given in Table 5.1.

5.6 Impact of σ phase on high temperature phase stability of α phase

Sigma phase formation in high Cr ferritic steels under service conditions at high temperature is a common feature which has a severe impact on the mechanical and physical properties like creep strength, tensile ductility and impact toughness.

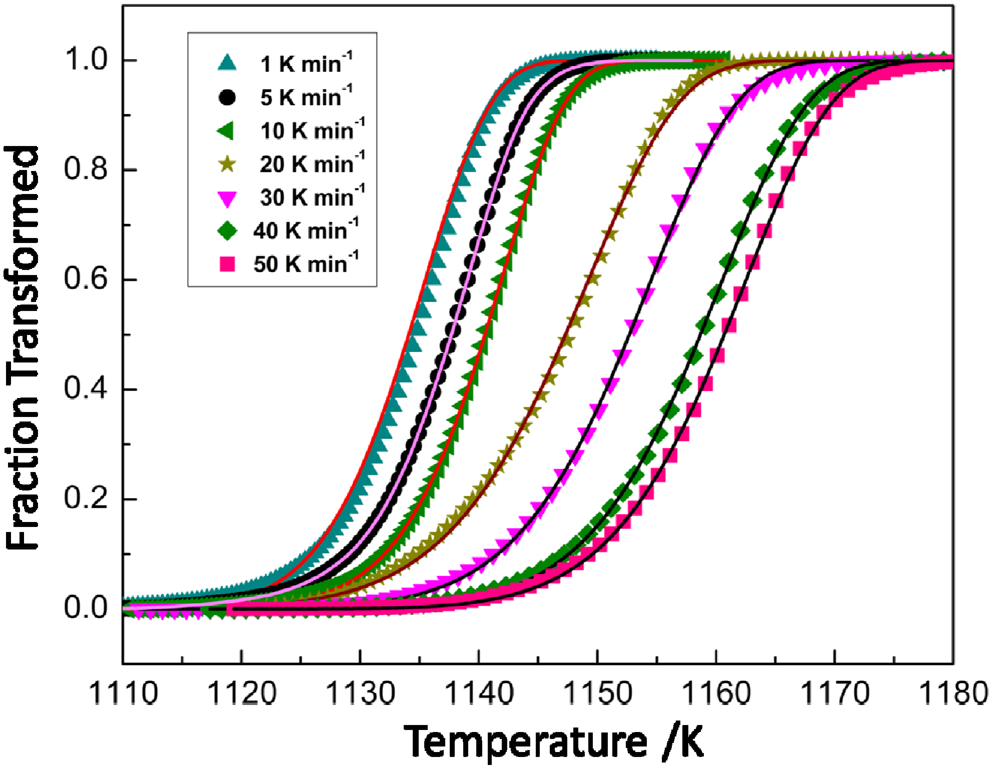

Fig. 5.10. KJMA analysis of kinetics of sigma (σ) to alpha (α) phase transformation

The formation of sigma phase in ferritic steel at high temperature arises from the complex interaction of Fe and Cr atoms under severe stress condition. Although, a wealth of literature is available on the physical metallurgy of sigma phase of Fe - Cr and related systems, a calorimetry based extensive characterization of high temperature phase stability and phase transformation kinetics in a wide temperature range of 100 to 1100 ^{0}C (373 to 1373 K) is not available to the best of my knowledge. Moreover, the sigma phase field of Fe - Cr system was optimized [85] despite experimental ambiguities. It is reiterated here that the sluggish kinetics of sigma formation from alpha forbids its study by dynamic phase identification techniques; however, the reverse kinetics of sigma decomposition to alpha is fast enough to study by dynamic techniques.

Table 5.1.
Results of KJMA analysis

Heating Rate (β) (K min^{-1})	n	Q_{eff} (kJ mole^{-1})	K
1	2.52	263.51	2.15 X 10^{12}
5	2.63	255.34	2.89 X 10^{12}
10	2.87	235.07	4.42 X 10^{11}
20	2.30	253.96	1.75 X 10^{11}
30	2.18	254.26	2.25 X 10^{11}
40	2.27	244.65	3.20 X 10^{11}
50	2.21	248.19	2.97 X 10^{12}

This has provided an impetus to carry out an extensive calorimetric characterization study to obtain better clarity on the ambiguous events in the sigma phase field of Fe-Cr system. Towards this goal, sigma phase was synthesized from parent alpha phase by heat treatment of prior cold rolled sample in vacuum. XRD and metallographic characterization revealed that bcc alpha phase was completely converted to tetragonal sigma phase after heat treatment. The complex structural conversion of bcc to tetragonal basically results in contraction in unit cell which leads to the formation of micro cracks in sigma microstructure (**Fig. 5.2(a)**). This is responsible for the extremely brittle nature of the sigma phase. Differential Scanning calorimetry study revealed completely different characteristics for alpha and sigma phases at high temperature. The alpha phase alloy shows only one transformation until melting, which corresponds to the ferro - para magnetic transition at 558 ^{0}C (831 K). The alpha to sigma phase transformation could not be detected in alpha phase sample which is attributed to the slow kinetics (**Fig. 5.3**). This aspect was confirmed by repeat experiments. In contrast, the first DSC run of sigma phase revealed a phase transformation at 852 ^{0}C (1125 K) during heating although the reverse transformation was not observed during cooling (**Fig. 5.4**). This corresponds to the sigma to alpha transformation at 852 ^{0}C (1125 K). The repeat second experiment with the same DSC run sample showed a completely different behavior compared to the first run (**Fig. 5.5**) and was identical to the behavior of alpha phase. From the above studies it is confirmed that once the sigma phase decomposed to alpha, it does not form during cooling and requires further prolonged heat treatment to reappear. This has great significance in high Cr ferritic steel where sigma phase formation issue can be completely avoided by suitable heat treatments above the sigma decomposition temperature.

Further, it was observed that the measured sigma decomposition temperature of 852 ^{0}C (1125 K) is 32 K higher than the accepted upper temperature limit of 820 ^{0}C (1093 K) [85] of sigma phase field for Fe-Cr binary system in the latest reported Fe-Cr phase diagram. This can be understood in the light of experimental discrepancies on the sigma decomposition temperature range reported in literature [85]. In a recent Mossbauer study, the isothermal transformation kinetics of sigma to alpha phase transformation has been presented by Mikikits-Leitner et. al [145]. Interestingly, the authors assume the accepted temperature of 821 ^{0}C (1094 K) in the Fe-Cr phase diagram for $\sigma \rightarrow \alpha$ transformation and ex situ Mossbauer investigation was carried out above 821 ^{0}C (1094 K) at five different temperatures in the range of 827 - 847 ^{0}C (1100 K - 1120 K). Isothermal study of phase transformation kinetics above transition temperature is only feasible if the kinetics is extremely sluggish. Best examples of this is alpha to sigma phase transformation at around 500-510 ^{0}C (773-783 K). The restructuring of bcc alpha phase into complex tetragonal has resulted in extremely sluggish kinetics. Secondly, the temperature is not high enough for fast diffusion which enables the study of isothermal kinetics above transition for alpha to sigma transformation. The DSC thermogram of alpha phase at slow heating rate of 1 K min^{-1} also supports the above fact. In contrast, sigma to alpha transformation was observed even with moderately high heating rate of 50 K min $^{-1}$. Therefore, it is concluded that the isothermal experiments above transition temperature for $\sigma \rightarrow \alpha$ transformation is not possible, while it can be carried out close to the transition temperature from lower side. This also suggests that the transition temperature for $\sigma \rightarrow \alpha$ transformation is different from 820 ^{0}C (1093 K) as reported in the latest Fe-Cr diagram. In order to determine the pseudo equilibrium sigma decomposition temperature, the effect of heating rate on the decomposition temperature of sigma phase was studied with various heating rates in the range of 1 – 50 K min^{-1}. The result of this study is shown in **Fig. 5.7**. The intercept of the fitted line appears at 849 ^{0}C (1122 K) which is being co plotted in **Fig. 5.8** with the recent optimized sigma phase field of Fe Cr phase diagram proposed by Xiong et al [85]. This calls for the further optimization of sigma phase field in Fe–Cr phase diagram.

5.7 Conclusion

The present study provides new insights into the high temperature phase stability and phase transformation kinetics of sigma and alpha phases in $Fe_{54}Cr_{46}$ alloy. Following are the important conclusions drawn from the present study.

- The alpha (α) to sigma (σ) phase transformation could not be studied by dynamic calorimetry due to its extremely sluggish nature while the reverse kinetics of sigma(σ) to alpha (α) can be precisely attested by dynamic calorimetry.
- The upper limit of sigma phase field is measured as ~ 1122 K which is about 30 K higher than the presently accepted sigma decomposition temperature in Fe-Cr phase diagram.
- The activation energy for sigma to alpha phase transformation is estimated to be ~250 kJ mole^{-1} by nonisothermal KJMA analysis.

- Sigma phase formation in high Cr ferritic steel can be avoided by heat treatment above the sigma decomposition temperature since this phase immediately dissolves into alpha above the transition temperature and its reappearance is an extremely slow process.

Chapter 6

High temperature thermo-physical and heat transport properties of sigma (σ) and alpha (α) phases

6.1 Introduction

Steels of different grades and product forms are most sought after in various industries owing to their favourable mechanical, physical and corrosion properties and radiation resistance. Choice of a structural steel is always driven by the operating environment. However, the evolution of its microstructure, local chemistry and related properties in response to external variables while in service like for example the formation of deleterious TCP (topologically close packed) phases is a cause for concern. Among the various embrittling phases reported to form in steels like Laves, χ, Z phase and carbides [6], the mechanism and kinetics of formation of sigma (σ) phase is well studied. Many in-service failures were reported due to σ-phase formation. Chastell and Flewitt [117] in the year 1979 reported the premature failure of 316 SS secondary super heater boiler tube due to enhanced creep cavitation associated with σ formation. ER 309L SS welds containing δ-ferrite exhibited 85% reduction in toughness after ageing at 700 °C (973 K) for 2 h, due to $\delta \rightarrow \sigma$ transformation [118]. Prolonged heating at temperatures greater than 650 °C (923 K), embrittled austenitic stainless steel weld joints due to σ formation [119]. Accelerated ageing of Gas Tungsten Arc Welds of 316FR SS also lead to the nucleation of σ at δ/γ interphase boundary which was predicted to affect the repair weldability of the steel [120]. In FeCr binary, σ is a stable equilibrium phase which exists at high temperature and can be stable upto 77 GPa and had low compressibility than both the constituent elements [85]. Cieslak et al. [107,199] reported the σ phase to be weakly ferromagnetic at temperatures lower than 46 K (-227 °C) and its magnetism to be eight times weaker than that of the α phase. Malinsky and Claisse in 1973 [138] measured the heat capacity of α phase in $Cr_{0.47}Fe_{0.53}$ alloy in the temperature range of 554-1154 °C (827-1427 K) and Downie and Martin [34] measured Cp, enthalpy and entropy of formation for both α and σ phases in $Fe_{0.53}Cr_{0.47}$ and $Fe_{0.566}Cr_{0.434}$

alloys by dynamic calorimeter. A similar study on the estimation of thermal conductivity of individual phases in Fe-Cr system is not available to the best of our knowledge. Therefore, objective of the present work is to measure both thermo-physical and heat transport properties for both parent α and σ phases in a $Fe_{54}Cr_{46}$ (at.%) alloy and thereby gain a comprehensive understanding of the difference in behavior between the two phases. Synthesis and characterization of sigma phase has already been discussed in **Chapter 5** in detail. The same parent and product phase of alpha and sigma phase is being used in this study.

6.2. Enthalpy measurements by Calorimetry

The drop calorimeter measured enthalpy increment curve as function of temperature for alpha and sigma phase is shown in **Fig. 6.1.** It is observed that the enthalpy curve has an increasing trend with temperature. There is no phase transformation observed upto 1327 ^{0}C (1600 K). However, a slope change is observed around 547 ^{0}C (820 K) for α phase which corresponds to the magnetic phase transformation of $\alpha_{ferro} \rightarrow \alpha_{para.}$ **Figure 6.1** shows an increase in the enthalpy of sigma phase without any phase transformation upto 827 ^{0}C (1100 K), beyond which a distinct jump in enthalpy is observed at ~ 837 ^{0}C (1110 K) which corresponds to the structural phase transformation of tetragonal sigma to bcc alpha phase. The enthalpy associated with this phase transformation is measured as ~ 2.6 kJ mole^{-1}. There is no change in slope observed for the enthalpy curve of sigma phase. The difference in enthalpy of α and σ phase of $Fe_{56}Cr_{44}$ alloy is distinctly observed in **Fig. 6.1**. This is attributed to the difference in the Debye temperatures for the two structures depending on the nature of bonding. The study of high temperature phase transformation characteristics and specific heat measurements of both alpha and sigma phase was carried out by differential scanning calorimeter and the results are displayed in **Fig. 6.2** (a) and (b) respectively.

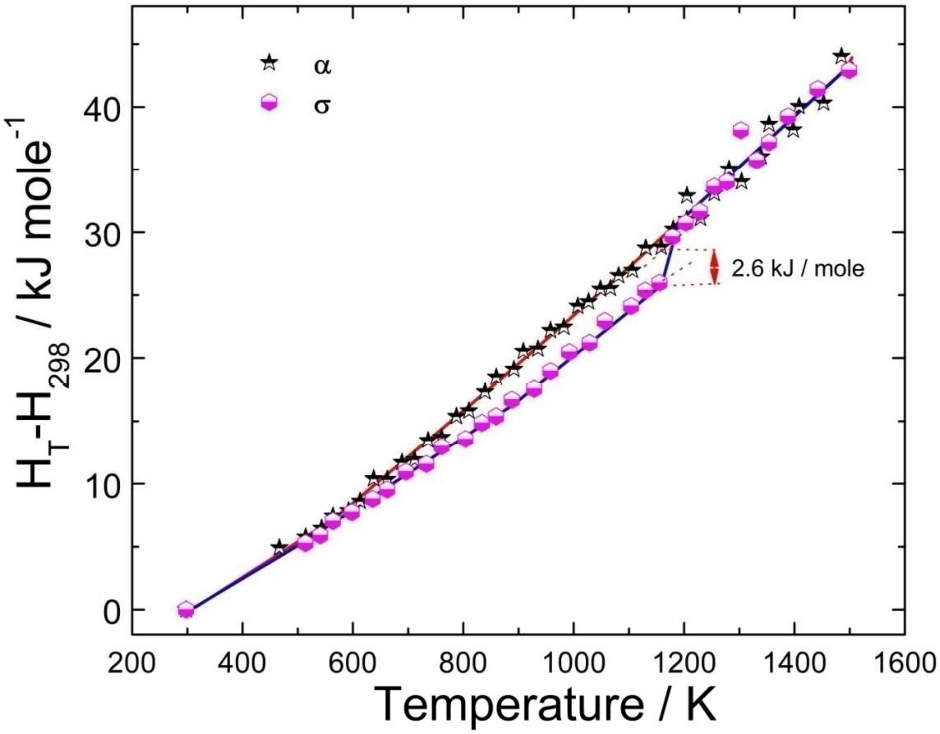

Fig. 6.1 Enthalpy increment measurements for α and σ phase by drop calorimetry

It is observed that alpha phase does not undergo any structural phase transformation other than magnetic transformation at 548 ^{0}C (821 K) which was also observed in the enthalpy curve obtained by drop calorimetry. This confirms the Curie temperature of alpha phase as 548 ^{0}C (821 K). The heat flow profile for sigma phase provides evidence for the structural phase transformation of sigma to alpha which is in line with the results of drop calorimetry at 847 ^{0}C (1120 K). The specific heat of both alpha and sigma phase was measured by both drop and differential scanning calorimetry and the results are discussed in the next section.

6.3. Evaluation of specific heat from enthalpy data

The enthalpy data generally fitted with standard Mayer Kelly expression given by Eq. (6.1). The enthalpy data in the present study is treated with modified Mayer Kelly expression given in Eq. (6.2) to experimentally obtain the specific heat for both the alloys.

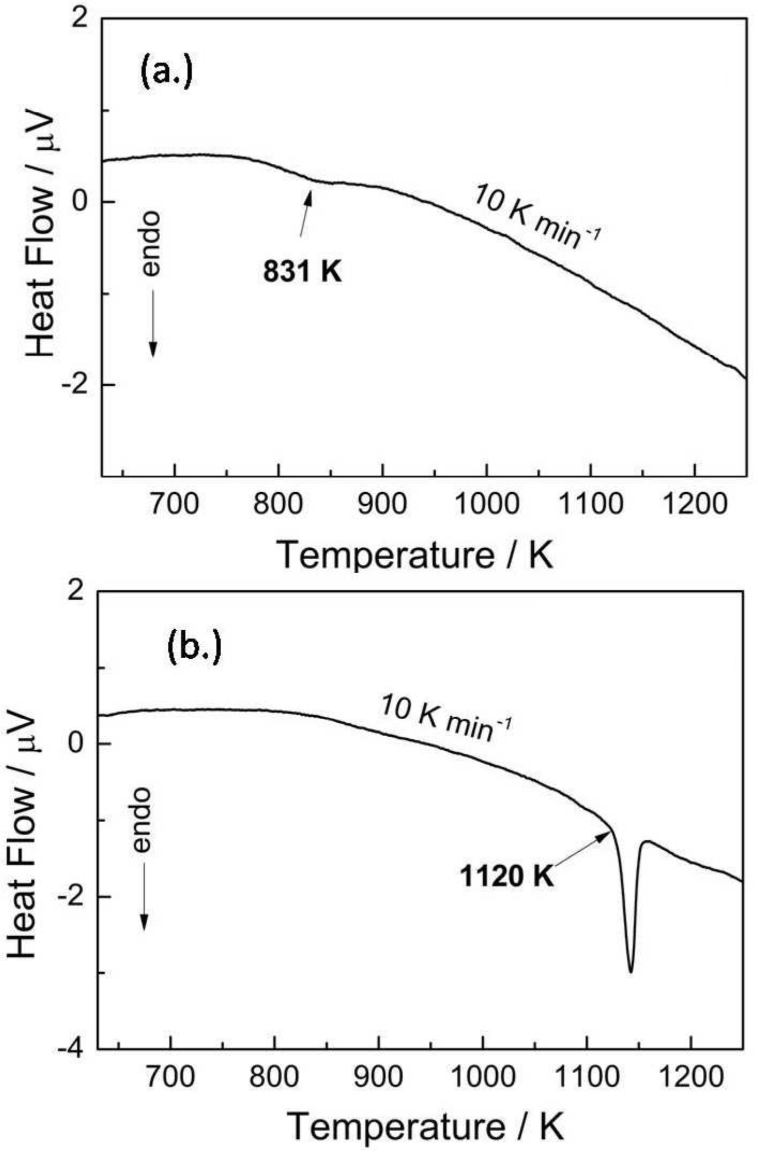

Fig. 6.2 DSC heat flow diagram for (a) α phase and (b) σ phase at 10 K min^{-1} heating and cooling rates

$$H_{T-298} = P_1 + P_2\,T + P_3\,T^{2} + P_4 / T \qquad (6.1)$$

Where P_1, P_2, P_3 and P_4 are the fit constants obtained by fitting. Since alpha phase is associated with a magnetic phase transformation at 537 ^{0}C (810 K), the standard Mayer Kelly expression is modified with a magnetic enthalpy term from Hillert – Jarl model (97) in order to get the experimental magnetic specific heat.

$$H_{T-298} = P_1 + P_2\,T + P_3\,T^{2} + P_4 / T + \Delta H_{mag} \qquad (6.2)$$

$$\Delta H_{mag} = \ln(\beta+1)\,h(\tau). \qquad (6.3)$$

$h(\tau) = [(-79\,\tau^{-1}/140p)+(474/497)(1/p-1)(2\,\tau^{3}+2\tau^{9}/3+2\tau^{15}/5)]/D$, for $\tau =(T/T_c) \leq 1$ [6.3.a]

$h(\tau) = -(\tau^{-5}/2+\tau^{-15}/21+\tau^{-25}/60)/D$, for $\tau =(T/T_c) \geq 1$ (6.3.b)

where β is the average magnetic moment per atom in Bohr magnetron unit which can be measured experimentally, 'p' is a structure dependent parameter. For simple bcc phase 'p' has value of 0.4 with an associated value of D = 1.55828482 [182] whereas for other common phases 'p' has the value of 0.28 with D = 2.342456517. The experimental enthalpy data for alpha phase alloy was fitted by Eq. (6.2) after reducing the magnetic enthalpy. Sigma phase being nonmagnetic, enthalpy associated with magnetism is zero. Hence, the experimental enthalpy is fitted by simple Mayer Kelly expression in Eq. (6.1). The enthalpy data for sigma phase was fitted until 837 ^{0}C (1110 K) before the transformation of sigma to alpha phase. The fit coefficient for alpha phase is given below.

P_1/J mol^{-1}	=	-5403.8 ± 250.23;
P_2/J mol^{-1} K^{-1}	=	16.03 ± 0;
P_3/J mol^{-1} K^{-2}	=	0.00895 ± 0.0007;
P_4/J mol^{-1} K	=	151265 ± 1834.2;
R^2 (fit)	=	0.98.

The fit coefficients for nonmagnetic sigma phase have the value of

P_1/J mol^{-1}	=	-13503.6 ± 729
P_2/J mol^{-1} K^{-1}	=	27.1 ± 0;
P_3/ J mol^{-1} K^{-2}	=	0.00726 ± 0.001
P_4/ J mol^{-1} K	=	707320 ± 8365.12;
R^2 (fit)	=	0.97.

The experimental specific heat for both the alloys was calculated by using P2, P3 and P4 fit parameters which are shown in **Fig. 6.3** along with the specific heat measured by differential scanning calorimetry and available literature data [34]. The specific heat for sigma phase measured by drop and dynamic calorimetry is compared with literature and specific heat of alpha phase in **Fig. 6.3.**

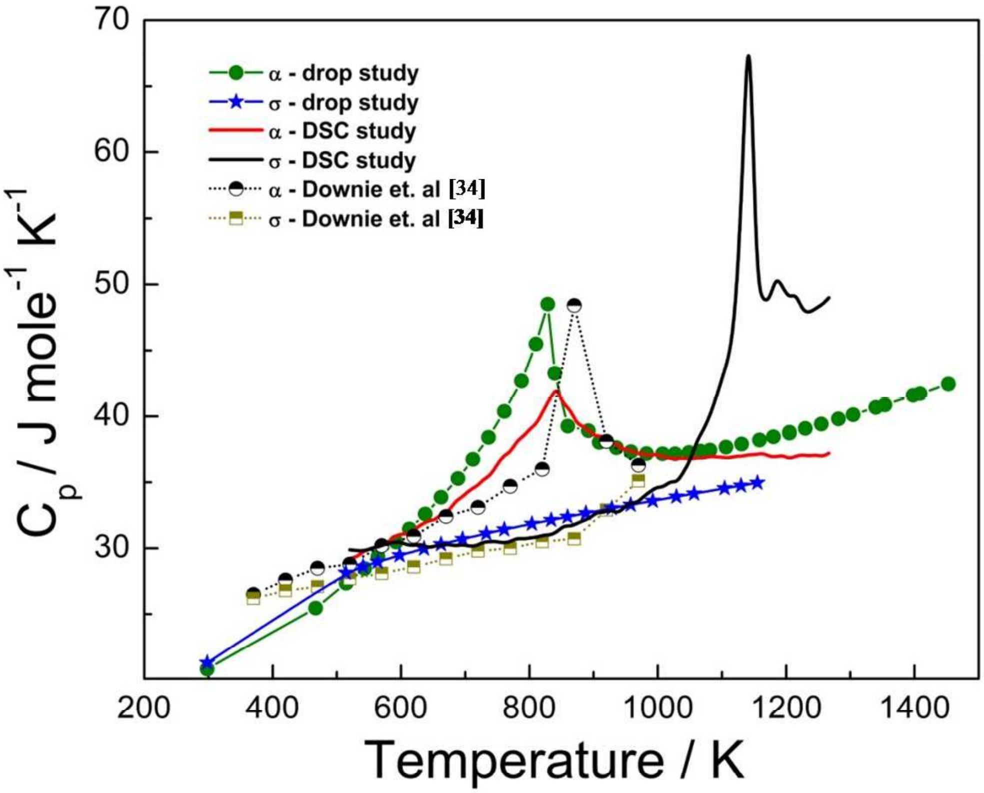

Fig. 6.3 Comparison of experimental specific heat values obtained by drop and DSC for α and σ phases with literature data

The difference in specific heats for sigma and alpha phases are readily apparent from **Fig. 6.3**. It is observed that the specific heat for alpha phase measured by static and dynamic method is in good agreement and also fairly in agreement with available literature [34]. However, specific heat at T_c has different values for static and dynamic mode of measurements. The results in the present study are also in good agreement with available literature until 727 ^{0}C (1000 K). However, the specific heat measured by DSC for sigma phase shows a deviation beyond 727 ^{0}C (1000 K) as it approaches the phase transformation regime. A similar trend is also reported in literature by Downey et al [34] beyond 577 ^{0}C (850 K). Therefore, this phase transformation region was ignored in the specific heat data obtained from DSC.

6.4 Evaluation of thermal expansion properties by dilatometry

Temperature dependent linear thermal expansion was measured by thermomechanical analyser for both alpha and sigma phases and uncorrected data is depicted in **Fig. 6.4**.

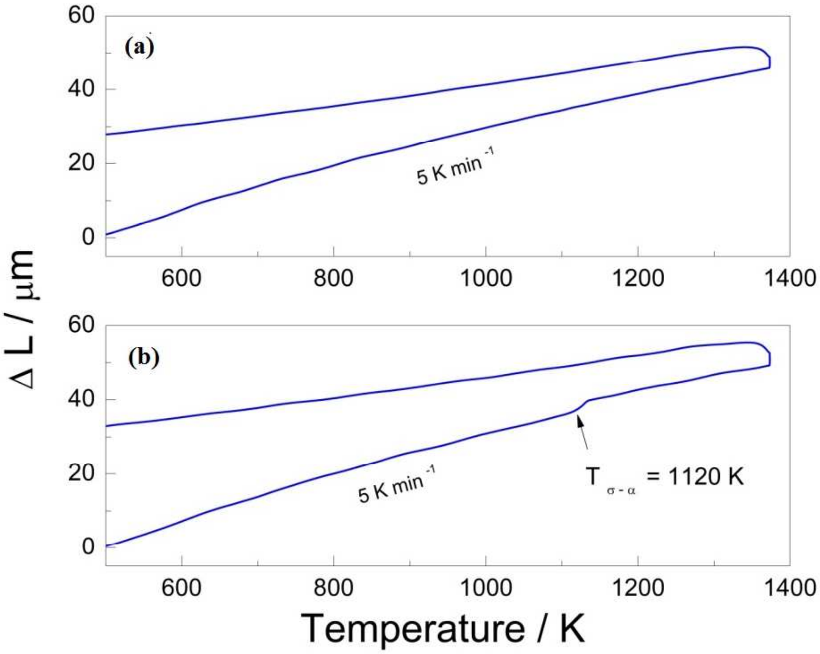

Fig. 6.4 TMA profile for **(a)** α and **(b)** σ phases

It is observed from **Fig. 6.4 (a)** that the alpha phase is linearly expanded with temperature with no evidence for any phase transformation until 1127 ^{0}C (1400 K). However, a clear inflection is observed at 847 ^{0}C (1120 K) for sigma phase in **Fig. 6.4 (b)** , which is associated with the sigma to alpha phase transformation as observed in DSC and drop results. As can be seen in **Fig. 6.4 (a)** the magnetic transformation is apparently not attested. However, the corrected TMA curve for alpha phase in **Fig. 6.5 (a)** clearly shows the magnetic transformation is attested by a small contraction at around 547 ^{0}C (820 K). In order to measure the thermal expansion coefficient, the corrected TMA curve was fitted with simple nonlinear second order equation of following form.

$$Y = a + b\,T + c\,T^2 \qquad (6.4)$$

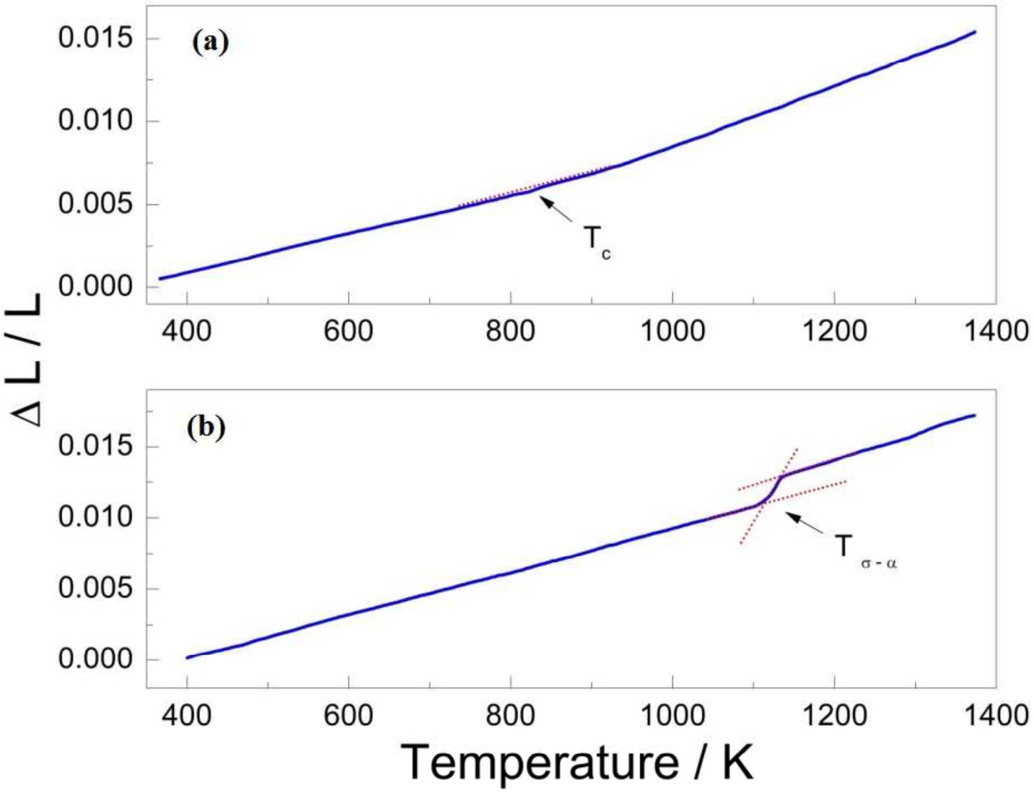

Fig. 6.5 Corrected TMA heating profile for **(a)** α and **(b)** σ phase

The fit coefficients for alpha phase are a = -0.00154, b = 4.12 x 10^{-6} and c = 5.99 x 10^{-9}. The room temperature thermal expansion coefficient for alpha phase is 7.39 x 10^{-6} K^{-1}. TMA curve for sigma phase was fitted until 847 ^{0}C (1120 K) before the sigma to alpha phase transformation. The fit coefficients for sigma phase are a = -0.00586, b = 1.4929 x 10^{-5}, c = 1.76633 x 10^{-10} K^{-1}. The room temperature thermal coefficient for sigma phase is 1.5 x 10^{-5} which is much higher than for alpha phase of same composition.

6.5. Thermal Diffusivity and thermal conductivity results

A snapshot of laser pulse for alpha and sigma phase as obtained from Laser flash thermal diffusivity analyzer (LFA) is shown in **Fig. 6.6 and 6.7** respectively. It is observed from **Fig. 6.6 and 6.7** that the room temperature thermal diffusivity of alpha and sigma phase is 0.0484 cm^2s^{-1} and 0.011 cm^2s^{-1} respectively. The thermal diffusivity for alpha phase is much higher than that of sigma phase. The temperature dependent thermal diffusivity in the range of 25 - 1127 ^{0}C (273-1400 K) for alpha and sigma phases of $Fe_{54}Cr_{46}$ alloy are shown in **Fig. 6.8**.

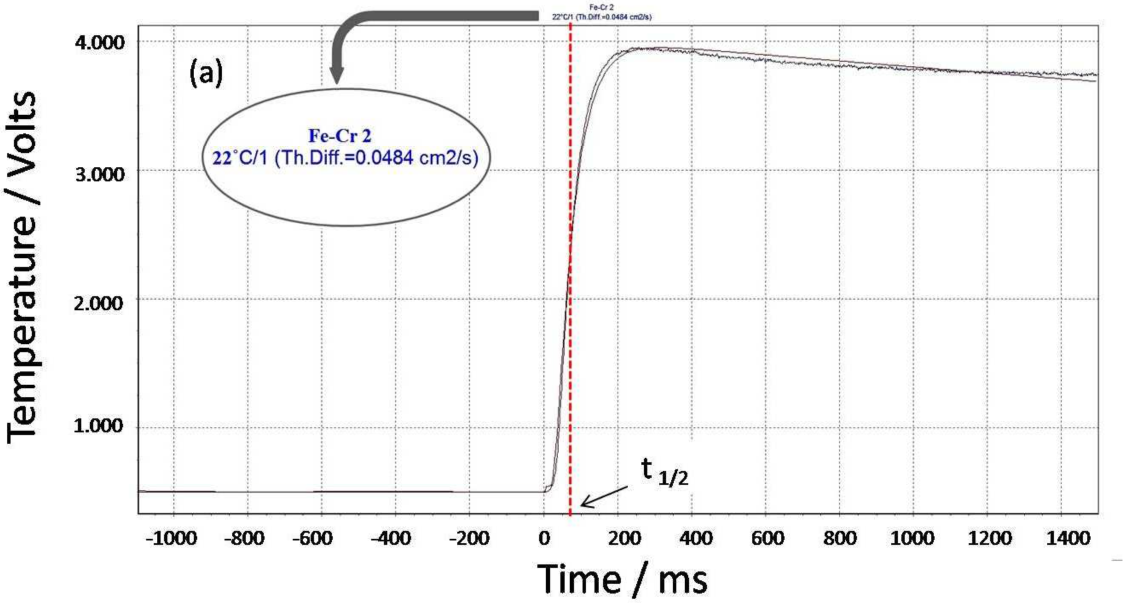

Fig. 6.6 Snapshot of temperature Vs. time diagram as obtained by LFA for α phase

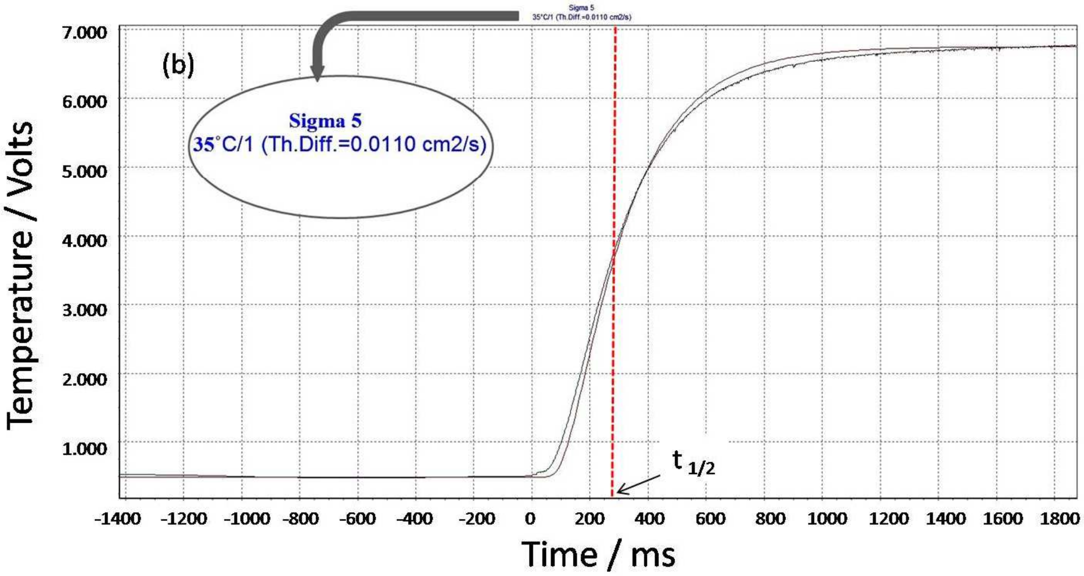

Fig. 6.7 Snapshot of temperature Vs. time diagram as obtained by LFA for σ phase

The effect of magnetism is clearly manifested for alpha phase in thermal diffusivity data which initially showed a decreasing trend with temperature until the magnetic transformation followed by an increase with increasing temperature. However, thermal diffusivity for sigma phase shows a monotonic increase with increasing temperature. The experimental thermal conductivity for alpha and sigma phase is compared with available literature [200-201] for high Cr steel in **Fig. 6.9**. The thermal conductivity of alpha and sigma phase is 16.9 and 3.9 W m^{-1} K^{-1} respectively which clearly establishes the detrimental effect of sigma formation on the thermal conductivity of any structural material. The experimental room temperature thermal conductivity of alpha phase is in good agreement with the reported data of Abiko et. al [200] and it resides within the thermal conductivity range of high Cr steel [201]. It increases with temperature as observed for other steels and the magnetic transformation is clearly manifested in the conductivity data. A similar trend is observed for 18Cr steel in **Fig. 6.9**. It is necessary to mention here that the thermal conductivity of sigma phase is not reported in literature until date to the best of our knowledge. **Figure 6.9** also shows that the thermal conductivity of sigma phase increases with temperature.

6.6 Modeling of thermodynamic parameters

Thermodynamic parameters of solids can be analytically estimated through suitable equation of state (EoS) by using the available EoS parameters. Enthalpy, the experimentally measurable parameter primarily depends on the vibrational degree of freedom which arises from the volume expansion as a consequence of lattice vibration. Although, the vibrational degrees of freedom account for the major part of enthalpy, the magnetic spin disordering and kinetics of conducting electrons also have sizable contributions. Therefore, the temperature dependent enthalpy of a solid material is the combination of three distinct contributions; lattice vibration, magnetic and electronic. The total enthalpy of a magnetic material can be defined as

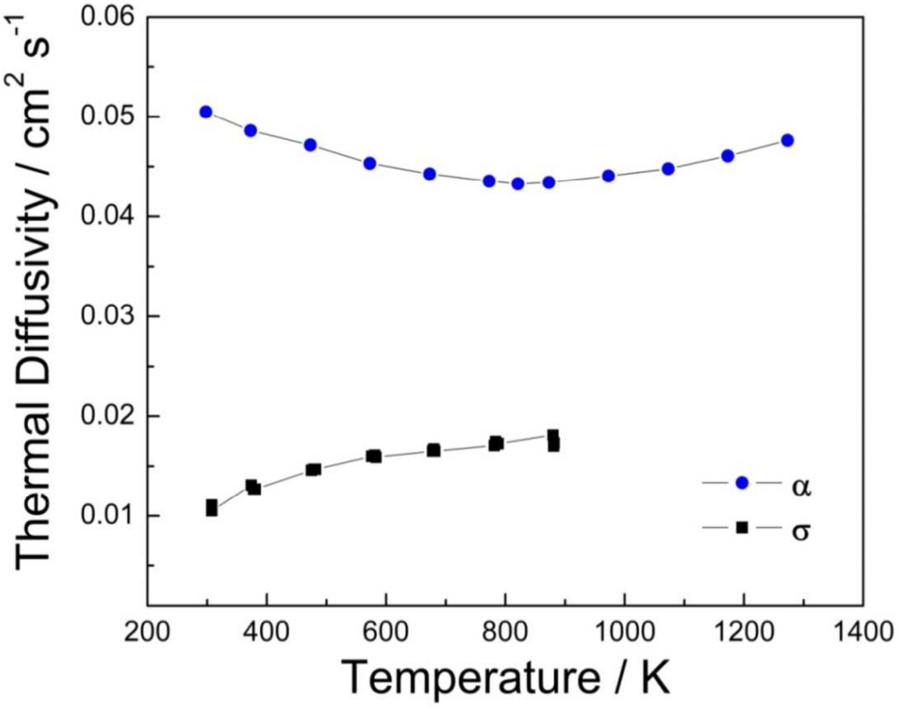

Fig. 6.8 LFA measured temperature dependent thermal diffusivity for α and σ phases

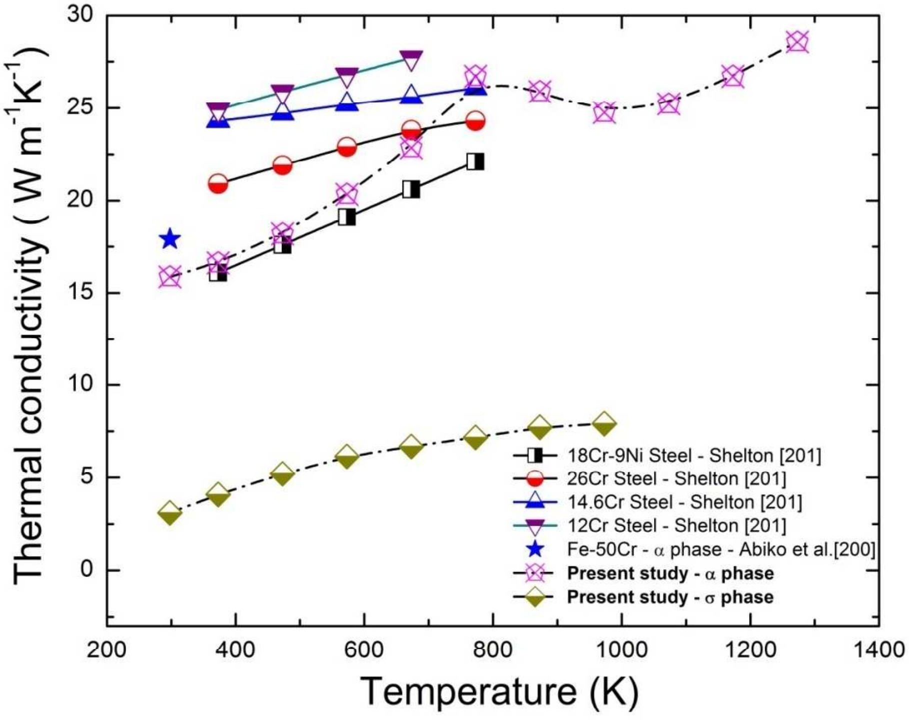

Fig. 6.9 LFA measured temperature dependent thermal conductivity of α and σ phases are co-plotted with available literature for high Cr steel

$$H(T) = E_0 + E_{vib}(T) + E_{mag}(T) + E_{elc}(T) + P \times V(T) \tag{6.5}$$

where E_o, E_{vib}, E_{mag} and E_{elc} are the zero kelvin energy, harmonic vibration, magnetic and electronic energy respectively. *P X V(T)* term represents the anharmonic contribution which is not being incorporated in the harmonic estimation of E_{vib}. Zero kelvin energy can be obtained by ab initio based first principle calculation. Suitable equation of state (Birch - Murnahan equation) is used to fit and obtain the zero Kelvin energy. Another way to obtain zero kelvin energy is to fit the experimental pressure vs volume (P vs V) data by an appropriate equation of state.

6.6.1 Estimation of harmonic lattice vibration (E_{vib})

The major contribution to enthalpy arises from atomic vibration. Harmonic contribution to enthalpy (E_{vib}) can be calculated by Debye model where the frequency of vibration is assumed to be independent of volume and temperature. Therefore, E_{vib} can be approximated from phonon frequency alone considering there will be no phonon-phonon interaction by the following expression

$$E_{vib} = 9NK_B T({T}/{\theta_D})\int_0^{\theta_D} D\{{X^3}/{(e^X - 1)}\} \tag{6.6}$$

In the above expression, $X = \theta_D / T$ and θ_D is the Debye temperature. This model successfully approximates at low temperature region rather than at high temperatures, because of its nonanalytical integral form. In the present calculation, Nernst–Lindeman model is used for estimation of E_{vib} under harmonic approximation because of its simple analytical nature and successful interpolation to the high temperature limits of Debye integral approximation [183-184]. The details of Nernst–Lindeman model can be found elsewhere [38] in the following form

$$E_{vib} = 0.75 pR\theta[\{{2}/{(e^{\theta/T} - 1)}\} + \{{1}/{(e^{\theta/2T} - 1)}\}] \tag{6.7}$$

where p stands for number of atoms per formula unit and $\theta = 0.77\ \theta_D$ and R has a value of 8.314 J mol^{-1} K^{-1}. Debye temperature (θ_D) for α - $Fe_{56}Cr_{44}$ alloy is reported as 430 K by Downie et. al [34] which has been used in present study for the calculations.

6.6.2. Anharmonic contribution estimated by Debye – Gruneisen formalism

The estimation of vibrational enthalpy in the above section by Nernst–Lindeman model does not incorporate true anharmonicity. It has calculated the vibrational enthalpy considering as harmonic oscillator. Debye – Gruneisen quasi harmonic formalism has been employed for estimation of temperature dependent anharmonicity in terms of volume expansion. The volume dependence of vibrational frequency is correlated through Grüneisen parameter (γ_G). Basically, γ_G relates thermal properties with elastic properties of materials [183-184], which can be defined as

$$\gamma_G = -\frac{d\ln\omega}{d\ln V} = -\frac{d\ln\theta_D}{d\ln V} \tag{6.8}$$

In the above expression ω is frequency of lattice vibration, θ_D is Debye temperature and V is molar volume of solid. Further Grüneisen parameter can also be expressed in terms of experimentally measurable parameter which can be given as

$$\gamma_G = \alpha_V B_T V / C_v \tag{6.9}$$

Where, α_V is the volume thermal expansion, B_T is the isothermal bulk modulus and C_v is specific heat at constant volume. Further, Grüneisen parameter (γ_G) can be correlated with pressure derivative of isothermal bulk modulus ($B_T^{'}$) by Slater's formula which can be written as

$$\gamma_G = 0.5(B_T^{'}) - 1/6 \tag{6.10}$$

More details on Debye-Grüneisen quasi-harmonic formalism is available in the recent monograph of Anderson [184]. The basic Debye-Grüneisen thermal equation of state can be expressed in the following manner

$$V_T = V_0\{[E_{vib}/(Q_0 - rE_{vib})] + 1\} \qquad (6.11)$$

Where $Q_0 = B_T V_0 / \gamma$ and $r = (B_T^{'} - 1)/2$, V_0 is the volume, B_T is isothermal bulk modulus and $B_T^{'}$ is the isothermal pressure derivative of bulk modulus at 298.15 K [34].

6.6.3. Effect of magnetism

Magnetism has a strong effect on the phase stability and thermo physical properties of magnetic alloys. The effect of magnetism to the phase stability has been elaborated by Inden through his empirical model [96-97] which has been widely accepted for elucidating magnetic effect on phase stability. Inden has expressed the complex behavior of magnetic specific heat with a logarithmic singularity at the critical transformation temperature which has the following form

$$C_p^{FM} = K^{FM} R \ln\left((1+\tau^3) / (1-\tau^3) \right) \qquad \text{for } \tau = T/T_c < 1 \qquad (6.12)$$

$$C_p^{FM} = K^{PM} R \ln\left((1+\tau^3) / (1-\tau^3) \right) \qquad \text{for } \tau = T/T_c > 1 \qquad (6.13)$$

where R is the gas constant, Tc represents Curie temperature and K^{FM}, K^{PM} are the two empirical constants for ferromagnetic and paramagnetic state.

However, derivation of magnetic Gibbs energy or magnetic entropy from the above expression is tedious. Hillert and Jarl [97] have simplified the Inden's expression for specific heat with expanded power series form, which is as follows

$$C_p^{FM} = 2K^{FM} R \ln\left(\tau^3 + \tau^9/3 + \tau^{15}/5\right) \qquad \text{for } \tau = T/T_c < 1 \qquad (6.14)$$

$$C_p^{FM} = 2K^{PM} R \ln\left(\tau^{-5} + \tau^{-15}/3 + \tau^{-25}/5\right) \qquad \text{for } \tau = T/T_c > 1 \qquad (6.15)$$

By integrating the above expressions, a simple expression for magnetic enthalpy (E_{mag}) can be written in the following form,

$$E_{mag} = 2K^{FM}T_cR[0.25\tau^4 + 0.033\tau^{10} + 0.0125\tau^{16}] \quad \text{for } \tau = T/T_c < 1 \qquad (6.16)$$

$$E_{mag} = -2K^{PM}T_cR[0.25\tau^{-4} + 0.023\tau^{-14} + 0.0083\tau^{-24}] \quad \text{for } \tau = T/T_c > 1 \qquad (6.17)$$

However, magnetic enthalpy can further be expressed in a very simple analytical manner [182] which has the following form (6.18)

$$E_{mag} \quad = \quad \ln(\beta + 1) \times h(\tau) \qquad (6.18)$$

$$h(\tau) = \frac{1}{D}\left[-\frac{79\tau^{-1}}{140p} + \frac{474}{497}\left(\frac{1}{p} - 1\right)\left(2\tau^3 + \frac{2\tau^9}{3} + \frac{2\tau^{15}}{5}\right)\right] \quad for \quad \tau < 1 \qquad (6.18a)$$

$$h(\tau) \quad = \quad -\frac{1}{D}\left(\frac{\tau^{-5}}{2} + \frac{\tau^{-15}}{21} + \frac{\tau^{-25}}{60}\right) \quad for \quad \tau \geq 1 \qquad (6.18b)$$

where β is the average magnetic moment per atom in Bohr magnetron unit which can be measured experimentally; ‘p’ is a structure dependent parameter which basically characterizes the fraction of magnetic enthalpy absorbed above T_c. For simple bcc phase ‘p’ has value of 0.4 with an associated value for D = 1.55828482 [182], whereas for other common phases ‘p’ has the value of 0.28 with D = 2.342456517. The above expression has been employed in present study for calculation of magnetic enthalpy (E_{mag}) by using available literature magnetic moment of 1.12 BM and Curie temperature of 838K [85].

6.6.4 Electronic contribution

Electronic contribution to thermal properties needs to be considered at high temperature because higher kinetic energy of electrons has a significant contribution to the enthalpy. Electronic contribution to specific heat can be given by the well known Sommerfeld formula

$$C_{elc} = 2\pi^2 k_B^2 N(E_F)T/3 = \gamma_e T \qquad (6.19)$$

Table 6.1

List of input parameters used in thermodynamics modeling for alpha and sigma phase of $Fe_{54}Cr_{46}$ alloy

	Alpha	Sigma
Lattice parameter at 298K / *nm*	0.287 (Present study)	a = 0.882 c = 0.445
Volume(m^3)	6.8982 X 10^{-6} (Preston et al[183])	7.2 X 10^{-6} (Liu et al[112])
Bulk Modulus (B_T) (GPa)	221 (Zhang et al[72])	217 (Zhang et al[72])
Pressure Derivative of Bulk Modulus (B_T')	4.18 (Downie et. al[34])	5.8 (Downie et. al[34])
Debye temperature (Θ_D) / K	430 (Downie et al[34]) 410 (Mossbauer study[48])	455 (Downie et al[34])
Grüneisen parameter (γ_G)	1.38 (Calculated in present study)	1.64 (Calculated in present study)
Electronic coefficient (Γ_e) / J mol K $^{-2}$	5 x 10^{-3} (Downie et al[34])	5.6 x10^{-3} (Downie et al[34])
Average Magnetic moment(μB)	1.12 (Xiong et al [85])	-
T_C/K	838 (Xiong et al)	-

6.7 Modeling of thermal properties

Various input parameters for estimation of thermodynamic properties have been tabulated in Table 6.1. Estimated contributions to enthalpy and specific heat of alpha phase are depicted in **Fig. 6.10** and **Fig. 6.11**. The different contributions that arise from lattice vibration, magnetism and kinetic energy of electrons which are separately portrayed in **Fig. 6.10** and **Fig. 6.11**. It is observed from **Fig. 6.10** that the phonon contribution dominates over the other contributions. Total enthalpy and specific heat are obtained by summing up all the individual contributions. It is also observed that the calculated enthalpy is in excellent agreement with the experimental values. The slope change in enthalpy in **Fig. 6.10** due to magnetic transformation is clearly apparent. The magnetic contribution in specific heat for alpha phase has a sizable contribution, which is maximum at Tc and then decreases. The calculation for enthalpy started deviating from experimental data at high temperature because the Debye Grunession formalism is a quasiharmonic model which cannot take care of the total anharmonicity. A similar result is being displayed in **Fig. 6.12** and **6.13** for sigma phase. There is no magnetic contribution associated with the sigma phase.

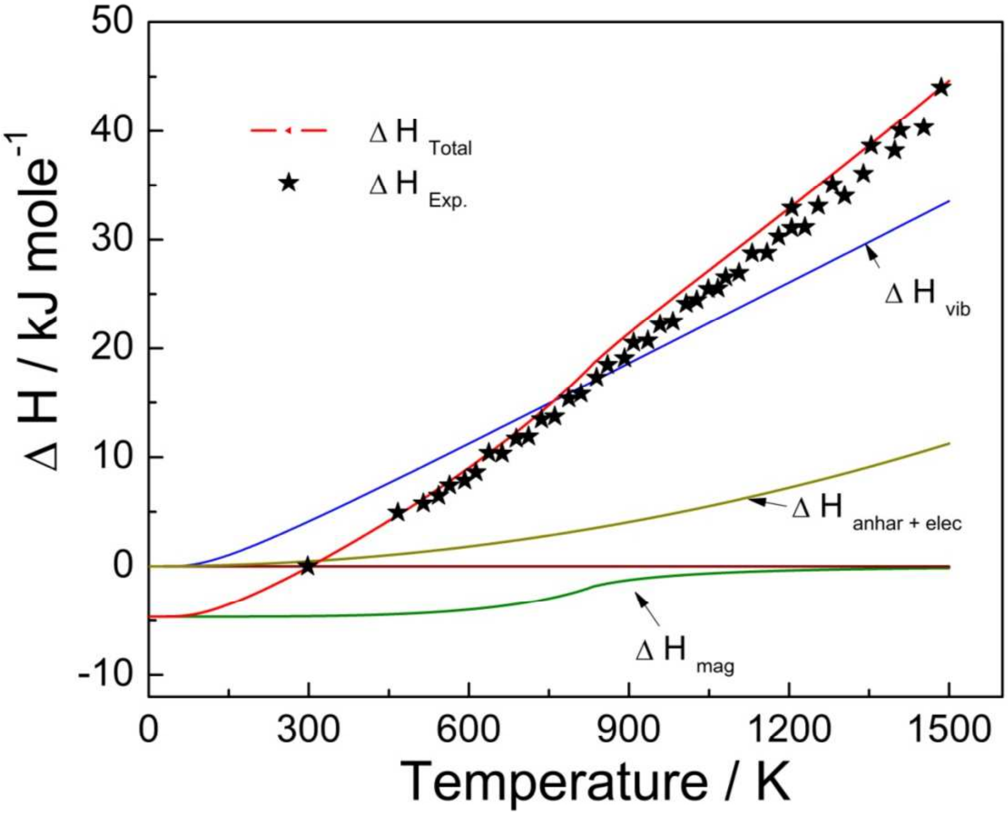

Fig. 6.10 Analytical modeling of enthalpy curve for α phase

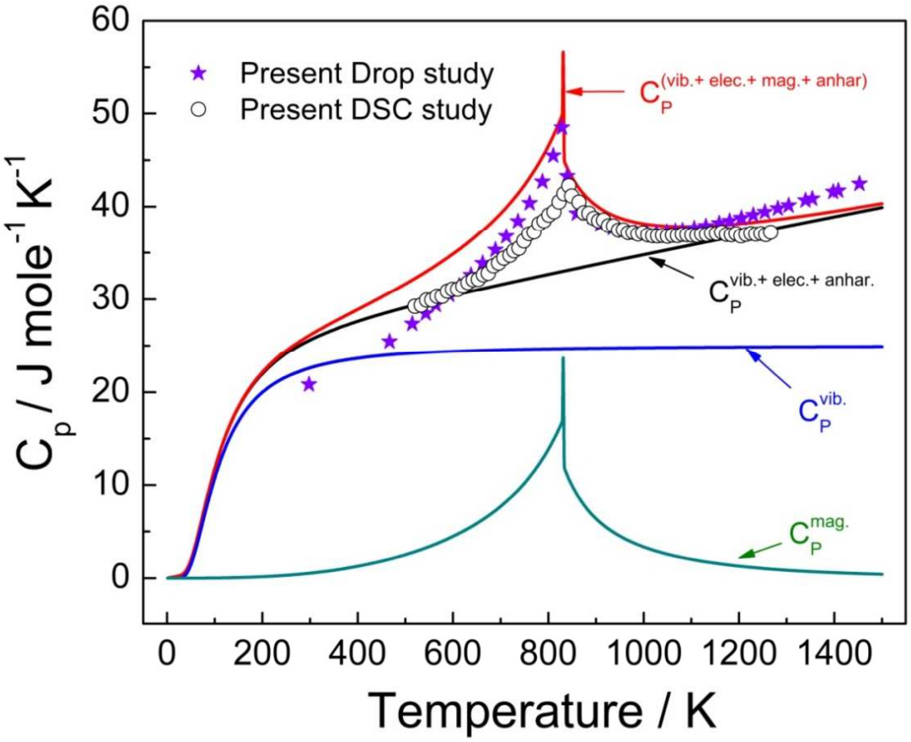

Fig. 6.11 Experimental specific heat is co-plotted with calculated specific heat for alpha phase

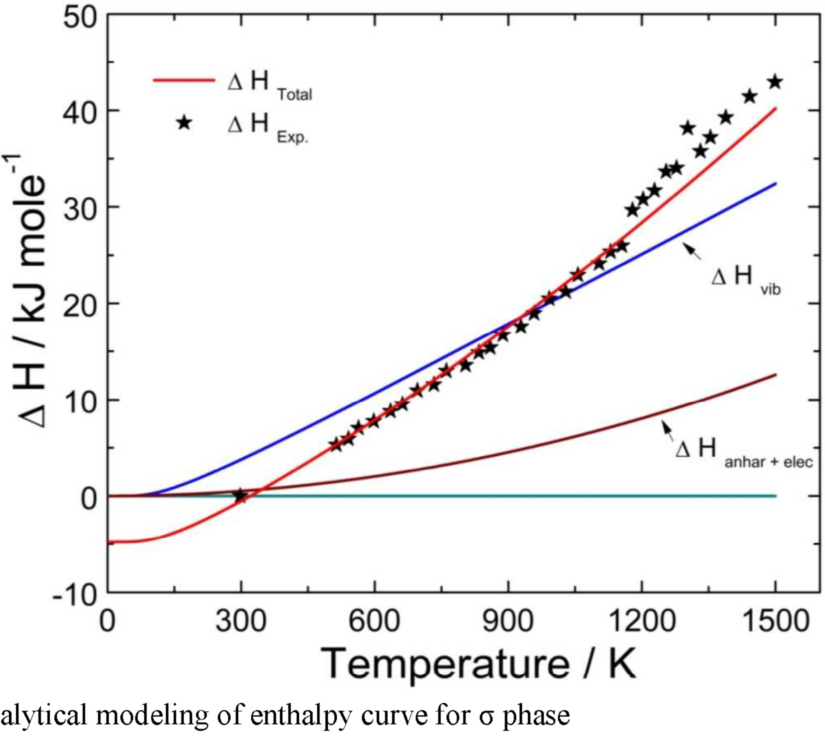

Fig. 6.12 Analytical modeling of enthalpy curve for σ phase

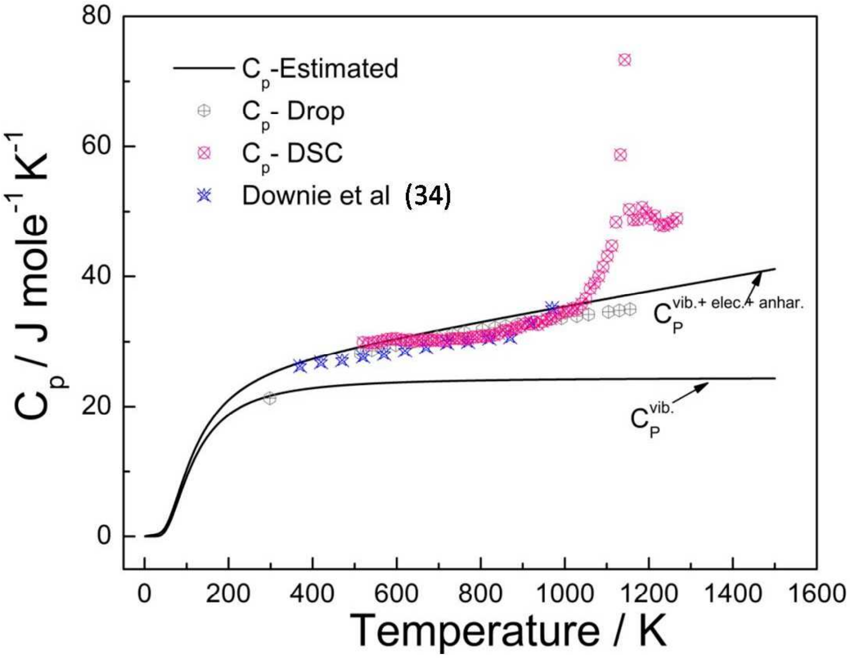

Fig. 6.13 Experimental specific heat is co-plotted with calculated specific heat for σ phase

It is seen from **Fig. 6.12** that calculated enthalpy has good agreement up to the phase transformation region. Beyond that it does not match with the experimental data. The same observation is made in the case of specific heat from **Fig. 6.13**.

6.8 Summary and Conclusions

A comparative study of thermo-physical and heat transport properties is being carried out for alpha and sigma phase of $Fe_{54}Cr_{46}$ alloy. The conclusions of this study are as follows.

(a). Alpha phase does not undergo any phase transformation, however sigma undergoes a phase transformation of $\sigma \rightarrow \alpha$ at 1120 K. The enthalpy of transformation measured 2.6 kJ $mole^{-1}$.

(b). The room temperature thermal expansion coefficient for alpha and sigma phase is 7.39 x 10^{-6} and 1.5 x 10^{-5} K^{-1} respectively.

(c). The room temperature thermal diffusivities of alpha and sigma phase are 0.0484 cm^2 s^{-1} and 0.011 cm^2 s^{-1} respectively. The room temperature thermal conductivity of alpha phase is 16.9 W $m^{-2}s^{-1}$ whereas that of the sigma phase is 3.9 W $m^{-2}s^{-1}$

(d). A comprehensive analytical model is set up to model the experimental thermodynamic parameters which shows a good agreement.

Chapter-7

Effect of W on the α ↔γ transformation characteristics in Fe-Cr based binary and multi component alloys

7.1 Introduction

The high temperature properties of 9 Cr Ferritic/Martensitic steels are governed by its microstructural stability. The steel is used in the normalised and tempered condition consisting of a tempered martensite microstructure, which imparts the best combination of properties for high temperature applications [1-15]. The tempered martensite structure with high density of dislocations and different types of fine scale carbide precipitates is the primary reason for the high temperature mechanical properties [11-15]. The martensite structure is the result of fast cooling after solution treatment in the gamma phase field. The high temperature fcc (Gamma) phase is stabilized by the carbon which arises as a consequence of dissolution of carbides, which is commonly known as austenitisation. After austenitisation, the dissolved carbon is trapped leading to martensite diffusion less transformation due to the fast cooing . Therefore, the events in the gamma phase field has enormous importance to the behavior of ferritic/martensitic steels. It is required to mention here that there exists a huge scatter in the experimental data as already discussed in chapter-1 for gamma phase field of Fe-Cr binary system. The alloying additions in steels shiftthe γ -loop either towards left or right. In this context, the addition of refractory solutes in steels like Mo, W and Ta, which provide solid solution strengthening and delay the coarsening of precipitates, has important effect in stabilising the microstructure [4-9, 18]. It is important to mention here that W added 9Cr steel has attracted considerable attention in the development of economical creep resistant materials [146-156]. Moreover, the development of reduced activation ferritic martensitic steel (RAFM) for fusion reactors, wherein Mo is replaced by W in P91 steel is based on the enhanced strength achieved in addition to addressing the activation problem [146-156]. An increase of W from 1 to 2 wt.% is reported to help in retaining the lath martensite structure [151] as it retards the coarsening of $M_{23}C_6$ precipitates during long term thermal exposures [155]. However, the addition of W is also reported to have adverse effects as it retards the martensite formation [147, 150]. It is observed that addition of W to 9Cr F-M steels has resulted in the formation of undesired ferrite phase along with martensite even under fast cooling conditions [147-151], which has adverse effect on creep properties. The presence of W in $M_{23}C_6$ also influences its dissolution kinetics, which in turn would alter the transformations characteristics at high temperature. Therefore, the role of W addition on transformation behaviour of Fe-9Cr binary alloy and Fe-9Cr-0.1C multi component alloys needs to be understood. In this background, the present chapter deal with α ↔ γ transformation temperatures for Fe - (1-13 wt.%) Cr alloys and the effect of W on α ↔ γ transformation characteristics in Fe-9Cr alloys and its consequences on martensitic transformation in Fe-9Cr-2W-0.1C (P92) steel.

7.2. Study of α↔γ transformation characteristics of Fe-Cr alloys

In order to study the α ↔ γ transformation characteristics, differential scanning calorimeter experiments were carried out for thirteen Fe-Cr alloys employing 3 K min^{-1} heating and cooling rate upto 1550 ^{o}C (1823 K). The experimental results of selective alloys of Fe-1 wt.% Cr, Fe-11 wt.% Cr and Fe-12 wt.% Cr are displayed in **Fig. 7.1 (a), (b)** and **(c)** respectively. Fe-1 wt.% Cr alloy shows three transformations during heating upto melting. These correspond to ferro → para magnetic (Tc), α → γ and γ → α phase transformations at 770 ^{0}C (1043 K), 907 ^{0}C (1180 K) and 1385 ^{0}C (1658 K) respectively. The signature of reverse transformations during cooing are also observed in **Fig. 7.1 (a)**. The results for other alloys (Fe-2 wt.% to 10 wt.% Cr) are not shown here as similar transformation characteristics are observed with different transformation temperatures which have been tabulated in **Table 7.1**. **Figure 7.1(b)** displays the DSC profile for Fe-11 wt. % Cr. The above three transformations are observed at 735 ^{0}C (1008 K), 925 ^{0}C (1198 K) and 1077 ^{0}C (1350 K). The temperature difference between α → γ and γ → α transformations is 478 K for Fe-1 wt.% Cr to 152 K for Fe-11 wt.% Cr. **Figure 7.1 (c)** displays the DSC profile for Fe-12 wt.% Cr alloy which shows magnetic transformation at 730 ^{0}C (1003 K). α → γ transformation is not observed for Fe-12 wt.% alloy in contradiction to the literature. The α → γ and α → γ transformation temperatures are co plotted with literature data in Fig. 7.1(d). It is seen from **Fig.7.1(d)** that gamma phase forms upto 14 wt.% Cr as per literature whereas in the present study gamma phase field exists only upto 11 wt.% Cr. It is necessary to mention here that the magnetic transformation temperature (Tc) has shown a maxima at 5 wt.% Cr which is in agreement with literature.

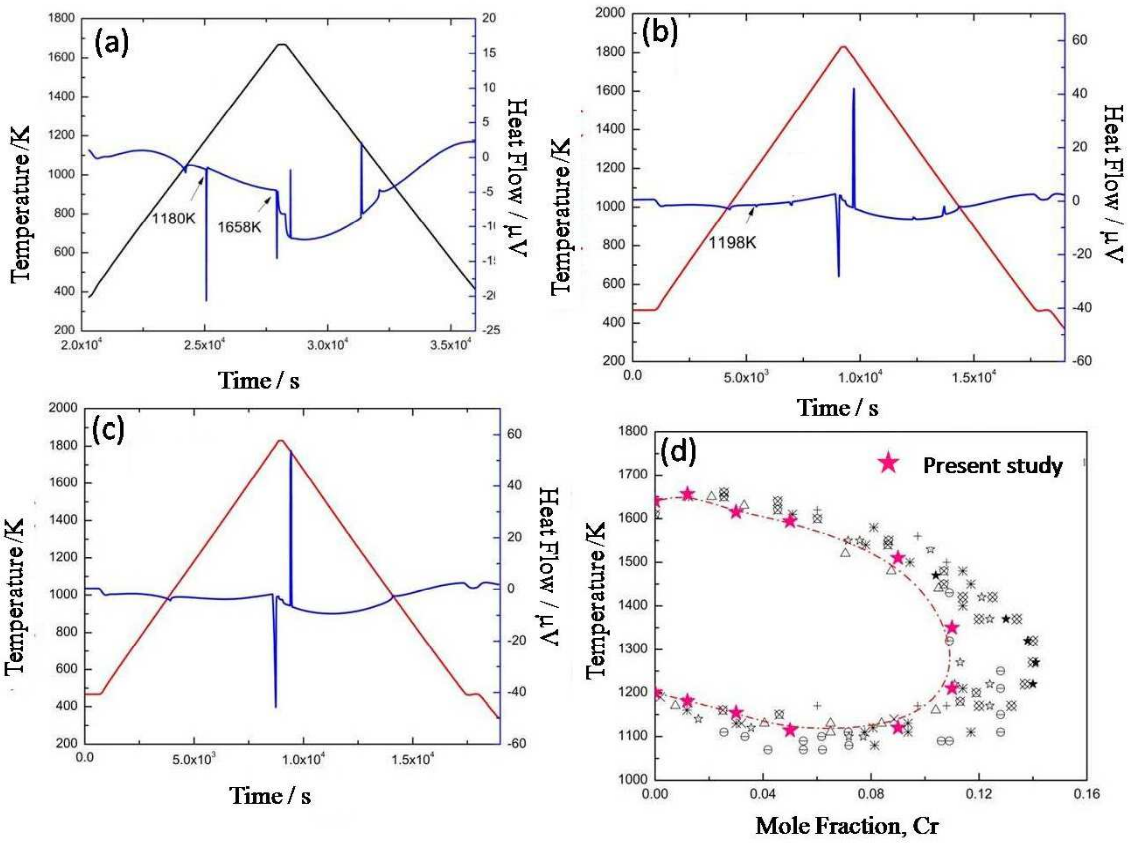

Fig. 7.1 DSC profile for **(a)** Fe-1 wt.% Cr **(b)** Fe-11 wt.% Cr **(c)** Fe-12 wt.% Cr **(d)** α ↔ γ phase transformation temperatures measured in present study is co plotted with available literature data

7.3. Effect of W addition on α↔γ transformation characteristics of Fe-9Cr-xW (x = 1 - 2 wt.%)

Fe-9Cr alloy is the primary alloy for Fe-9Cr based ferritic / martensitic steel whose microstructure stability is dependent on the austenitisation in γ phase field and rate of cooling after austenitisation. W being a bcc stabiliser has negative impact on the stability of fcc phase field.

Table – 7.1

Transformation temperature for Fe-Cr alloy

Alloy	Curie Temperature(Tc)	$T_{\alpha\rightarrow\gamma}$	$T_{\gamma\rightarrow\alpha}$
Fe-1 wt.% Cr	770 ^{0}C (1043 K)	908 ^{0}C (1181 K)	1382 ^{0}C (1655 K)
Fe-3 wt.% Cr	774 ^{0}C (1047 K)	881 ^{0}C (1154 K)	1342 ^{0}C (1615 K)
Fe- 5 wt.% Cr	770 ^{0}C (1043 K)	871 ^{0}C (1144 K)	1321 ^{0}C (1594 K)
Fe-9 wt.% Cr	753 ^{0}C (1026 K)	847 ^{0}C (1120 K)	1237 ^{0}C (1510 K)
Fe-11 wt.% Cr	735 ^{0}C (1008 K)	925 ^{0}C (1198 K)	1077 ^{0}C (1350 K)
Fe-12 wt.% Cr	730 ^{0}C (1003 K)	-	-

Therefore, in order to study the effect of W on $\alpha \leftrightarrow \gamma$ transformation characteristics of Fe-9Cr alloy, differential scanning calorimeter experiments were performed for W added Fe-9Cr alloys employing 3 K min^{-1} heating and cooling rate upto 1550 ^{o}C (1823 K). The experimental results of selective alloys of Fe-9 wt. % Cr – 0.5, 1, 1.5 and 2 W are displayed in **Fig. 7.2 (a), (b)**, **(c)** and **(d)** respectively. **Figure 7.2 (a)** alloy shows the DSC result for Fe-9 wt.% Cr – 0.5 W. Three transformations are clearly observed during heating upto melting which corresponds to ferro → para magnetic (T_c), $\alpha \rightarrow \gamma$ and $\gamma \rightarrow \alpha$ phase transformation at 765 ^{0}C (1038 K), 886 ^{0}C (1159 K) and 1393 ^{0}C (1666 K) respectively. The reverse transformations during cooling are also observed from **Fig. 7.2 (a)** at 745 ^{0}C (1018 K), 903 ^{0}C (1176 K) and 1210^{0}C (1483 K) for 1 W alloy and 746 ^{0}C (1019 K), 895 ^{0}C (1168 K) and 1201 ^{0}C (1474 K) for Fe-9 wt.% Cr-1.5W alloy.

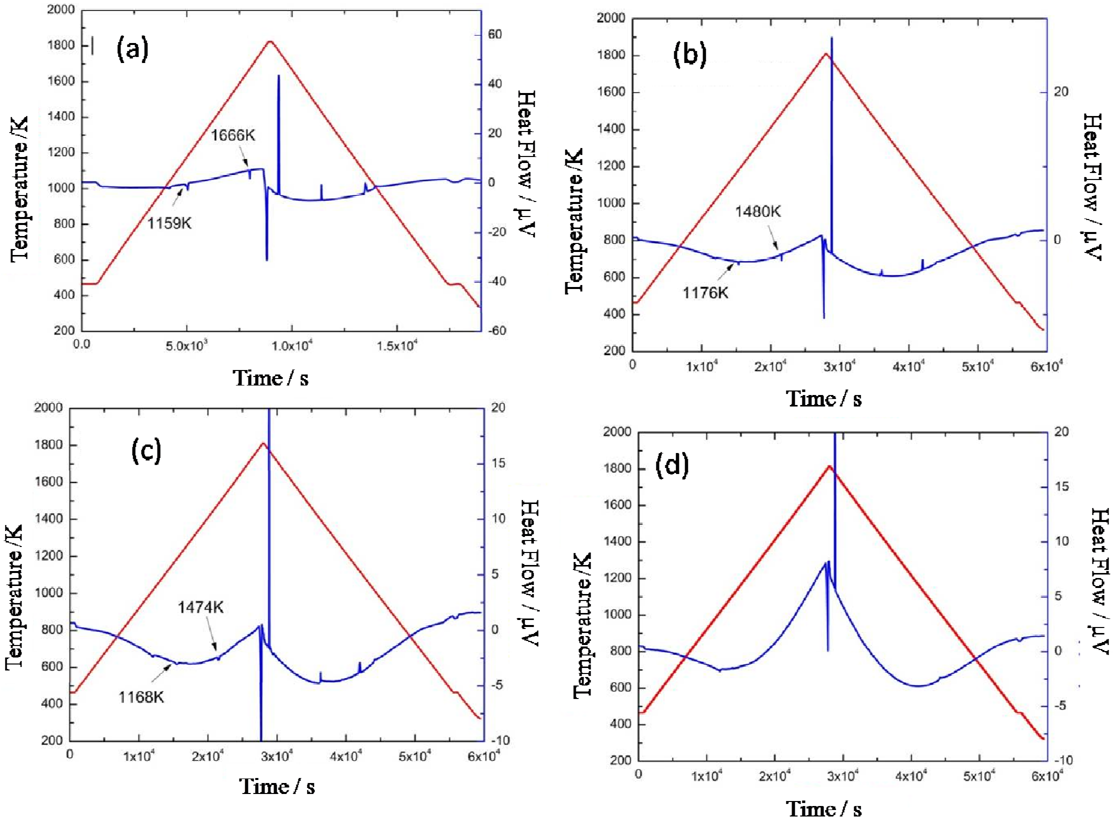

Fig. 7.2 DSC profile for **(a)** Fe-9 Cr–0.5 W, **(b)** Fe-9 Cr-1 W, **(c)** Fe-9 Cr-1.5 W and **(d)** Fe-9Cr-2W

The temperature difference between α → γ and γ → α is reduced significantly from 507K for Fe-9 wt.% Cr-0.5W to 306 K for Fe-9 wt.% Cr-1.5W. **Figure 7.2 (d)** shows the DSC profile for Fe-9 wt.% Cr-2W alloy which shows only the magnetic transformation at 742 ^{0}C (1015 K) upto melting. α → γ transformation is not observed for Fe-9 wt.% Cr-2W, which indicates that this alloys is stable in the ferrite phase. This signifies that the martensitic transformation in 9Cr based ferritic/martensitic steel is suppressed with the addition of W beyond 1.5 wt.%. The effect of W on 9Cr based ferritic martensitic steel is described in the subsequent sections.

7.4 Study of transformation characteristics in Fe-9Cr-2W-0.1C multicomponent alloy (P92 Steel)

7.4.1 Thermal Characterisation of P92 Steel

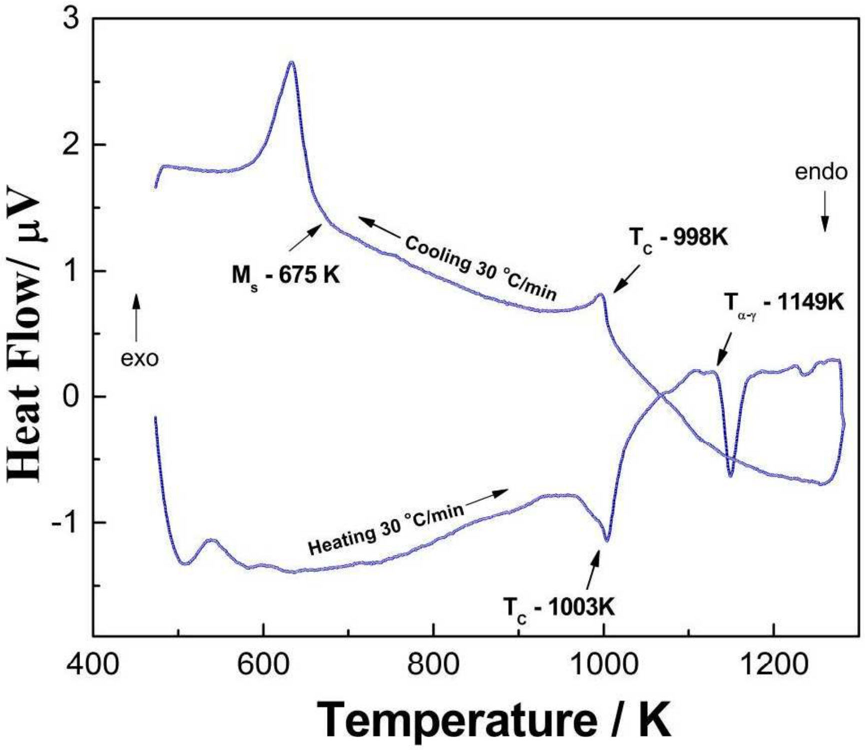

Fig. 7.3 DSC thermogram of P92 steel obtained at the scan rate of 30 K min^{-1} clearly reveals the presence of magnetic peak at 725 ^{0}C (998 K) prior to martensitic transformation during cooling

A typical DSC profile of the steel heated in Ar atmosphere to 1000 ^{0}C (1273 K) at a constant rate of 30 K min^{-1} held for 1 h and then cooled at 30 K min^{-1} is given in **Fig. 7.3** It is evident from the heating and cooling DSC profiles that the steel has witnessed two phase transformation events in each cycle. The transformation at 730 ^{0}C (1003 K) in the heating cycle can be correlated to the magnetic transformation of ferromagnetic to paramagnetic ferrite (α) phase. The Curie temperature (T$_c$) of P92 steel is measured as 730 ^{0}C (1003 K) which is in agreement with literature reports [147, 152]. The second endothermic peak during heating is observed at 876 ^{0}C (1149 K) which is attributed to the structural transition from bcc-ferrite (α) to fcc-austenite (γ) phase. On a similar account the first peak observed at 725 ^{0}C (998 K) during cooling from austenite is followed by a second phase change commencing at 403 ^{0}C (676K) and ending around 370 ^{0}C (643K). In order to confirm these two phase transformations during cooling cycle another set of DSC experiments were carried out on P91 steel which does not contain tungsten.

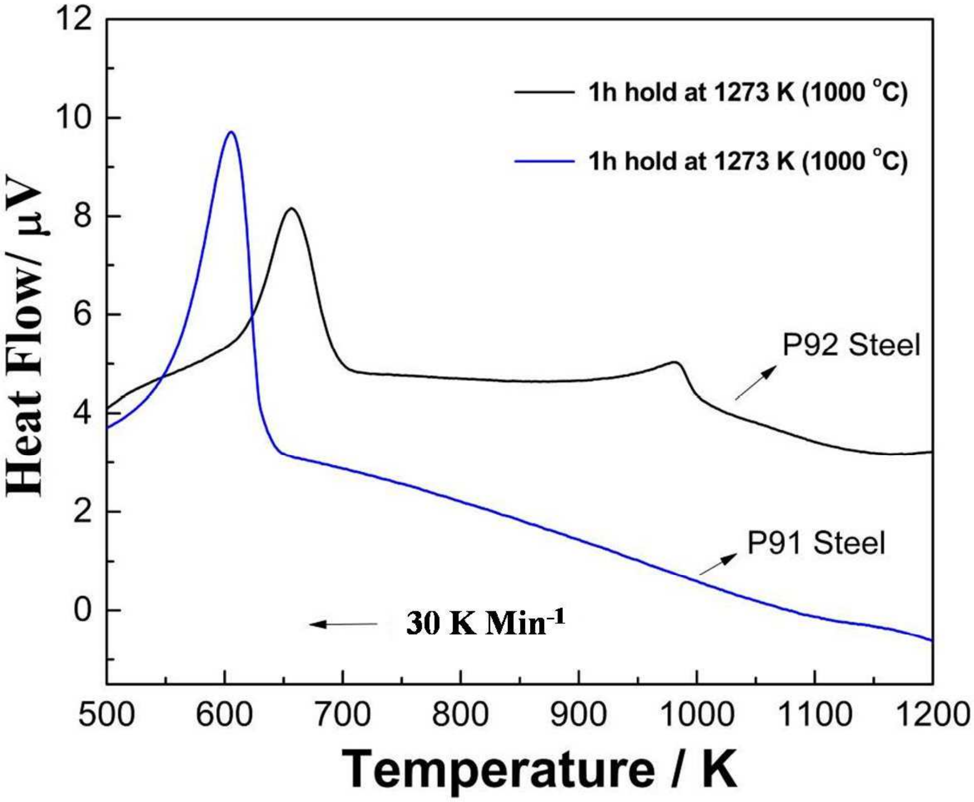

Fig. 7.4 Comparison of DSC cooling profile for P92 and P91 steel under identical experimental condition obtained at the scan rate of 30 K min^{-1} shows the absence of magnetic transformation in P91 in contrast to P92 steel

Comparison of the cooling profiles of P92 and P91 steels (**Fig. 7.4**) shows the following differences;

i. P91 steel exhibits a single transformation peak during cooling from high temperature γ phase which corresponds to M_s (368 °C (641 K)) and M_f (340 °C (613 K)), as also supported by literature [147, 152]. Contrary to expectation in ferritic – martensitic steels P92 exhibits two peaks. Based on the above observation and literature the analogous low temperature peak in P92 commencing at 403 °C (676 K) and ending at 370 °C (643K) is attributed to martensitic transformation.

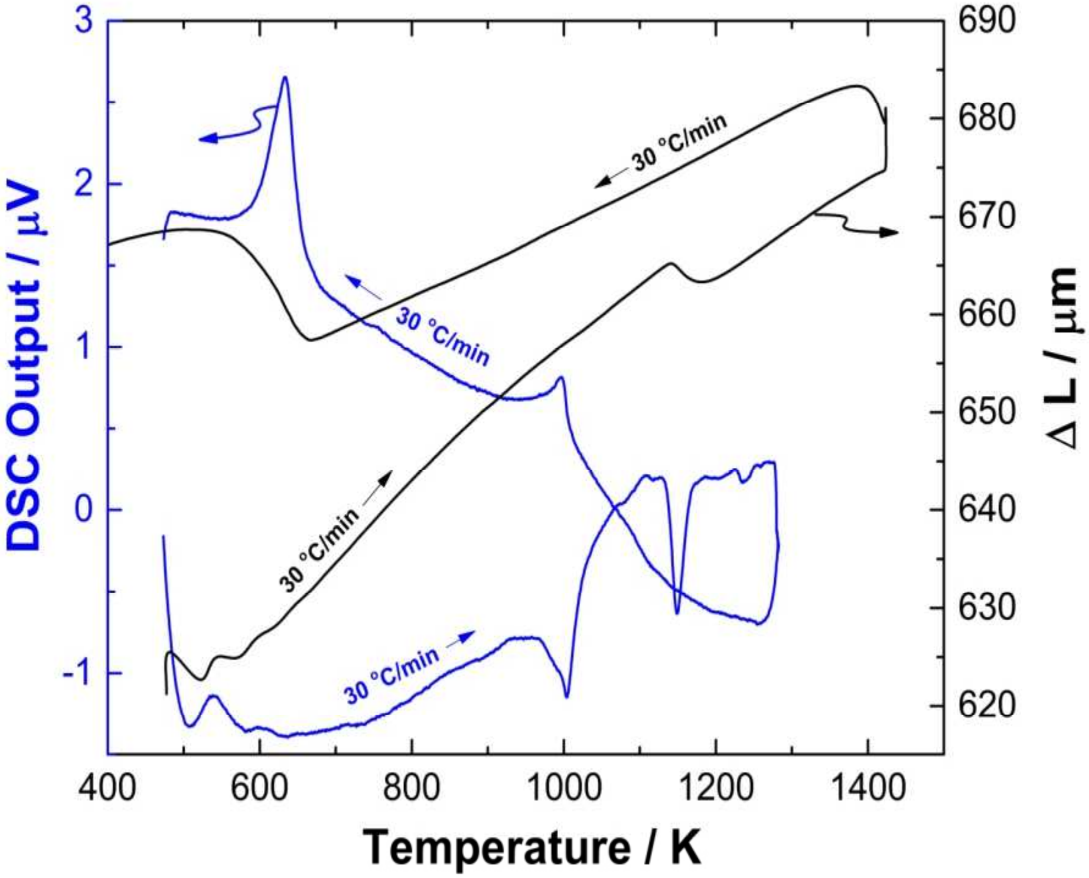

Fig. 7.5 Comparison of DSC and TMA profile for P92 steel obtained at 30 K min^{-1}, confirms that no magnetic transformation peak is attested in both heating and cooling cycle

ii. However, the peak at 725 ^{o}C (998 K) in P92 steel is not observed in P91 steel.

This additional peak compares with the heating profile in P92 (**Fig. 7.4**) where the peak has been ascribed to the on-heating magnetic transition temperature (T_c = 730 ^{0}C (1003 K)). This suggests the possibility of a magnetic phase transformation during cooling in P92. In order to confirm the speculations a dilatometer experiment was carried out and the results are compared in **Fig. 7.5**. A single inflection corresponding to a structural transition is observed in the heating and cooling dilatometer profile in contrast to DSC profile. The transformation at 876 ^{o}C (1149 K) observed during heating in the dilatometer profile corresponds well with the structural transition of ferrite (α) to austenite (γ) as also observed in DSC profile. However, the magnetic transition is not detected by dilatometer during heating cycle, which is quite possible as magnetic transition does not manifest as a detectable volume change. Similar observation has been made during cooling and a single peak due to martensitic transformation alone is observed in dilatometer experiment which is in complete agreement with the DSC results. It is therefore evident that the first transformation observed at 725 ^{o}C (998 K) in DSC cooling profile is associated with a magnetic transition. Further, the absence of a thermal hysteresis during heating and cooling cycles (**Fig. 7.3**) confirms that it is a second order transformation quite typical of a magnetic transformation. Based on the above results it is clear that a magnetic transformation is observed in P92 steel prior to martensitic transformation at a cooling rate of 30 K min^{-1} from austenitising temperature of 1050 ^{o}C (1323 K). This suggests the presence of a certain volume fraction of ferrite phase along with γ phase. The co-existence of ferrite phase along with martensite is further attested in the microstructure of P92 steel cooled at 30 K min^{-1} in **Fig 7.6 (a).** However, no ferrite phase has been observed in the microstructure of P91 steel shown in **Fig. 7.6 (b)** cooled under similar conditions. The presence of ferrite in P92 steel can be explained either by formation of diffusional ferrite during cooling of high temperature γ phase or alternately it is untransformed ferrite (retained) during austenitisation, and will be dealt with in the subsequent section.

.4.2. Effect of solution treatment conditions on transformation characteristics

In order to identify the reasons for the co-existence of ferrite and austenite in P92 steels and to optimise the heat treatment conditions for formation of full martensite product, a set of experiments were carried out by varying the thermal history. Three different variables namely cooling rate, austenitisation temperature and holding time were varied systematically in the DSC, the results of which will be described in sequence.

In the first set of experiments on cooling rate variation, all the samples were heated at 10 K min^{-1} to 1050 ^{o}C (1323K) and cooled at various rates in the range of 1-90 K min^{-1}.

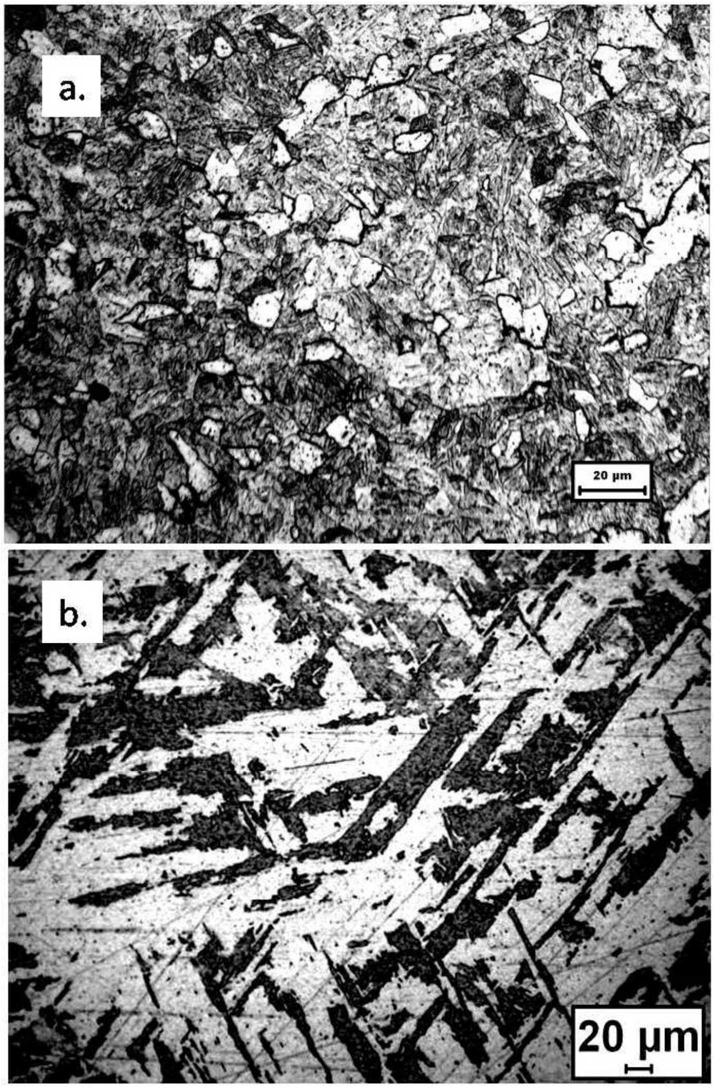

Fig. 7.6 Microstructure of 30 K min^{-1} cooled post DSC sampe of (a.) P92 and (b.) P91 steel shows the presence of ferrite phase in P92 steel in contrast to P91 steel which has complete martensite structure

The DSC cooling profiles of the specimen cooled at 1, 5, 10, 20 K min^{-1} are shown **Fig. 7.7(a)** and cooling profiles of 30, 50, 90 K min^{-1} are shown in **Fig 7.7 (b).** The presence of an exothermic peak at ~ 726 ^{o}C (999 K) is observed in **Fig.7.7 (a),** which correlates with a magnetic transition. On the other hand, peak corresponding to martensitic transformation is not observed for cooling rates of 1, 5 K min^{-1}. This suggests the formation of proeutectoid (diffusional) ferrite during cooling at such slow rates. However, there is evidence for formation of martensite when the sample was cooled at 10 K min^{-1}, in the form of two small exothermic peaks. At a cooling rate of 20 K min^{-1} a single peak is observed for the martensitic transformation along with the magnetic phase transformation at ~ 726 °C (999K).

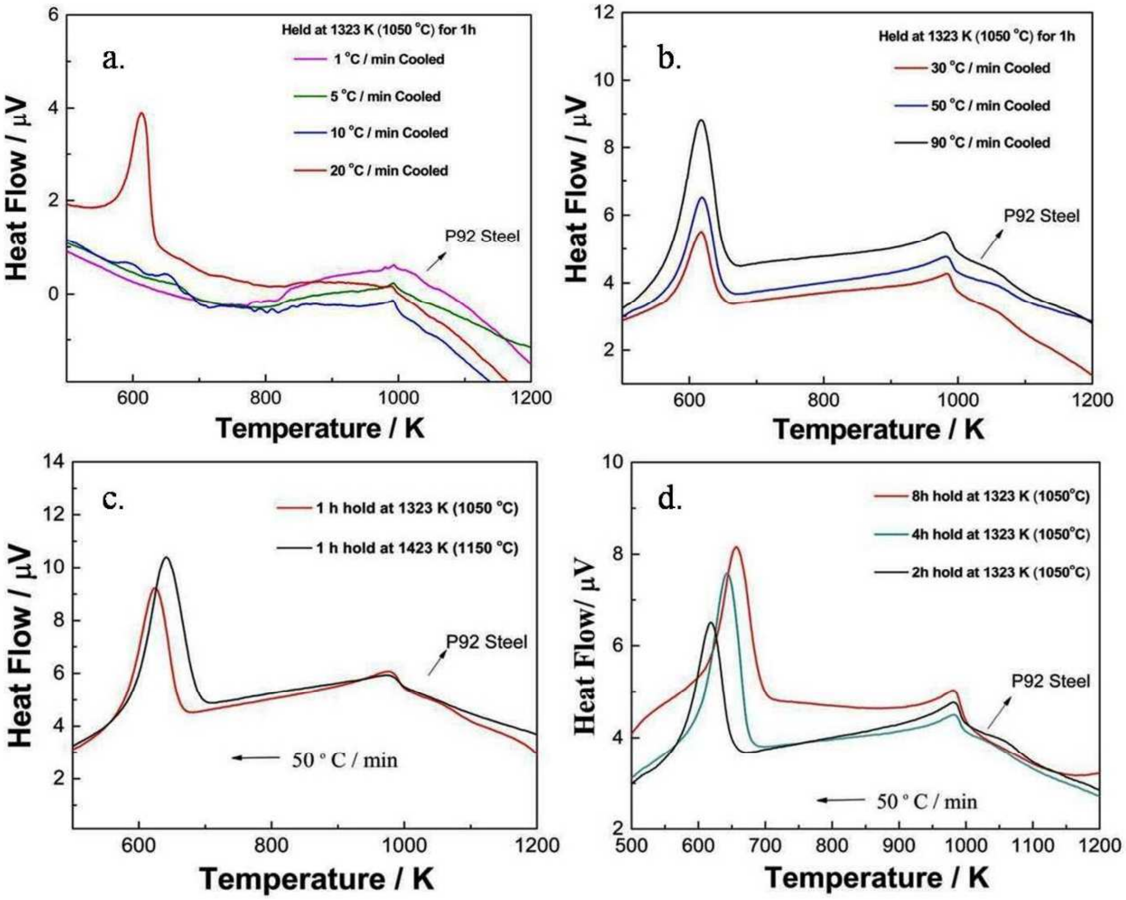

Fig. 7.7 (a.) & (b) DSC cooling profile of P92 steel obtained at different cooling rates in the range of 1-90 K min^{-1}, **(c.)** DSC cooling profile of P92 steel obtained at constant cooling rates for different austenitisation temperature **(d.)** DSC cooling profile of P92 steel obtained at constant cooling rates for different austenitisation time at 1050 °C (1323 K)

A similar behaviour is observed (**Fig 7.7 (b)**) for higher cooling rates of 30 - 90 K min^{-1}. Hence, it is clear that varying amounts of proeutectoid ferrite forms during cooling at rates below 10 K min^{-1}. Hence, it can be concluded that the critical cooling rate (Q_c) for martensite formation is between 10 - 20 K min^{-1}. The presence of the magnetic transition is evident at all cooling rates from **Fig. 7.7 (a)** and **Fig. 7.7 (b),** which confirms the presence of ferrite. Although formation of diffusional ferrite at low cooling rates is quite possible, its presence at high cooling rates > 50 K min^{-1} is rather unexpected. This suggests a strong possibility that ferrite is retained during austenitisation at 1050 °C. Hence, in the second set of experiments austenisation temperature has been varied in the range of 1050-1150°C (1323-1423K). A set of samples have been heated at 10 K min^{-1} to different austenitising temperatures (1323 & 1423K) and held for 1 h followed by cooling at 50 K min^{-1}. The cooling DSC profiles obtained from the above experiments are shown in fig.7.7(c). The presence of two distinct peaks which can be correlated to magnetic and martensitic formation is evident, which is similar to the observations in **Fig 7.7 (a & b). Figure 7.7(c)** also shows the magnetic transition to occur at 726 °C (999 K) in both the cases. Further, an increase in Ms temperature by ~30K with increase in austenitisation temperature from 1050 to 1150°C (1423K) is also observed. This is attributed to the higher extent of dissolution of carbides at 1150°C which enhances the carbon concentration in the austenite and a higher driving force for martensite formation. The presence of magnetic peak again implies the co-existence of ferrite and austenite while the higher austenitisation temperature and cooling rate (50 K min $^{-1}$ > Q_c) adopted in this experiment only facilitates martensitic transformation and precludes the possibility of proeutectoid ferrite during cooling. In the third set of experiments the samples have been heated at 10 K min^{-1} to 1050 °C (1323K) and held for different time durations of 1-8 hours and subsequently cooled at 50 K min^{-1}. The corresponding DSC cooling profiles are depicted in **Fig.7.7 (d).** The persistence of the magnetic transition peak at ~ 726 °C (999 K) is observed for all hold times. However, an increase in M_s from 665 to 710K with increase in hold time from 2 to 8 h is observed. This is also attributed to the higher extent of dissolution of carbides with increase in hold time, similar that obtained for higher austenitisation temperatures. In addition, larger prior austenite grain size with higher austenitisation temperature and hold time promotes the martensite formation [18]. Reference formatting is not correct. It is clear from the above DSC results that the ferrite phase, attested by a magnetic transition continues to exist, despite increase in austenitisation temperature, hold time and cooling rate.

7.4.3. Effect of cooling rate on microstructural evolution

Typical SEM micrographs of P92 steel cooled from 1050 ^{o}C (1323 K) at cooling rates of 1, 30 and 90 K min^{-1} are shown in **Fig. 7.8(a-c). Figure 7.8 (a)** shows the presence of ferrite phase with no evidence for martensite at 1 K min^{-1}. The average microhardness measured was ~ 180 VHN, which is in agreement with the values for soft ferrite phase. A careful observation of **Fig. 7.8 (a)** revealed ferrite of two distinct size distributions. The presence of few ferrite grains of average size ~ 5 μm along with predominantly large ferrite grains (<20 μm) is observed. This distribution suggests that the mechanism of their formation is different. In conjunction with the DSC data it is understood that small fraction of ferrite grains have been retained during austenitisation, while most part of the larger grain sized ferrite has formed by diffusional transformation during cooling from austenite. Microstructures of 30 and 90 K min^{-1} cooled samples have been portrayed in **Fig. 7.8 (b and c).** From these two micrographs the presence of small islands of ferrite (~10-15 volume %) in a predominantly lath martensite microstructure is observed for higher cooling rates. The average microhardness has been measured as 182 and 348 VHN from the ferrite and martensite constituents respectively, which also supports the presence of ferrite. In order to completely eliminate the formation of pro-eutectoid ferrite a sample was austenitised at 1050°C (1323 K) with a hold time of 8h and water quenched. The microstructure of this specimen (**Fig. 7.8(d))** also shows the clear presence of ferrite (~188VHN) surrounded by a martensite matrix (~362VHN). From the reported TTT diagram of 9 Cr – W steel there is no evidence for formation of diffusional ferrite for high cooling rates as employed in the present study [202]. The presence of retained ferrite at high temperature (austenitsation) in P92 steel is therefore concluded from the DSC and metallography studies. It may be recalled that Ac_1 and Ac_3 have been evaluated as 1149 and 1180K for this steel. This suggests that although the austenitisation temperatures adopted in this study (1273 – 1423K) are well above Ac_3 the experimental results point towards the retention of ferrite during solution treatment. It is needless to say that tungsten plays a role in controlling the mechanism and kinetics of the phase transformations.

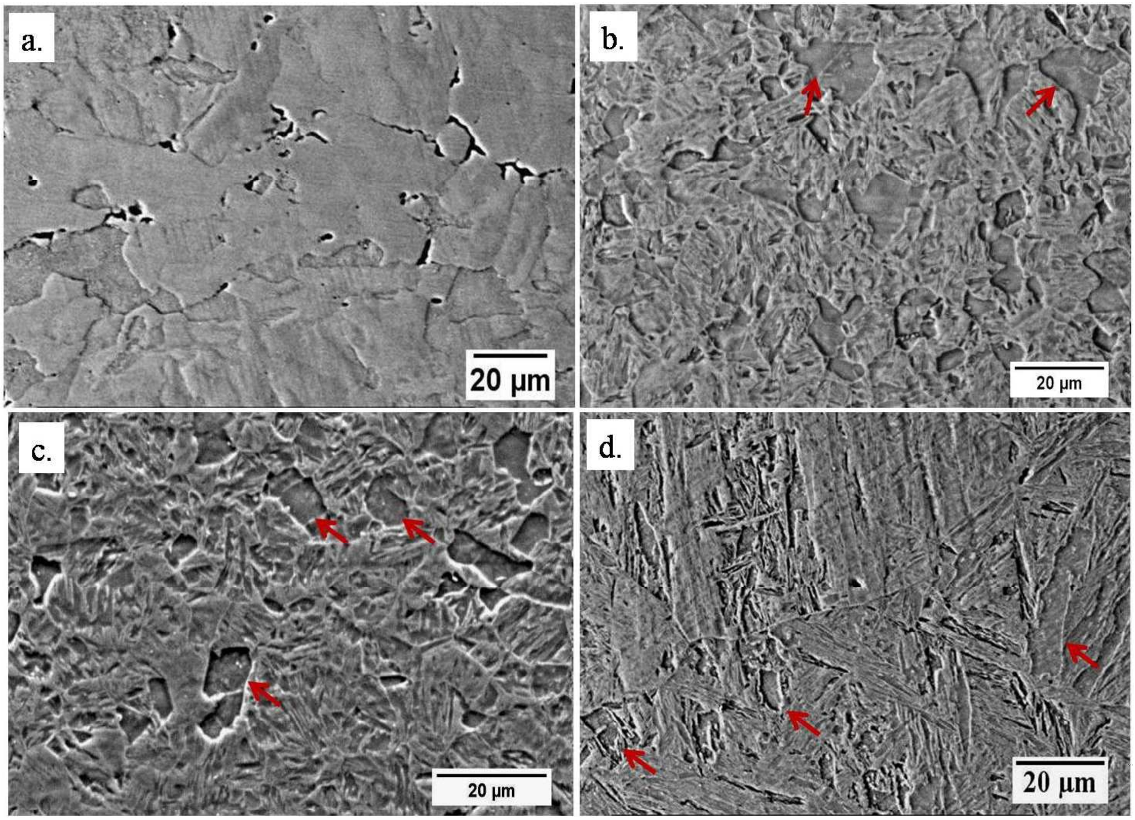

Fig. 7.8 Microstructure of post DSC P92 steel samples cooled at (a.) 1 K min^{-1} (b.) 30 K min^{-1} (c.) 90 K min^{-1} (d.) water quench from 1050 °C (1323 K)

7.5 Thermo-Calc simulation of equilibrium phases

In order to obtain a deeper insight into the role of tungsten in the co-existence of ferrite and γ phase under equilibrium conditions at high temperature, the phases in P91 and P92 steels with varying composition or W content have been simulated using Thermo-Calc, the results of which are presented here. Thermo-Calc simulated pseudo binary phase diagram (in terms of carbon isopleths) of P91 steel has been presented in **Fig.7.9 (a).** The dotted line in red represents the composition of P91 steel in terms of carbon content. The Ac$_1$ temperature of P91 steel evaluated by Thermocalc is in reasonable agreement with the DSC data (**Fig.7.4**). It is observed that the steel remains completely within the gamma loop at the austenitisation temperature of 950 °C (1223 K), 1050 °C (1323 K) and 1150 °C (1423 K). However, presence of MX carbide is seen until 1050°C. Higher austenitisation temperatures of 1150 °C (1423 K) and above although facilititates formation of single phase γ after dissolution of MX, but may also lead to formation of δ ferrite phase. It is seen from **Fig. 7.9 (a)** that the allowed austenitisation temperature window to effect a complete martensitic transformation is in the range of 900-1150°C for P91 steel. Since P92 steel is a derivative of P91 with W addition, the effect of W on phase stability of P91 steel has been also simulated by Thermo-Calc and the results are shown in **Fig. 7.9 (b & c)** with sequential incorporation of 1 and 1.5 wt.% of W respectively, maintaining other alloying contents fixed. It is observed from **Fig.7.9 (a-c)** that with W addition the high temperature γ phase field shrinks which is manifested as a progressive shift towards the right side. The presence of some amount of δ phase together with austenite is also predicted in W containing P91 with addition of > 1 wt. W at austenitisation temperature of 1150 °C steel in contrast to P91. The pseudo binary phase diagram of P92 steel used in the present study has been simulated and shown in **Fig. 7.9 (d).** The simulated Ac_1 temperature is in fair agreement with the DSC results. Interestingly, it is observed that the steel does not enter the γ single phase domain at high temperature. However, it resides in the three-phase domain of $\alpha + \gamma + MX$ at 950 °C (1223K) and 1050 °C (1323K). Further increase in austenitisation temperature shifts the domain to the two phase $\gamma + \delta$ domain. The observed shift in the γ loop due to the addition of 1.9 wt. % W indicates that formation of single phase γ is not possible for the alloy composition of P92. The co-existence of austenite and ferrite at all austenitisation temperatures derived by Thermo-calc simulation clearly supports the experimental data described in previous sections.

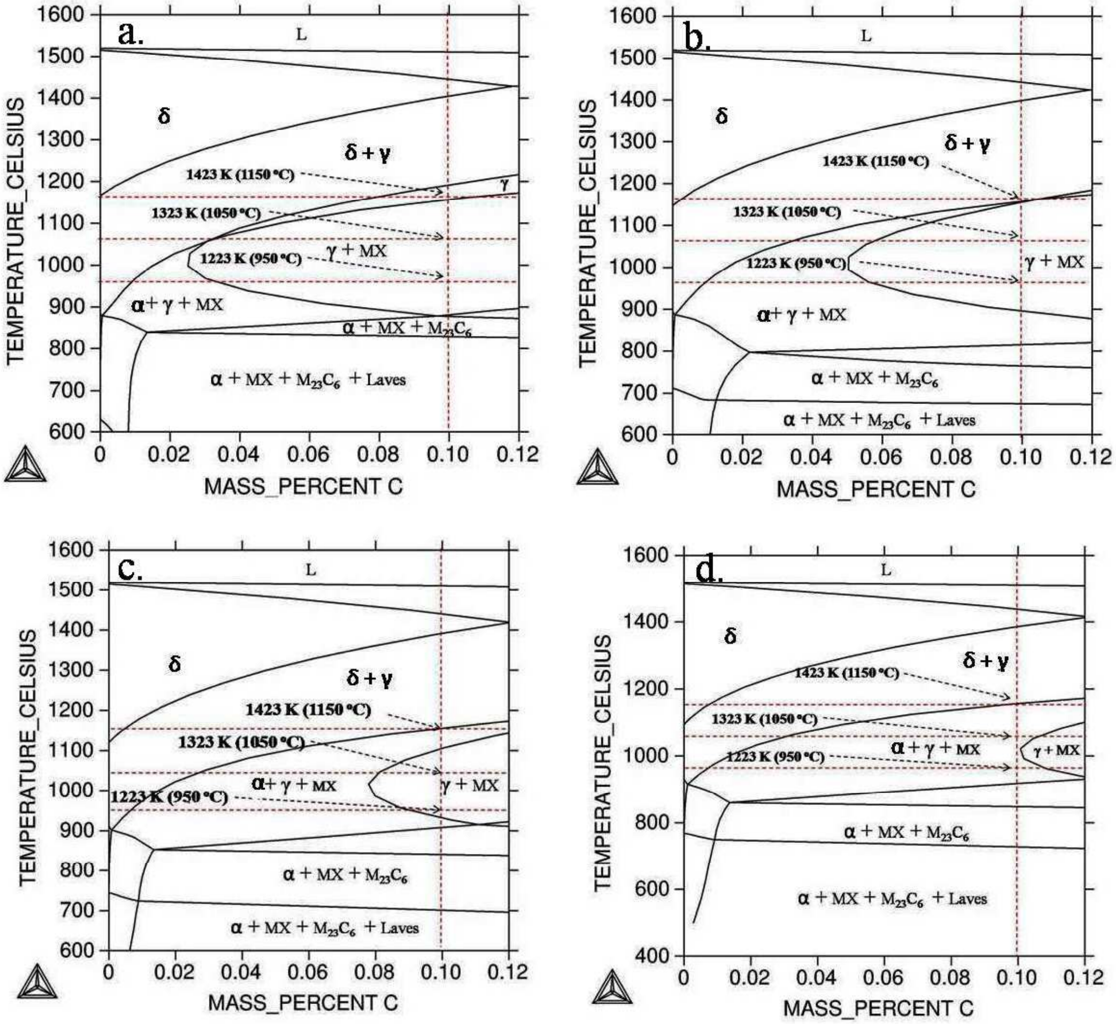

Fig. 7.9 Equilibrium isopleths obtained by Thermo-Calc TCFE6 database for (a.) P91 steel, (b.) P91+1W steel, (c.) P91 +1.5 W steel, (d.) P92 steel

7.6. Impact of W on the industrial heat treatment process of P92 steel

9Cr ferritic/martensitic steels are used in the normalised and tempered condition as structural material for most industrial applications. The tempered martensitic structure with a high dislocation density, intra and inter lath carbides possesses the best combination of strength and toughness for high temperature applications. It has been realised that the addition of W results in retaining martensite lath and carbide in fine scale during long term high temperature exposure. Additionally, like other refractory metals W is a solid solution strengthening element. As consequence, it has been reported that P92 has better creep resistance than P91 steel. Therefore, the development of W added 9 Cr ferritic/ martensitic steel (P92) is indeed indispensable to improve the high temperature mechanical properties particularly creep strength. The basis of heat treatment in ferritic- martensitic steels is to produce a martensite by normalising from a temperature above Ac_3 followed by a tempering process at a temperature close to the nose of the C- curve in the TTT diagram. In this context, the presence of ferrite phase together with martensite in the normalised condition is not desirable. The presence of 8 – 10 % volume percent of ferrite phase in P92 steel has also been reported in literature [150,152]. The presence of a peak at ~ 725 ^{o}C (998K) preceding the martensitic transformation in the DSC thermogram of P92 steel cooled at 30 K min^{-1} from 1000 ^{o}C (1273K) (**Fig. 7.3**) provided the first indication for existence of the magnetic ferrite phase, which was also supported by dilatometry experiments. The room temperature microstructure of this specimen (**Fig. 7.6(a)**) also confirmed the presence of 10-15% of ferrite dispersed in the martensite matrix, in contrast to the results for P91 steel (**Fig. 7.3** and **Fig. 7.6(b)**). Systematic variation of cooling rate, austenitisation temperature and hold time also did not produce complete martensite formation in P92 steel. One of the possible reasons for presence of ferrite arises through a diffusional transformation from $\gamma \rightarrow \alpha$ during cooling from γ. However, the TTT diagram of 9Cr steel shows the possibility of difffusional ferrite at cooling rates below 10 Kmin^{-1} [12]. A possible cause for deviation from the TTT diagram can be due to fluctuations or local inhomogenity in chemistry. However, this possibility is ruled out as the specimen was held for prolonged duration of upto 8 h at austenisation temperature prior to fast cooling. Another possibility could be the substantial shift in the nose of TTT diagram to shorter times due to W addition, which could lead to ferrite formation even at cooling rates as high 90 K min^{-1} used in the present study. However, no significant change in the TTT diagram of P92 with respect to P91 has been reported in literature [203]. Further, the presence of ferrite has also been observed in water quenched sample also (**Fig. 7.8.(d)**), which clearly eliminates the possibility of formation of diffusional ferrite at cooling rates exceeding 30 K min^{-1}. It is reported that $M_{23}C_6$ in W containing ferritic - martensitic steels although predominantly is Cr rich, it also contains substantial amounts of W [148]. The dissolution of $M_{23}C_6$ carbides above Ac_1 releases carbon and provides the driving force for austenite formation. The sluggish kinetics of dissolution of $M_{23}C_6$ carbides in W containing ferritic- martensitic steels with increase in W content is also reported. However, in the present study increase in austenitisation temperature to 1150 °C (1423 K) and hold time to 8h at 1050 °C (1323 K) has also been attempted, which rules out the possibility of $M_{23}C_6$ dissolution kinetics inhibiting the formation of complete austenite. The persistence of the magnetic peak (**Fig. 7.7**) irrespective of the experimental conditions adopted in this study clearly is an affirmation of the co-existence of ferrite and austenite at high temperature, implying an incomplete transformation of $\alpha \rightarrow \gamma$. The Thermocalc simulated pseudo binary phase diagram showed that P91 steel resided completely within the γ loop at austenitisation temperature. This suggests that tungsten exerts a significant role in the incomplete transformation of $\alpha \rightarrow \gamma$ in P92 steel. It is seen from the Thermocalc simulation that addition of high amount (1.9%) of bcc W, a ferrite stabiliser, shifts the high temperature γ loop to the right with a consequent shrinking of the high temperature austenite domain. The existence of $\alpha + \gamma + MX$ and $\gamma + \delta$ at lower and higher austenitisation temperatures confirms that single phase γ is not achievable for the P92 steel composition employed in this study. Based on the above discussions it is evident that a fully martensitic product cannot be achieved in P92 steel for the chosen alloy composition under the industrially adopted heat treatment conditions of normalising. The presence of small amounts of ferrite (≤ 5 volume %) is not reported to adversely affect the mechanical properties. Degradation of properties vis-à-vis microstructure in presence of higher amount of ferrite is also reported [16-17], which could possibly be compensated by the substitutional solid solution strengthening effect of W. Hence, a careful tailoring of composition is essential to obtain the required mechanical properties.

7.7 Summary and Conclusions

- DSC and metallographic study confirm the presence of ferrite phase in a martensite matrix during normalising of P92 steel.
- Thermo-Calc simulation shows that bcc stabiliser W destabilises high temperature γ phase field.
- P92 steel was established to remain in two phase $\alpha + \gamma$ (+ MX) domain by Carbon isopleths.
- Complete martensite formation has not been achieved for the P92 steel used in this study.

Chapter 8

Summary & Further Avenues of Research

8.1. Summary of the present study

This thesis presented the results of a detailed investigation on phase stability, thermo-physical and heat transport properties of alpha (α) and sigma (σ) phases in Fe-Cr alloys. The kinetics of α↔γ phase transformation has also been studied, with emphasis on the role of alloying elements like chromium and tungsten on the transformation characteristics and its influence on the behaviour of engineering materials like P92 steel. A variety of experimental techniques and analytical modelling has been used in this study to evaluate thermodynamic parameters to obtain a comprehensive database and a deeper insight into the physical metallurgy of Fe-Cr based systems. Static and dynamic calorimetry has been used as the major experimental technique in association with metallography and hardness measurements to study the high temperature phase stability and thermal properties. Laser flash thermal diffusivity and thermo-mechanical analyzer have been employed to measure the thermal conductivity and thermal expansion. The salient results of the thesis are summarized as follows.

1) The magnetic, anharmonic and electronic contributions to the high temperature phase stability of Fe rich Fe-Cr alloys were estimated quantitatively which partially fills the gap on thermal property data in this system. Enthalpy increment (H_T-$H_{298.15}$) and heat capacity in the temperature range of 200 – 1200 °C (473 to 1473 K) have been measured for Fe-16 at.% Cr alloy using drop calorimetry.
2) A consolidated physically based model has been proposed which fully describes the thermodynamic properties of ferromagnetic α phase in Fe-rich Fe-Cr alloys (0-16 wt. %Cr). The high temperature calorimetry data has been integrated into the physically based modelling protocols, to establish a wholesome conceptual basis of phase stability in Fe rich Fe-Cr system.

3) Phase separation (α’ + α”) in Fe-21 at.% Cr alloy was established by inverse drop calorimetry. Two distinct phase transformations in Fe-21Cr alloy namely (i) α’ (Fe-rich) + α” (Cr-rich) → α at 447±10 °C (720±10 K) and (ii) $\alpha_{\text{ferromagnetic}} \rightarrow \alpha_{\text{paramagnetic}}$ at 652±10 °C (925±10 K) were established. The measured enthalpy data in conjunction with available literature enabled an integrated theoretical assessment of the energetics of α’+α”→α, and $\alpha_{ferro} \rightarrow \alpha_{para}$ transformations. In addition, a comprehensive evaluation of enthalpy and heat capacity data for Fe-21Cr alloy in the temperature range -273 to 1200 °C (0-1473 K), with explicit incorporation of magnetic contribution has also been made.

4) Sigma phase (σ) was synthesized from its parent alpha (α) phase of $Fe_{54}Cr_{46}$ alloy by annealing at 700 °C (973K) for 360 h in vacuum. A comparative thermal study of sigma (σ) and alpha phase alloy in the temperature range of 100 – 1400 °C (373 to 1673 K) by Differential Scanning Calorimeter (DSC) Showed a single inflection of ferro to para magnetic transition (T_C) at 558 °C (831 K) for alpha phase.

5) The measured sigma (σ) to alpha (α) decomposition temperature under pseudo equilibrium condition as 849 °C (1122 K) is ~ 30 °C higher than the reported upper limit of 820 °C (1093 K) in Fe Cr phase diagram.

6) Kinetics of sigma (σ) to alpha (α) phase transformation has been studied using heating rates from 1 to 50 K min^{-1} in DSC. Activation energy for the transformation was estimated as 369 kJ $mole^{-1}$ employing Kissinger model. The fraction transformed has been modelled using non isothermal KJMA model and the order and kinetic parameters have been determined.

7) The effect of sigma (σ) phase on thermo-physical and heat transport properties of parent alpha (α) phase has been established. While alpha (α) phase undergoes no structural phase transformation, sigma (σ) undergoes a transformation to alpha (α)

phase at 847 ^{o}C (1120 K). . The enthalpy of transformation was measured as 2.6 kJ mole^{-1}.

8) The measured room temperature thermal expansion coefficient for alpha (α) and sigma (σ) phase is 7.39 x 10^{-6} K^{-1} and 1.5 x 10^{-5} K^{-1} respectively. The room temperature thermal diffusivity of alpha (α) and sigma (σ) phases were measured as 0.0484 cm^2 s^{-1} and 0.011 cm^2 s^{-1} respectively by Laser Flash Thermal Diffusivity Analyzer. It is evident that formation of sigma (σ) phase has adverse effects on heat transport properties of alpha (α) phase. The measured room temperature thermal conductivity of alpha phase is 16.9 $Wm^{-1}K^{-1}$ while that of sigma (σ) phase is 3.9 $Wm^{-1}K^{-1}$. Further, a comprehensive analytical modeling of experimental thermodynamic parameters has been carried out which shows a good agreement.
9) The α ↔ γ transformation characteristics of Fe- (1-13 wt.%) Cr binary and Fe-9Cr-W ternary alloys were studied. This work showed that beyond 12 wt% Cr, α ↔ γ transformation is suppressed in Fe-Cr binary alloys, which is lower than the reported value of 14 wt% Cr. W addition beyond 1.5 wt% also suppressed the transformation in Fe-9Cr alloy.
10) A magnetic transition preceding the martensitic transformation during cooling from the high temperature austenite phase field in Fe-9Cr-2W-0.1C (P92 ferritic-martensitic steel) provides evidence for the co-existence of ferrite and martensite at room temperature. The high cooling rates precluded the formation of diffusional ferrite. Complete martensite formation was not achieved in P92 steel for all cooling rates (1 - 90 K min^{-1} in DSC and water quenching) during cooling from austenitisation temperatures in the range of 1223-1423 K (950 – 1150 °C). Thermo-Calc simulation established that P91 steel is in a single phase γ domain during austenitisation, while

the γ phase field shrinks with addition of W and P92 remains in the three phase domain of $\alpha + \gamma$ + MX region which explains for the two phase microstructure.

8.2. Further avenues of research

This thesis presented a comprehensive understanding on the thermodynamic and kinetic properties of Fe-Cr systems. Nevertheless, there are several areas which require further investigations, a few of which are listed below.

1) Effect of alloying additions on kinetics of sigma formation by thermal analysis and correlation with microstructures including the effect of different volume fractions of sigma phase on the elastic properties of alpha phase
2) Effect of sigma phase on the corrosion properties of alpha phase
3) An in-depth structure analysis of sigma phase by high resolution microscopy,
4) Synthesis and characterisation of sigma phase stabilized ferritic steel by mechanical alloying route.
5) First principle calculation of heat transport properties for alpha and sigma phase,

Reference

1. R. Klueh, K. Ehrlich, F. Abe, *J. Nucl. Mater.,* 191 (1992) 116
2. S. Zinkle, N. Ghoniem, *J. Nucl. Mater.,* 417 (2011) 2
3. T. Fujita, *ISJT Int.,* 32 (1992) 175
4. H. Bhadeshia, A. Strang, D. Gooch, *Int. Mater. Rev.,* 43 (1998) 45
5. R. Klueh, D. Harries, *ASTM Int.,* 3 (2001) 1
6. R. Klueh, A. Nelson, *J. Nucl. Mater.,* 371 (2007) 37
7. K. Lo, C. Shek, J.Lai, *Mater. Sci. Engg.,* R 65 (2009) 39
8. J K Sahu, U Krupp, R N Ghosh, H J Christ, *Mater. Sci. Engg., A* 508 (2009) 1
9. S. Saroja, A. Dasgupta, R. Divakar, S. Raju, E. Mohandas, M. Vijayalakshmi, K. Rao, B. Raj, *J. Nucl. Mater.,* 409 (2011) 131
10. U. Klotz, C. Solenthaler, P. Uggowitzer, *Mater. Sci. Eng. A,* 476 (2008) 186
11. W. Jones, C. Hills, D. Polonis, *Metall. Mater. Trans. A,* 22 (1991) 1049
12. Y. Wei, W. Wei, S. Yin, Y. Ke, *Front Mater Sci.,* 7 (2011) 1
13. M. Yoshizawa, M. Igarashi, K. Moriguchi, A. Iseda, H. Armaki, K. Maruyama, *Mater. Sci. Eng. A,* 510-511 (2009) 162
14. S. Jin, L. Guo, Z. Yang, D. Fu, C. Liu, R. Tang, F. Liu, Y. Qiao, *Mater. Charac.,* 62 (2011) 136
15. Y. Shen, H. Liu, Z. Shang, Z. Xu, *J. Nucl. Mater.,* 465 (2015) 373
16. P. Ennis, A. Zielinska-Lipiec, O. Wachter A. Czyrska-Filemonowicz, *Acta Mater.,* 45 (1997) 4901
17. P. Ennis, A. Zielinska-Lipiec, A. Czyrska-Filemonowicz, *Mater. Sci. Tech.,* 16 (2000) 1226
18. V. Knezevic, J. Balun, G. Sauthoff, G. Inden, A. Schneider, *Mater. Sci. Eng. A.,* 477 (2008) 334

19. C. Hsieh, W. Wu, *ISRN Metall.,* 2012 (2012) 732471

20. H. Sieurin, R. Sandstom, *Mater. Sci. Engg.,* A 444 (2007) 271

21 S. Dubiel, J. Cieslak, *Crit. Rev. Solid State Mater. Sci.,* 36 (2011) 191

22. S. Breener, M. Miller, W. Soffa, *Scrip. Metall.,* 16 (1982) 831

23. R. Viswanathan and W. Bakker, *J. Mater. Engg. & Perform.,* 10 (2001) 81

24. W. Gordon and A. van Bennekom, *Mater. Sci. & Tech.,* 12 (1996) 126

25. W. Dench, *Trans. Faraday Soc*., 59(1963)1279

26 G. Belton, R. Fruehan, *Trans. Metall. Soc., AIME*, 1 (1970) 781

27. I. Pavars, B. Baum, P. Geld, *High Temp*., 8 (1970) 67

28. G. Kirchner, T. Nishizawa, B. Uhrenius*, Metall. Trans., A* 4 (1973) 167

29. E. Mazandarany, R. Phelke, *Metall. Trans., A* 4(1973) 2067

30. J. Chipman, *Metall Trans., A* 5 (1974) 521

31. L. Kaufman, *Metall. Trans.,A* 5 (1974) 1688

32. M. Rao, W. Tiller, *Mater. Sci. Eng., 14 (*1974) 47

33. A. Normanton, R. Moore, B. Argent*, Metal Sci.,* 10 (1976) 207

34. D. Downie, J. Martin, *J. Chem. Thermodyn*., 16 (1984) 743

35. Y.Chuang, J. Lin, Y. Chang, *Calphad,* 11 (1987) 57

36. J. Andersson and B. Sundman, *Calphad,* 11 (1987) 83

37. A. Zaitsev, M. Zemchenko, B. Mogutnov, *Russ. J. Phys. Chem.,* 64 (1990) 634

38. B. Lee, *Calphad,* 17 (1993) 251

39. G. Bonny, D. Terentyev, L. Malerba*, J. Phase Equilb.,* 31 (2010) 439

40. W. Xiong , P. Hedstrom , M. Selleby , J. Odqvist , M. Thuvander and Q. Chen, *Calphad,* 35 (2011) 355

41. H. Kuwano, *Trans. Japan Inst. Met*., 26 (1985) 473

42. M. K. Miller, *J. Phys. Colloq.,* 50 (1989) 247

43. M. K. Miller, J. M. Hyde, M. G. Hetherington, A. Cerezo, G. D. W. Smith, C. M. Elliott, *Acta Metall. Mater.*, 43 (1995) 3385

44. R.O. Williams, H.W. Paxton, *J. Iron Steel Inst.,* 185 (1957) 358

45. G. Pomey, P. Bastien, *Revue de Metallurgie,* 53(1956) 147

46. Y. I. Ustinovshikov, B. E. Pushkarev, *Mat. Sci. Eng. A*, 241(1998)159

47. Yu. I. Ustinovshikov, B. E. Pushkarev, *J. Alloys Compd*., 389(2005) 95

48. S. M. Dubiel, G. Inden, *Z. Meallkd.,* 78(1987) 544

49. G. R. Speich, A. J. Schwoeble, W. C. Leslie, *Metall. Trans*., 3(1972) 2031

50. K. Abiko, Y. Kato, *Phys. Stat. Solidi.* 167 (1998) 449

51. A. Hishinuma, S. Takaki, K. Abiko, *Phys. Stat. Solidi*, 189 (2002) 69

52. K. Schroder, *Phys. Rev*., 125 (1962) 1209

53. S. S. Shiniozaki, A. Arrot, *Phys. Rev.,* 152 (1966) 611

54. A.T. Aldred, *Phys. Rev. B,* 14 (1976) 219

55. A.T. Aldred, B.D. Rainford, J.S. Kouvel, T.J. Hicks, *Phys. Rev. B,* 14 (1976) 228

56. B. Fultz, L. Anthony, J. L. Robertson, R. M. Nicklow, S. Spooner, M. Mostoller, *Phys. Rev. B*, 52 (1995) 3280

57. M. S. Lucas, M. Kresch, R. Stevens, B. Fultz, *Phys. Rev. B,* 77(2008) 84303

58. J. Cieslak, M. Reissner, W. Steiner, S. M. Dubiel, *Phys. Stat. Solidi, (a)* 205(2008) 1794

59. S. M. Dubiel, J. Cieslak, B. F. O. Costa, *J. Phys.: Condens. Matter,* 22 (2010) 055402

60. M. Hennion, *J. Phys. F: Met. Phys*., 13(1983) 2351

61. P. Olsson, I. A. Abrikosov, L. Vitos, J. Wallenius*, J. Nucl. Mater*., 321(2003)84

62. J. Wallenius, P. Olsson, C. Lagerstedt, N. Sandberg, R. Chakarova, V. Pontikis, *Phys. Rev. B,* 69(2004) 094103

63. A. Caro, D. A. Crowson, M. Caro, *Phys. Rev. Lett*., 95(2005) 075702

64. J. H. Shim, B. J. Lee, B. D. Wirth, *J. Nucl. Mater.,* 351 (2006) 56

65. P. Olsson, A. Abrikosov, J. Wallenius, *Phys. Rev. B,* 73 (2006) 104416

66. T. Klaver, R. Drautz, M. Finnis, *Phys. Rev. B*, 74 (2006) 094435

67. A. A. Mirzoev, M. M. Yalalov, D. A. Mirzaev, *Phys. Met. Metall.*, 103(2007) 86

68. M. Y. Lavrentiev, R. Drautz, D. N. Manh, T. P. C. Klaver, L. Dudarev, *Phys. Rev. B,* 75 (2007) 014208

69. A. Froideval, R. Iglesias, M. Samaras, S. Schuppler, P. Nagel, D. Grolimund, M. Victoria, W. Hoffelner*, Phys. Rev. Lett.*, 99(2007) 237201

70. D. N. Manh, M. Y. Lavrentiev, S. L. Dudarev, *Comptes. Rendus Physique,* 9(2008) 379

71. P. A. Korzhavyi, A. V. Ruban, J. Odqvist, J. O. Nilsson, B. Johansson, *Phys. Rev. B,* 79(2009) 054202

72. H. Zhang, B. Johansson, L. Vitos, *Phys. Rev. B,* 79 (2009) 224201

73. M. Y. Lavrentiev, D. N. Manh, S. L. Dudarev, *Comp. Mater. Sci.,* 49 (2010) 5199

74. V. I. Razumovskiy, A. V. Ruban and P. A. Korzhavyi, *Phys. Rev. B,* 84 (2011) 024106

75. A. V. Ruban, V. I. Razumovskiy, *Phys. Rev. B,* 86 (2012) 174111

76. M. Y. Lavrentiev , H. Mergia, *J. Phys. Cond. Mat.*, 24 (2012) 326001

77. H. Zhang, G.Wang, M. Punkkinen, S. Hertzman, B. Johansson, L. Vitos, *J. Phys.: Condens.Matter,* 25 (2013) 195501

78. A. Alam, R. K. Chouhan, A. Mookerjee, *Phys. Rev. B,* 83 (2011) 54201

79. D. Terentyev and L. Malerba, *J. Nucl. Mater.*, 329 (2004) 1161

80. G. Bonny, R.C. Pasianot, L. Malerba, A. Caro, P. Olsson, M. Yu. Lavrentiev, *J. Nucl. Mater.,* 385 (2009) 268

81. B. H. Sencer, F. A. Garner, *J. Nucl. Mater.*, 283 (2000) 164

82. T. Okita, N. Sekimura, F.A. Garner, *J. Nucl. Mater.*, 417 (2011) 944

83. J H Shim, H J Lee, B D Wirth, *J. Nucl. Mater.*, 351 (2006) 56

84. M. Cadville, J. Lopez, *Phys. Rep.,* 153 (1987) 331

85. W. Xiong, M. Selleby, Q. Chen, J. Odqvist, Y. Du, *Sol. St. Mater. Sci.*, 35 (2010) 125

86. J. Wallenius, P. Olsson, C. Lagerstedt, N.Sandberg, R. Chakarova, V. Pontikis, *Phys. Rev., B* 69 (2004) 094103

87. P. Korzhavyi, A. Ruban, *Phys. Rev. B,* 77 (2008) 094436

88. P. Villars, J. Daams, *J. Alloys. Compd.,* 197 (1993) 177

89. G. Bonny, D. Terentyev, L. Malerba, *Scr. Mater.*, 59(2008) 1193

90. F. Bergner, A. Ulbricht, C. Heintze, *Scr. Mater.*, 61(2009) 1060

91. G. Bonny, P. Erhart, A. Caro, R.C. Pasianot, L. Malerba, M. Caro, *Model. Simul. Mater. Sci., Eng.*, 17(2009) 025006

92. F. Bley, *Acta Metall. Mater.,* 40(1992) 1505

93. L. Malerba, *SCK-CEN internal report, No.* ER-16 (2006) 1-22.

94. T. Nishizawa, *J. Phase Equilb.*, 16 (1995) 379

95. W. Pepperhoff and M. Acet, *Constitution and Magnetism of Iron and its Alloys*, Springer, Berlin (2007)

96. G. Inden, *Physica, B* 103 (1981) 82

97. M. Hillert, M. Jarl, *Calphad*, 2 (1978) 227

98. K. Tarafder, S. Ghosh, B. Sanyal, O. Eriksson, A. Mookherjee and A. Chakrabarti, *J. Phys. Condens. Matter,* 20 (2008) 44520

99. I.M. Wolff, K. Premachandra, M.B. Cortie, *Mater. Chara.,* 28 (1992) 139

100. L. Niewolak, L. Garcia-Fresnillo, G.H. Meier, W.J. Quadakkers, *J. Alloys Compd.,* 638 (2015) 405

101. M. Vach, T. Kunikova, M. Domankova, P. Sevc, L. Caplovic, P. Gogola, J. Janovec, *Mater. Char.,* 59 (2008) 1792

102. D.N. Wasnik, G.K. Dey, V. Kain, I. Samajdar, *Scripta Mater.*, 49 (2003) 135

103. J.M. Vitek, S.A. David, *Welding J.,* 65 (1986) 106

104. R. Magnabosco, *Mater. Res.,* 12(3) (2009) 321

105 B. Raha, *Mater. Today,* 5 (2018) 7836

106. A.M. Leitner, B. Sepiol, M. Leitner, *Phys. Rev. B*, 82 (2010) 100101

107 J. Cieślak, M. Reissner, S. M. Dubiel, J. Wernisch, W. Steiner, *J. Alloys Compd.*, 460 (2008) 20

108. J. Sopousek and T. Kruml, *Scripta Mater.,* 35(6) (1996) 689

109 A. Blachowski, J. Cieslak, S. M. Dubiel, J. Zukrowski, *J. Alloys Compd.,* 308 (2000) 189

110. A. Blachowski, S.M. Dubiel, J. Zukrowski, *Intermetallics*, 9 (2001) 493

111. M. David, *Scripta Metall.,* 13 (1979) 1195

112. F. Liu, Y.H. Hwang, S.W. Nam, *Mater. Sci. Eng. A,* 483 (2008) 418

113. O. Conejero, M. Palacios, S. Rivera, *Eng. Failure Anal.,* 16 (2009) 699

114 D. Li, Y. Gao, J. Tan, F. Wang, J. Zhang, *Scripta Metall.,* 23 (1989) 1319

115. A. Kington, F. Noble, *Mater. Sci. Eng. A,* 138 (1991) 259

116. A. Babakr, A. Al-Ahmari, K. Jumayiah, F. Habiby, *J. Minerals and Mater. Chara. Eng.* 7 (2008) 127

117. D. Chastell, P. Flewitt, *Mater. Sci. Eng.,* 38 (1979) 153

118. I. Kim, J. Lee, A. Kimura., *J. Nucl. Mater.,* 329-333 (2004) 607

119. J. Brozda, J. Madej, *Eng. Failure Anal.,* 15 (2008) 368

120. E. Chun, K. Saida, *J. Nucl. Mater.,* 505 (2018) 212

121. G. Bergman and D. Shoemaker, *Acta cryst.,* 7 (1954) 857

122. J. Joubert, *Prog. Mater Sci.,* 53 (2008) 528

123. I. Ansara, T. Chart, A. Guillermet, F. Hayes, U. Kattner, D. Pettifor, N. Saunders, K. Zeng, *CHALPHAD: Comput. Coupling Phase Diagrams Thermochem.,* 21 (1997) 171

124. R. Williams, *Trans. Met. Soc. A. I. M. E.,* 212 (1958) 497

125. O. Kubaschewski, T G Chart, *J. Inst. Metals,* 93 (1964-65) 329

126. D. Chandra, L. H. Schwartz, *Metall. Trans.,* 2 (1971) 511

127. T. De Nys, P. M. Gielen, *Metall. Trans.,* 2 (1971) 1423

128. H. Ettwig, W. Perrerhoff, *Arch Eisenhuettenw,* 43 (1972) 271

129 P. Camus, *J. Phys.,* 48 (1987) 6

130 A. Cerezo, J. Hyde, M. Miller, S. Petts, R. Setna, G. Smith, *Phil. Trans. R. Soc. Lond.,* A 341 (1992) 313

131 S. Novy, P. Pereige, C. Pereige, *J. Nucl. Mater.,* 384 (2009) 96

132. A. Cook, F. Jones, *J. Iron Steel Inst.,* 148 (1943) 217

133. E. Baerlecken, H. Fabritius, *Archiv Eisenhuttenw.,* 26 (1955) 679

134. G. Poomy, P. Bastien, *Revue de Metallurgie,* 53 (1956) 147

135. N Yukawa, M. Hida, T. Imura, M. Kawamura, Y. Mizuno, *Metall. Trans.,* 3 (1972) 887

136 O. Kubaschewski, *Springer Verlag,* 32(1982)349

137. I. Backhurst, *J. Iron Steel Inst.,* 189 (1958) 124

138. I. Malinsky and F Claisse, *J. Chem. Thermodyn.,* 5 (1973) 615

139. H. Zeedijk, *Prakt. Metall.,* 527 (1972) 85

140. F. Shortsleeve, M. Nicholson, *Trans. ASM,* 43 (1951) 142

141. G. Sauthoff, W. Speller, *Z. Metallkde.,* 72 (1981) 457

142. F. Waanders, S. Vorster, H. Pollak, *Hyp. Int. (c),* 3 (1998) 277

143. K. Premachandra, M. Cortie, R. Eric, *Mater. Sci. Technol.*, 8 (1992) 437

144. B. Costa, S. Dubiel, *Phys. Stat. Sol. (a),* 139 (1993) 83

145. A. Mikikits-Leitner, B. Sepiol, X. Leitner, J. Cieslak and S. M. Dubiel, *Phys. Rev. B,* 82 (2010) 155503

146. F. Abe, T. Noda, H. Araki, M. Okada, *J. Nucl. Sci. Tech.,* 31(1994) 279

147 S. Raju, B. Jeya Ganesh, A. Rai, R. Mytili, S. Saroja, B. Raj, *J. Nucl. Mater.,* 405 (2010) 59

148 Ravikirana, R. Mytili, S. Raju, S. Saroja, T. Jayakumar, E. Rajendrakumar, *Mater. Char.,* 84 (2013) 196

149. L. Tan, *Semi – annual progress reports, Oak Ridge National Laboratory, DOE /ER*-0313/52 (2012) 1-7

150. Q. Gao, C. Wang, F. Qu, Y. Wang, Z. Qiao, *J. Alloys Comp.,* 610 (2014) 322

151. R. Mythili, Ravikirana, J. Vanaja, K. Laha, S. Saroja, T. Jayakumar, M. D. Mathew, E. Rajendra Kumar, *Procedia Eng.,* 55 (2013) 295

152. Q. Gao, Y. Liu, X. Di, L. Yu, Z. Yan, *J. Mater. Res.,* 27 (2012) 2779

153. Q. Gao, Y. Liu, X. Di, Z. Yan, Z. Dong, *J. Mater Sci.,* 46 (2011) 6910

154. S. Raju, H. Tripathy, A. Rai, R. N. Hajra, S. Saibaba, *J. Nucl. Mater.,* 459 (2015) 150

155. S. Ghosh, *J. Mater. Sci.,* 45 (2010) 1823

156. V. Knezevic, M. Subanovic, O. Hamart, H. Heuser, K. Tak, *Proceedings from seventh international conference,* (2013) 648

157. L Hansen, R. Criddle, *Thermochim. Acta.,* 160 (1990) 173

158. K. Gallagher, *Handbook of Thermal Analysis and Calorimetry*, Elsevier, (1998)

159. Multi HTC-96, *Setaram Installation Guide and Manual* (1997)

160. K. D. Maglic, A. Cezairliyan and V. E. Peletsky (Eds.), *Compendium of Thermophysical Property Measurement Techniques,* vol. 2, Plenum Press, New York, (1992)

161. Y. Takahashi and Y. Kohsaka, *J. Nucl. Mater.,* 130 (1985) 109

162. D. G. Archer, *J. Phys. Chem. Ref. Data*, 22 (1993) 1441.

163. J. D James, J. A Spittle, S. G. R. Brown and R. W. Evans, *Meas. Sci. Technol.*, 12 (2001) 1

164. S. Sarge, E. Gmelin, G. Hohne, H. Cammenga, W. Hemminger,W. Eysel, *Thermochim. Acta*, 247 (1994) 129

165. http://www.setaram.com/SETSYS-Evolution-DTA-DSC.htm

166. R. Sabbah, An Xu-wu, J.S. Chickos, M.L. Planas Leitão, M.V. Roux and L.A. Torres, *Thermochim. Acta,* 331 (1999) 93

167. L. Richardson and E. L. Charsley, *Calibration and Standardisation in DSC*, in *Handbook of Thermal Analysis and Calorimetry. Vol. 1: Principles and Practice*, Elsevier Science (1998)

168. E. Gmelin and S. Sarge, *Pure Appl. Chem.,* 67 (1995) 1789

169. B. Wunderlich, *Thermal Analysis*, San Diego, CA, Academic Press, (1990)

170. M. Brown, *Introduction to Thermal Analysis,* Chapman and Hall, London, (1988).

171. G. Höhne, W. Hemminger, and H. J. Flammersheim, *Differential Scanning Calorimetry: An Introduction for Practitioners*, Berlin, Springer-Verlag, (1996)

172. Setsys Evolution-TMA 16/18, *Installation Guide and Manual* (2010)

173. R. G. Munro, *J. Am. Ceram. Soc.*, 80 (1997) 1919

174. N. Manoj, D. Jain, J. K. Gautam, K. C. Thomas, V. Sudarsan, C. G. S. Pillai, R. K. Vatsa and A. K. Tyagi. *Measurement,* 92 (2016) 318

175. G. Mohapatra, F. Sommer and E. J. Mittemeijer, *Thermochim Acta,* 453 (2007) 31

176. W. J. Parker, R. J. Jenkins, C. P. Butler and G. L. Abbott, *J. Appl. Phys.,* 32 (1961) 1679

177. F. Righini and A. Cezairliyan, *High Temp. High Press.,* 5 (1973) 481

178. S. Min, J. Blumm, and A. Lindemann, *Thermochim. Acta,* 455 (2007) 46

179. W. M. Steen, *Laser Materials Processing*, (3rd edition), Springer, London; (2003) 70

180. R. F. Speyer, *Thermal analysis of Materials*, Marcel Dekker, Inc, New York;(1993) 242

181. R. P. Tye, D. Hume, *J. Therm. Anal. Calorim.*, 131 (2018) 289

182. A. Dinsdale, *Calphad,* 15 (1991) 317-425

183. D. Wallace, *Thermodynamics of Crystals*, Wiley, New York, (1972).

184. O. Anderson, *Equation of State of Solid for Geophysics and Ceramic Science,* Oxford university press, New York, (1995)

185. D. Sanditov, V. Mantanov, M. Darmaev and B. Sanditov, *Tech. Phys.,* 54 (2009) 385-388

186. G. Preston, *Philos. Mag.,* 13 (1932) 419

187. P. Desai, *J. Phys. Chem. Ref. Data,* 15 (1986) 967

188. Q. Chen, B. Sundman, *J. Phase Equilib.,* 22 (2001) 631

189. L. Jithender, N. Gopikrishna, *Ind. J. Phys.,* 87 (2013) 537

190. V. Moruzzi, J. Janak and K. Schwarz, *Phys. Rev., B,* 37 (1988) 790

191. S. Linderoth, P. Larsen, *MRS Proceedings*, 575 (1999) 325

192. H. Kissinger, *J. Res. NBS,* 57 (1956) 217

193. J Augis, J Bennett, *J. Therm. Anal.,* 13 (1978) 283

194. M Matsura, K Suzuki, *J. Mat. Sci.,* 14 (1979) 395

195. R. R. Wellen, E. L. Canedo, *Polymer Testing,* 40 (2014) 33

196. A. N. Kolmogorov, Izv. A N SSSR, *Ser.Matem.,* 3 (1937) 355

197. W. A. Johnson, R. F. Mehl, *Trans AIME,* 135 (1939) 416

198. M. Avrami, *J. Chem. Phys.,* 7 (1939) 1103

199. J. Cieslak, M. Reissner, W. Steiner, S. Dubiel, *J. Mag. Mag. Mater.,* 272 (2004) 534

200. K. Abiko, Y. Kato, *Phys. Status Solidi A*, 167 (1998) 449

201. S.M. Shelton, *Bureau of standards J. of research*, 12 (1934) 447

202. T. Karthikeyan, M. Dash, S. Saroja, M. Vijayalakshmi, *Metall. Mater. Trans. A.,* 44 (2012) 1673

203. B. Hahn, H. V. Gmb, D. Bendic, H. Forschung Gmb, Duisburg., Valloure c, (2015) 2